Studying Ultrafast Vibrational dynamics of Intramolecular Hydrogen Bonds using Broadband Infrared Pump-Probe Spectroscopy.

Madhumitha Balasubramanian

A dissertation

submitted in partial fulfillment of the

requirements for the degree of

Doctor of Philosophy

University of Washington

2018

Reading Committee:

Munira Khalil, Chair

Anne McCoy

Xiaosong Li

Program Authorized to Offer Degree:

Chemistry

University of Washington

ABSTRACT

Studying Ultrafast Vibrational dynamics of Intramolecular Hydrogen Bonds using Broadband Infrared Pump-Probe Spectroscopy.

Madhumitha Balasubramanian

Chair of the Supervisory Committee:
Associate Professor Munira Khalil
Department of Chemistry

The concept of hydrogen bonding has been intimately involved in the bonding and arrangement pattern of various molecular assemblies including complex protein structure. There are also indications that hydrogen bonds play an important role also in biological electron transfer across long distances. The vibrational dynamics of intramolecular hydrogen bonds pose experimental and theoretical challenges due to anharmonic couplings between the high frequency hydrogen bond stretching (ν_{OH}) mode and low frequency skeletal motions. This dissertation presents work done by using ultrafast Infrared pump-probe spectroscopy to study the vibrational dynamics of two intramolecular hydrogen bonded complexes, 10-Hydroxybenzo[h]quinolone (HBQ) and 2-(2′-Hydroxyphenyl)benzothiazole (HBT) dissolved in carbon tetrachloride. One of the biggest difficulty in studying the νOH stretching vibration is that they have complex and broad lineshapes in the infrared region (IR) that are difficult to decipher.

To overcome this difficulty, we have developed a tunable broadband mid-infrared (BBIR) source with the spectral range of 2-8 microns. The broadband pulse enables us to perform novel experiments in multiple domains (both in infrared and electronic) to understand energy transfer dynamics and vibrational couplings of very broad peaks. The tunable BBIR source is generated by a filamentation process of 800nm and 400nm pulses in a gas cell. To generate compressed pulses for the experiment, correction of higher order dispersion effects is necessary. Hence a compressor was built with a deformable mirror for the manipulation of spectral phase to make transform limited pulse. An iterative genetic algorithm was written with a simple single valued feedback for the optimal mirror compression. Nearly transform limited pulses were measured with the following characterization techniques to extract electric field: cross correlation Frequency Resolved Optical Gating (XFROG) and Spectral Phase Interferometry for Direct Electric-field Reconstruction (SPIDER).

The compressed broadband IR (BBIR) source, when used as part of a third order nonlinear infrared pump-probe spectroscopy, was able to give us information into the electronic ground state potential energy surface of the two model systems. .We pump the ν_{OH} and probe across 1800 cm^{-1} to 3300 cm^{-1} using the broadband IR pulse. The average lifetime of the OH mode for the HBQ and HBT systems was calculated to be 1.65 ps and 1.30 ps respectively. Both systems exhibit large anharmonicities (> 500 cm-1), which are characteristic of strongly hydrogen bonded systems. Additionally, we observe the coherent beating of low-frequency modes of 248 cm^{-1} and 118 cm^{-1} across the ν_{OH} stretch of HBQ and HBT, respectively. Anharmonic frequency calculations at the DFT level identify these low-frequency structural modes as in-plane bending modes which modulate the intramolecular hydrogen bonding

distance. These findings prove that the anharmonic nature of the fundamental ν_{OH} stretch is primarily dictated by the coupling to low frequency structural modes and these motions play an important role in the hydrogen bonding dynamics.

Table of Contents

LIST OF FIGURES

LIST OF TABLES

GLOSSARY

1D: 1-dimensional

2D: 2-dimensional

AOPDF: Acousto-optic programmable dispersive filter

AR: Anti-reflection

BBIR: Broadband infrared

BBO: β-Barium borate

BS: Beam splitter

CM: Curved mirror

DBQ: 10-deuteroxybenzo[h]quinoline

DFG: Difference frequency generation

DM: Deformable mirror

DFG: Difference frequency generation

ESA: Excited state absorption

ESIPT: Excited-state intramolecular proton transfer

ET: Electron Transfer

FFT: Fast Fourier-Transform

FO: Focusing optic

fs: femtosecond

FT: Fourier-Transform

FTIR: Fourier-Transform Infrared

FWM: Four wave mixing

FWHM: full-width half-maximum

GVD: Group velocity dispersion

GDD: Group delay dispersion

GC: Gas cell

GS: Ground state

GSB: Ground state bleach

GVM: Group velocity mismatch

HCF: Hollow core fiber

HAT: Hydrogen atom transfer

HBQ: 10-hydroxybenzo[h]quinoline

HgCdTe: Mercury cadmium telluride

HWP: Half-waveplate

I: Intensity; Absolute Square of the electric field

Iso: Isotropic

IR: Infrared

MCT: Mercury cadmium telluride detector

MIR: mid-infrared

Mono: Monochromator

ν_{OD}: Deuteroxyl vibrational stretching mode

ν_{OH}: Hydroxyl vibrational stretching mode

OEC: Oxygen evolving complex

OPA: Optical parametric amplification

OPCPA: Optical parametric chirped pulse amplification

P: Polarization optic

PES: Potential energy surface

PCET: Proton-coupled electron transfer

PM: Off-axis parabolic mirror

PP: Pump-probe

ps: picosecond

PS II: Photosystem II

PT: Proton transfer

SH: Second harmonic

S: Sample

Si: Silicon

Sig: Signal

SPIDER: Spectral phase interferometry for direct-electric field reconstruction

SNP: Sodium nitroprusside

TL: Transform Limit

TP: Calcite crystal

W: Watt

XFROG: Cross-correlation frequency-resolved optical gating

ZZZZ: All fields of electric field are parallel to one another

DEDICATION

This dissertation is dedicated with love and affection
to my Mother and Father

ACKNOWLEDGEMENTS

This work is based on research conducted at University of Washington, Seattle in the Khalil laser lab between 2013 and present. I am thankful for my friends and colleagues in encouraging me and persuading me throughout my research experience. I would like to start by thanking Professor Munira Khalil for academic support and for showing confidence in my work. When I entered the group my knowledge in IR spectroscopy was minimal and thanks to her I have developed knowledge and understanding in principles of vibrational spectroscopy. She has consistently been challenging me and helping me develop my ideas. Without her guidance, patience and persistent help this dissertation would not be possible.

Senior students Anthony Reynolds, Jennifer Brooks and Karla Slenkamp were instrumental in my early years as a graduate student and helped me learn on the laser table. Trevor Courtney, a Postdoctoral fellow who entered the Khalil group not long after me was a fantastic source of information in both fundamentals of spectroscopy and technical knowledge. I thank him for the extraordinary help he provided to help build the deformable mirror compressor. Zachary Fox started with me as a member of Khalil group and we always had a great working relationship as fellow graduate students. We learnt our way together in the laser lab and have always consulted each other about the problem we faced. He has always been a solid friend with whom I was able to celebrate the success of the grated school career as well as lament about some of the losses in the research. James Gaynor, an old soul, has been a part of the Khalil group two years after me. We shared our interests not only in Chemistry but also our taste in IPA. We have shared the same laser lab and worked closely for the pulse shaper and development of 2DEV spectroscopy. He has been a sounding board always ready to talk about science and has been a source of motivation. Undergraduate Cindy Tseng has been very helpful

in sample preparations and deuteration work. Our newly joined graduate students, Jason Sandwisch, William Miller and Robert Weakly have filled our group and reminded me of my years as a young graduate student. Our new postdoctoral fellow Joel Leger has helped me in my last leg of graduate student and has regaled me with stories that have made this journey fun. I would like to thank all Khalil group members I have worked with present and past for intellectually stimulating conversations over these past years as well as support.

I am indebted my family for helping me in academic career. My mother and father have always supported me in my interest in chemistry and my graduate school career was not any different. Without their support and guidance this work would not have been possible. Throughout the years, they gladly showered a lot of love and affection for their youngest daughter. They have helped me outside of graduate school by taking me to travel to various countries as a distraction from science. Their regular phone calls and care packages despite the long distance from their destination of Thailand has helped me make Seattle feel like home. Special thanks to my sister and her new family for lifelong support and strength that has helped me finish my graduate school successfully.

My graduate school career would be empty if I did not thank my friends from my graduate and undergraduate time. They have comforted me and allowed me to enjoy new experiences with them. My trying moments at graduate school have been reduced to mere inconveniences thanks to their undying support and encouragement.

Chapter 1: Introduction

1.1The Name's Bond, Hydrogen bond:

Hydrogen bonds play critical roles in various biological, material and photosynthetic molecular systems. These important interactions between molecules influence molecular structures over time in solvent, gas-phase or solid state environment. In the condensed phase, the dynamics of hydrogen bonds is closely associated with the mechanism of chemical and biological reactions [1, 2]. Intramolecular hydrogen bonding is a site-specific interaction between donor and acceptor groups within a molecule and the mechanism of such interactions play a remarkable role in photophysics and photochemistry processes[3]. Understanding the microscopic interactions governing the vibrational dynamics of intramolecular hydrogen bonds is important for elucidating the structure-function relationships of molecular complexes in biology, chemistry and material science[4]. In biology, examples include proteins and enzymes that rely on intramolecular and intramolecular hydrogen bonding to stabilize into secondary and tertiary structures that play a crucial role in the functionality of the molecule. The concerted formation and breakage of these hydrogen bonds between solvent and protein or between an amino acid and the protein backbone modulates the flexibility of the protein and controls its specific function [5, 6].

In photophysics intramolecular hydrogen bonding helps in the planarization of the π conjugated systems and is closely involved with excited state intramolecular proton transfer processes [7] . Hence these interactions are routinely associated with photochromic, thermochromics and sensing applications [8]. Of particular interest is learning how the transfer of the proton from a donor to an acceptor is modulated by the motions of the molecule and the

surrounding solvent. Intramolecular proton transfer in the excited state has practical applications for developing dye molecules and molecular switches. Our ability to make better dye molecules hinges on understanding the role of vibrational dynamics in intramolecular hydrogen-bonded complexes in the ground and electronic excited states. These include luminescence sensors which allow the excited state proton transfer with the addition of analytes. They can be used as molecular fluorescent probes as a way to label and study DNA-protein interaction [9, 10]. The dynamics of hydrogen bonds in solution is associated with crucial processes that dictate many different chemical and biological reactions. This process are not well understood because the nature of hydrogen-bond dynamics such as hydrogen/proton transfer reactions, breaking and reformation of hydrogen bonds as well as local interactions in the microscopic levels, all of which involve vibrational motions are extremely difficult to probe [11]. Intramolecular hydrogen bonding plays a special role in important intramolecular interactions and a critical element in selected molecular arrangements. The formation of intramolecular hydrogen bonds has a very pronounced effect on molecular structure and properties.

Due to the ubiquitous nature and the tremendous importance of the intramolecular hydrogen bonding, significant advances have been made over recent years to define the energy and spectroscopic landscape of these interactions. Research studies dealing with all facets of intramolecular hydrogen bonding, ranging from theory to experiment, from spectroscopic characterization to synthetic applications involving structural and functional aspects have been published [12-19]. In spite of numerous studies, the process remains poorly understood at the microscopic level because hydrogen-bond dynamics, such as bond rearrangements and hydrogen/proton transfer reactions, are extremely difficult to probe [20-25].

1.2 Understanding the vibrational landscape of the hydrogen bond:

The ν_{OH} stretch in the hydrogen bonded system results in drastically different vibrational spectra to the free ν_{OH} stretch. Strongly hydrogen bonded systems exhibit very broad OH stretches which are highly structured as well as having a spectral red shift compared to their free ν_{OH} counterpart as seen in Figure 1.1. The red shift is caused by the lengthened and weakened covalent OH bond due to the attraction of the hydrogen bond. Greater hydrogen bond strengths typically shift the ν_{OH} vibration to lower frequencies with greatly increased intensity in the infrared regime due to increased dipoles[26]. These differences in the width of vibrational spectra have been attributed to Fermi resonances with overtones and combination bands. Fermi resonances arises from the mixing of vibrational states (fundamental, overtone and combination bands) leading to linear combination of states with altered frequencies. These features are dependent on coupling strength and the energy gap of the mixing states. In hydrogen bonding systems, the energy gap of the mixing states can be altered by the hydrogen bonding dynamics [27-29].

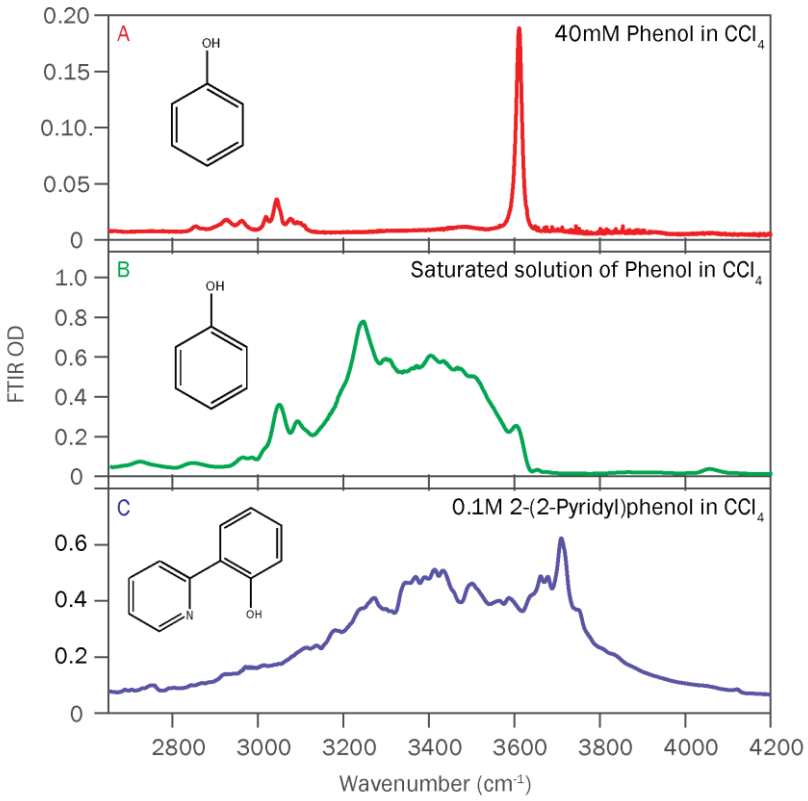

Figure 1.1: Infrared absorption spectra showing ν_{OH} stretching absorption bands of (A) the free ν_{OH} group of dilute solution of phenol in CCl_4, (B) intermolecular hydrogen bonding O-H system in a saturated solution of phenol in CCl_4, (C) intramolecular hydrogen bonding O-H system in 2-(2-Pyridyl)phenol in CCl_4.

Another phenomena attributed to the broadened hydrogen bond vibrational spectra is anharmonic coupling to low frequency hydrogen bond modes. Mechanical anharmonicity is described as the difference between the spectral positions of the overtone and the fundamental stretching band [30]. Hydrogen bonding systems typically have anharmonicities ranging several hundreds of cm^{-1} compared to lower anharmonicities for free O-H systems and this is directly related to Frank-Condon like progressions caused by coupling to low frequency structural modes [11, 31, 32]. Vibrational studies have shown that the potential of the OH stretch is modulated by low frequency modes which gate the donor-acceptor distance. These modes affect the distance as well as orientation of the donor and acceptor groups in the system and are directly involved in

the formation and breaking of the hydrogen bonds [11]. The anharmonic coupling between the high frequency OH stretch and the low frequency structural modes has been used to understand not only the very broad and highly structured OH stretching band but also Excited State Intramolecular Proton Transfer (ESIPT) processes associated with it. Previous work on strongly hydrogen-bonding systems such as acetic acid dimers and benzoic acid dimers have set a precedent on crucial information that can be retrieved for similar model systems. They have shown vibrational lifetimes of the ν_{OH} are relatively fast 150-250 fs and are quite often correlated with low frequency structural modes generally around 50-150 cm^{-1} [33, 34]. Thus, the OH stretching vibration (ν_{OH}) is an excellent and direct reporter of the hydrogen bonding dynamics.

Vibrational transitions of molecules can provide a window into the molecular properties and structure. While linear spectroscopy such as Fourier Transform Infrared Spectroscopy (FTIR) can be used to characterize molecular structures and dynamics, the peculiar spectral structure of the hydrogen bonded ν_{OH} stretch, which pose a challenging problem with line shapes, warrants ultrafast third order experiments [31, 35]. The complexity of the line shapes arises from the different microscopic interactions which can give rise to a coupling of different modes [36]. An example of ultrafast vibrational spectroscopy, pump-probe technique, has been widely applied to study ultrafast vibrational dynamics. However, it has been relatively hard to use ultrafast infrared pulses to pump and probe the ν_{OH} stretch. One of the main deterrents for this is the bandwidth required to cover the fundamental and overtone of the OH stretching band of these strong hydrogen bonding systems that can span several hundred cm^{-1}. Another difficulty in dealing with these systems, is that the lifetimes of the ν_{OH} stretch are very short (<1 ps). Hence progress in the development of ultrasfast mid-IR pulses has been closely associated with advancements in ultrafast vibrational studies on the ν_{OH} stretch in strongly intramolecular

hydrogen bonded systems. To overcome these technical difficulties, we have developed a broadband IR source as well as shortened the pulses to be used in time resolved spectroscopy.

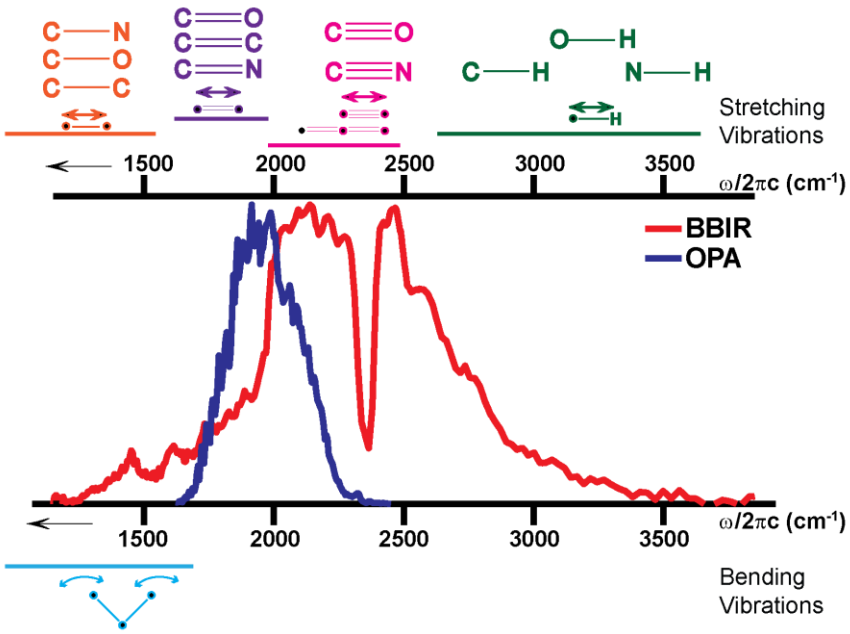

Figure 1.2: Frequency ranges of various stretching and bending vibrations of Interest compared with bandwidth of conventional mid-IR sources and the novel broadband source

1.3 Broadband Mid –IR pulses:

In recent years, light sources with very short pulses have become an indispensable tool for spectroscopies spanning X-ray to terahertz wavelengths. However, coherent pulses in the mid-IR region used in time-resolved spectroscopies have been limited by a relatively narrow bandwidth, residual dispersion, or both. Traditional mid-IR sources with microjoule pulse energies include the difference-frequency generation (DFG) between the near-IR signal and idler outputs of an optical parametric amplifier (OPA) to generate tunable mid-IR pulses with 250–400 cm^{-1} full width at half maximum spectral bandwidth ($\Delta\omega_{FWHM}$) and sub-70 fs [37] down to 45 fs [38] time duration. An alternative mid-IR source is based on optical parametric chirped pulse amplification (OPCPA), which has been shown to

produce high intensity mid-IR pulses [39, 40]. A very recent study generated mid-IR supercontinuum laser pulses by focusing 70 fs, 30 μJ mid-IR pulses in commercially available bulk chalcogenide glasses [41]. Even though these conventional sources can cover a wide spectral range by continuously tuning the wavelength, they cannot cover the entire range simultaneously to cover large range of frequencies needed for hydrogen bonded systems as seen in Figure 1.2. The ability to probe various different vibrational modes in one laser shot have made the need for broadband pulses in the mid IR region at the forefront of technical developemnent.

Fuji et al. (2006) introduced an elegant approach to generating a few-cycle mid-IR pulse using a four wave mixing process generated inside a filament in air. The novel method, similar to the work in the Khalil group, allows the generation of mid-IR and far-IR pulses with broad spectral bandwidths by focusing intense pulses of 800 nm light and its harmonics into gaseous media, creating filamentation [42-52]. In the mid-IR region, the resulting continua can have $\Delta\omega_{FWHM}$ in excess of 1000 cm^{-1} (<15 fs transform limit) with nanojoule pulse energies, which makes these broadband mid-IR (BBIR) pulses suitable for spectroscopies of molecules with multiple and potentially broad vibrational transitions across the mid-IR spectrum.

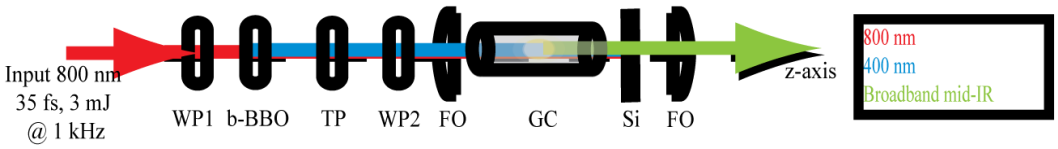

Figure 1.3: BBIR generation using 800 nm/400 nm light fields in a pressure-controlled gas cell. WP1: Half-wave plate [λ/2 @ 800nm]; b-BBO: 0.1mm Type I barium borate crystal; TP: birefringent calcite crystal timing plate; WP2: dual wavelength half-wave plate [λ/2 @ 800nm and λ @ 400nm]; FO: focusing optic, 1m focal length silver-coated concave mirror; GC: Home-built 1.2m stainless steel gas cell capped with 1mm thick UVFS (entrance) and 2mm BaF_2 window(exit); Si: 0.5mm thick silicon wafer placed at Brewster's angle.

The generation of broadband and tunable mid-IR pulses is based on a two-color filamentation process in air. The BBIR pulses, spanning the spectral region between 2.5 and 8 μm (Fig. 1), result from a third-order nonlinear interaction between two short pulses, one centered at 800 nm and the other at 400 nm in various gas media under different pressures. The generation of the broadband pulse during the filamentation is attributed to the four wave mixing (FWM) process from a third order nonlinear intensity response ($\chi^{(3)}$) of the propagation medium, here the gas media. The FWM process for the current set up is given below:

$$\omega_{BBIR} = \omega_{800} + \omega_{800} - \omega_{400} \qquad (1)$$

The various frequencies (ω_n)'s correspond to the angular frequencies of the different photons involved in the process. In this scheme, two photons of the strong pump pulse (~800nm) interact with one photon of the weaker second harmonic (SH) pulse (~400nm) to produce a photon of mid IR. While the carrier frequencies of three input fields add to zero, the response is derived as a result of the broad carrier envelopes of the input pulse. The 400 nm pulse is generated by doubling 800 nm pulses in a Barium borate (BBO) crystal. The second harmonic and the fundamental pulses are spatially and temporally overlapped and focused into air by a concave mirror (r = −1 m), generating a bright filament. A calcite delay plate is used in the collinear geometry to compensate for the temporal walk off between the fundamental and SH. The filamentation and FWM occur in an enclosed gas cell where the gas media and pressure conditions can be changed for tunability. The resulting beam is filtered for the BBIR pulse by two pieces of silicon (0.25mm each) and resized using a reflecting telescope [45].

The generation of the BBIR is subject to the balance of multiple processes that occur as powerful ultrashort beams focus into a gas medium. Self-focusing is the process in which the

index of refraction of material is modified by the intense laser beam in such a manner that leads to a focusing of the beam within material. As the beam radius further decreases closer to the self-focusing point, the beam may collapse on itself destroying the optical medium. However, in nonlinear media such as air and other gases, the collapse is negated due to the ionization of air creating plasma which in turn defocuses the beam [53, 54]. A filament occurs when a balance between self-focusing, plasma defocusing and diffraction is met and can travel over many Rayleigh lengths. This results in an enhancement of nonlinear processes occurring in the filamentation area and helps with the pulse compression [55-57]. The self-phase modulation of the 800 nm and the cross phase modulation of the 800 nm onto the 400 nm result in the broadening of the pulses by the FWM equation (Eq.1) [58, 59]. These third order processes are modified under different pressures of the gas cell to generate different BBIR spectrum. All these phenomena have a profound effect on the electric field of the resulting BBIR pulse giving it a very complicated structure and shape [54, 60].

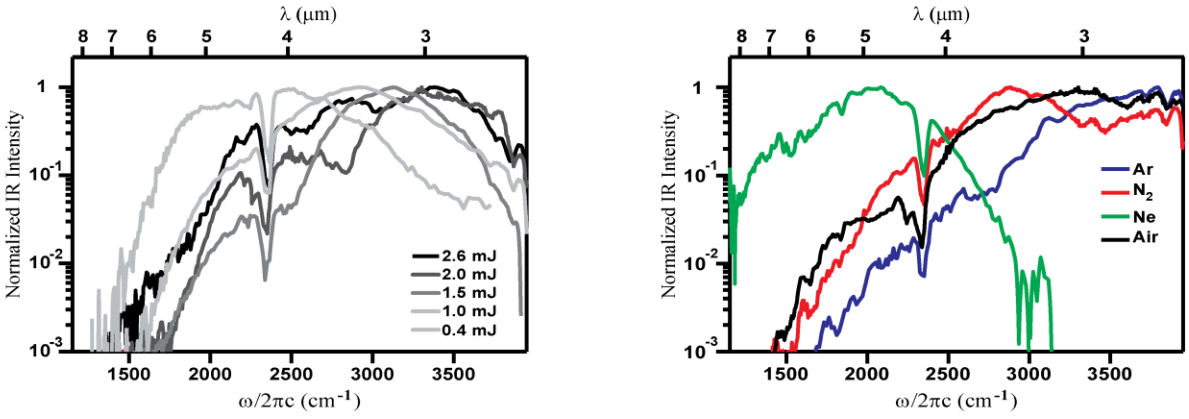

Figure 1.4: Analysis of the tunability of BBIR pulses with respect under various conditions. A) Spectral shift of the BBIR pulse as a function of 800nm Input energy (in air at 1000 Torr) B) Spectra of BBIR pulses generated in different gas media at fixed pressure of gas cell (760 torr).

The compression of mid IR pulses has traditionally relied on using materials which impart different higher order dispersion are used. However, these methods of second-order dispersion material compensation [61] are not sufficient for BBIR compression, as the group velocity dispersion (GVD) of each commonly used material is strongly dependent on frequency over the much larger BBIR bandwidth as seen in Figure . This poses a challenge for passive compensation of dispersion both intrinsic to the generated BBIR and from additional optics such as beam splitters and sample windows practical to spectroscopy experiments. In spectroscopies utilizing OPA-based IR pump and BBIR probe pulses, the reported BBIR durations or experimental time resolutions indicate BBIR pulses of ~70 fs, i.e., longer than the pump pulses [62-64]. Chapter 2 of this thesis will detail the construction and use of such an adaptive optics pulse shaper to compress the broadband pulses to Fourier limits.

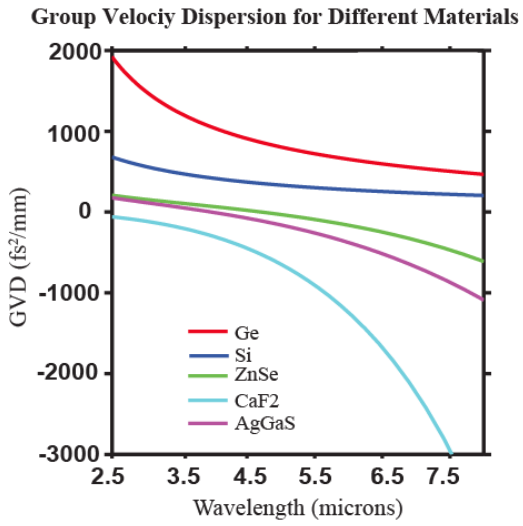

Figure 1.5: Second order dispersion of common materials used in ultrafast spectroscopy

1.4 Compression of the broad band pulse:

A modulated pulse like the BBIR is not monochromatic. Different frequency components travel through the medium with generally different phase velocities, and therefore, accumulate different

phase shifts which give origin to phase distortion. The Taylor expansion of the wave vector, *k* as a function of the angular frequency ω around some center frequency, ω_0, is given by:

$$k(\omega) = k_0 + \frac{\partial k}{\partial \omega}(\omega - \omega_0) + \frac{1}{2}\frac{\partial^2 k}{\partial \omega^2}(\omega - \omega_0)^2 + \frac{1}{6}\frac{\partial^3 k}{\partial \omega^3}(\omega - \omega_0)^3 + \ldots \quad (2)$$

The zeroth term is a common phase shift term and the first term describes the overall time delay of the pulse. The third term contains the group delay dispersion (GDD) and commonly referred to as linear chirp. Dispersion of third orders and beyond is grouped as higher order effects. Since a pulse always has a finite spectral width, dispersion can cause its frequency components to propagate with different velocities and has an effect on pulse duration. In this case, the BBIR pulse acquires chirp during propagation in the medium due to the effects of chromatic dispersion and nonlinearities (self-phase modulation and cross phase modulation). The pulse has been modified post generation to correct for the various aberrations like GDD as well as higher order effects seen in Equation 2 [65].

The smallest possible pulse duration (Fourier transform limit) is set by the spectral width of the pulses which is not modified by dispersive effects. This limit is derived from uncertainty principle, $\Delta\omega \times \Delta t = \frac{1}{4\pi}$ where Δω is the frequency spread and Δt is the pulse duration. For a Gaussian pulse the lower limit for the pulse duration for a given spectral width can be set by set by the time bandwidth product of approximately 0.44. Bandwidth limited pulses have the minimum possible time bandwidth product whereas chirped pulses have larger values. The linear chirp of a pulse can be reversed by propagating it through optical components with suitable dispersive properties. For example if the group velocity of a pulse increases with decreasing optical frequency, material with the opposite dispersive property can be added to bring all the

frequency components together. The dispersion of various orders for a medium can be calculated from the refractive index and Sellmeier formula. Figure 1.5 shows the second order dispersion (linear chirp) for some common materials used in ultrafast experiments [66]. It can be seen from the curvature of GDD traces in Fig. 1.5 that compression of BBIR pulses is not feasible over the entire bandwidth with material compensation alone as these materials cannot provide a constant GDD correction across the BBIR bandwidth without introducing additional dispersion.

Several research groups have demonstrated the manipulation of higher-order dispersion in the spectral phase of mid-IR pulses, first through indirect (near-IR) [67, 68] and then direct [69-72] pulse shaping. Given the spectral transmission limitations of liquid crystal spatial light modulators (LC-SLMs), viable methods for mid-IR phase control incorporate one of the following [73]: a germanium (Ge) acousto-optic modulator (AOM) [69, 71, 74], a calomel-based acousto-optic programmable dispersive filter (AOPDF) [70], hollow-core fiber compression (HCF) [75] or a deformable mirror (DM) [72]. To date, the majority of mid-IR pulse shaping techniques have used pulses produced from OPA methods or modified OPCPA methods [40, 76]. To facilitate the ultrafast experiments, we report the demonstration of active compression of BBIR continuum pulses. Building on our work to generate a BBIR source and test its spectral tunability across λ = 2.5–8 μm [45], we incorporate a DM grating-based pulse compressor [72, 77, 78] to achieve nearly transform-limited (TL) BBIR pulses. The DM compressor, which uses an iterative genetic algorithm with optical feedback, enables smooth variations in phase while maintaining high compressor throughput across a spectral range dependent only on the DM metallic reflective coating. For varying spectral centers and material compensation conditions of the BBIR pulses, we present and analyze the performance of the DM pulse shaper with algorithmic pulse compression. Compression yields nearly transform limited BBIR pulses of 21 fs, or ~1.4 optical

cycles at the center frequency, as measured by cross-correlation frequency resolved optical gating. Approaching the transform limit afforded by the spectral bandwidth of the BBIR source opens up numerous possibilities for the use of these pulses probes in experiments aimed at understanding the vibrational degrees of freedom in hydrogen bonded systems.

1.5 Hydrogen bonding model systems:

Following the successful generation and compression of our broadband ultrashort mid-IR pulse, pump-probe experiments were performed on model hydrogen bonding systems to study the vibrational landscape of the systems. Two hydrogen bonded systems 10-Hydroxybenzo[h]quinolone (HBQ) and 2-(2′-Hydroxyphenyl)benzothiazole (HBT) was studied using spectrally dispersed infrared pump-probe spectroscopy. Previous experiments on HBQ done by Chou et al, included steady-state absorption as well as femtosecond fluorescence and transient absorption pump-probe studies in non-polar solvents to gather information on the excited state intramolecular proton transfer [ESIPT]. They were able to observe an enol to keto tautomerization reaction signified by a 30 nm red shift of the fluorescence signal. From the vibrational analysis of their results, they were able to elucidate low frequency skeletal modes modulating the donor group and acceptor group distance of the HBQ structure that play a significant role in the ESIPT. In particular they indicated an in-plane bending mode at 230-250 cm^{-1} [79, 80]. Time resolved fluorescence signal of the keto state in HBQ shows that the proton transfer to the keto isomer occurs within 13 fs and a longer 300 fs time scale corresponds to internal conversion from the keto isomer to the enol isomer[81],[82]. Excited state dynamics simulation reveals that the proton transfer is highly dependent on the backbone displacement [83],73].

Photophysics of HBT show that the molecule undergoes proton coupled electron transfer (PCET) where the ESIPT is coupled to electron transfer through the double bond connecting the rings. [84] Studies on HBT involved directly observing the photoinduced enol-keto tautomerization in nonpolar solvent by using a UV pump/IR pump probe spectroscopy. The transient IR study was able to directly monitor the excited state formed by the cleavage of O-H bond by monitoring the formation of the C=O stretch [85]. Similar to HBQ, HBT the molecule undergoes internal conversion to the enol state after the ESIPT to the keto isomer[86]. ESIPT in HBT has also been observed in various different solvents, including polar and nonpolar solvents and the results indicate that in the nonpolar solvents, the proton transfer occurs within 120 fs facilitating the formation of keto state. In contrast, polar solvents motivated by twisting structural motions allowed the formation of enol state or the keto triplet state[87]. The phototautomerization process has also been studied theoretically and shows that the proton transfer mechanism is extremely fast (<40 fs) and the differences in skeletal geometry of HBT and HBQ plays a very important role in the dynamics of the proton transfer [88]. Computational analysis of structural modes for HBT point to different skeletal deformations that play a very important role in the ESIPT (113 cm^{-1}, 255 cm^{-1}, 289 cm^{-1} and 528 cm^{-1}) [89, 90]. In contrast, the Resonance Raman analysis shows that 293 cm-1 and 299 cm-1 mode was identified as contributing to the proton transfer[91]. An example of the photophysics mechanism of the ESIPT is shown in Figure 1.6.

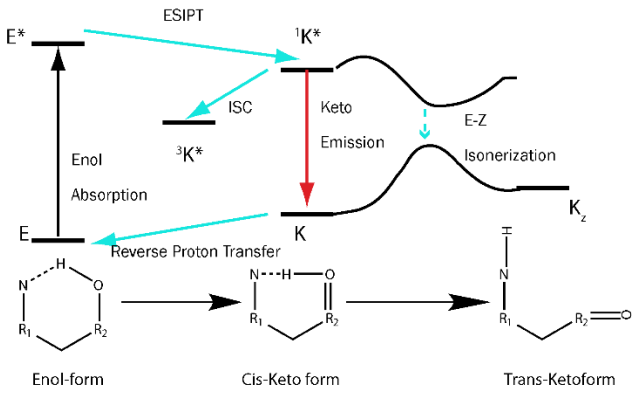

Figure 1.6: Basic Photophysics of ESIPT process illustrating the enol-keto tautaumerisation mechanism involving an intramolecular hydrogen bonding system. Adapted from Jianzhang Zhao et,al [92].

Vibrational study of versions of HBQ and HBT focusing on the intramolecular hydrogen bonding has not been reported. The deuterated version of the HBT (DBT) in toluene has been studied using femtosecond pump probe and the results show an oscillatory change in the OD stretching mode that is related to 118 cm^{-1}. This wave packet motion has been attributed with a low frequency mode that modulated the length of the hydrogen bond (OD band) [93]. This results follow in the footsteps of various computational and excited state studies that has been done as mentioned previously. While vibrational ground state studies have not been done on HBQ or the deuterated versions, the excited state studies as well as computational work done point to the presence of strong coupling of the OH stretching motion to low frequency structural motions.

There have not been studies done directly studying the intramolecular ground state hydrogen bonding dynamics in HBQ and HBT. This work aims to study ground state vibrational spectroscopy of the model systems by monitoring the ν_{OH} and the previously developed broad band mid-IR source is implemented in these experiments. The broad nature of the source gives

us the ability to probe across the fundamental and the overtone region. We were able to elucidate the various structural modes that are coupled to the fundamental νOH stretch and were able to further our understanding of the structural dynamics of intramolecular hydrogen bond.

1.6 Dissertation Overview:

This dissertation includes the technical details involved in the generation and compression of a tunable broadband IR source and the implementation of the source on highly anharmonic hydrogen bonded systems that exhibit intramolecular hydrogen bonding. Chapter 2 describes the development of the BBIR source and the *4f* deformable mirror compressor built to correct the field of the pulse. Detailed field characterization of the pulse as well as comparative improvement in the pulse shape is included in the chapter. Chapter 3 describes the isotropic pump-probe studies utilizing the compressed BBIR source on both HBQ and HBT systems in non-polar solvent and analysis of the ground state dynamics. Additionally anharmonic computational methods performed and the results of the computational analysis are also outlined in the chapter. Chapter 4 describes the brief work done on the deuterated counterpart for the HBQ model system and initial analysis of the isotope effect is included.

References:

1. J. M. Berg, J. L. Tymoczko, and L. Stryer, *Biochemistry* (W. H. Freeman, 2010).
2. C. Tommos and G. T. Babcock, "Proton and hydrogen currents in photosynthetic water oxidation," Biochimica et Biophysica Acta (BBA) - Bioenergetics 1458, 199-219 (2000).
3. D. Voet and J. G. Voet, *Biochemistry, 4th Edition* (John Wiley & Sons, 2010).
4. G. A. Jeffrey and W. Saenger, "The Importance of Hydrogen Bonds," in *Hydrogen Bonding in Biological Structures*, G. A. Jeffrey and W. Saenger, eds. (Springer Berlin Heidelberg, Berlin, Heidelberg, 1991), pp. 3-14.
5. N. Rawat and P. Biswas, "Hydrogen bond dynamics in intrinsically disordered proteins," The journal of physical chemistry. B 118, 3018-3025 (2014).
6. J. Fossey, D. Lefort, and J. Sorba, Free Radicals in Organic Chemistry (1993).
7. J. R. Cheeseman, M. T. Carroll, and R. F. W. Bader, "The mechanics of hydrogen bond formation in conjugated systems," Chemical Physics Letters 143, 450-458 (1988).
8. S. Wang, Z. Wang, and C. Hao, "Role of intramolecular hydrogen bonding in the excited-state intramolecular double proton transfer (ESIDPT) of calix[4]arene: A TDDFT study," Open Physics 14(2016).
9. J.-J. Zheng, Y.-Q. Lu, P.-L. Li, and C. Tao, "All-optical switching effect of the excited state proton transfer molecule 2-(2'-hydroxyphenyl) benzothiazole in different polar solvents," Wuli Xuebao 59, 6626-6631 (2010).
10. J. Ma, J. Zhao, P. Yang, D. Huang, C. Zhang, and Q. Li, "New excited state intramolecular proton transfer (ESIPT) dyes based on naphthalimide and observation of long-lived triplet excited states," Chem Commun (Camb) 48, 9720-9722 (2012).
11. E. T. J. Nibbering and T. Elsaesser, "Ultrafast Vibrational Dynamics of Hydrogen Bonds in the Condensed Phase," Chemical Reviews 104, 1887-1914 (2004).
12. T. F. Markle and J. M. Mayer, "Concerted Proton–Electron Transfer in Pyridylphenols: The Importance of the Hydrogen Bond," Angewandte Chemie International Edition 47, 738-740 (2008).
13. T. F. Markle, I. J. Rhile, A. G. DiPasquale, and J. M. Mayer, "Probing concerted proton–electron transfer in phenol–imidazoles," Proceedings of the National Academy of Sciences (2008).
14. J. M. Mayer, "PROTON-COUPLED ELECTRON TRANSFER: A Reaction Chemist's View," Annual Review of Physical Chemistry 55, 363-390 (2004).
15. J. M. Mayer, "Simple Marcus-Theory-Type Model for Hydrogen-Atom Transfer/Proton-Coupled Electron Transfer," The Journal of Physical Chemistry Letters 2, 1481-1489 (2011).
16. I. J. Rhile, T. F. Markle, H. Nagao, A. G. DiPasquale, O. P. Lam, M. A. Lockwood, K. Rotter, and J. M. Mayer, "Concerted Proton−Electron Transfer in the Oxidation of Hydrogen-Bonded Phenols," Journal of the American Chemical Society 128, 6075-6088 (2006).
17. M. Wikstrom, "Identification of the electron transfers in cytochrome oxidase that are coupled to proton-pumping," Nature 338, 776-778 (1989).
18. T. Kolev, "Influence of intermolecular hydrogen bonding on IR-spectroscopic properties of (R)-(−)-1-phenylglycinium hydrogen squarate monohydrate in solid-state. IR-LD, Raman spectroscopy and theoretical study," Journal of Molecular Structure 846, 139-146 (2007).
19. B. Kuhn, P. Mohr, and M. Stahl, "Intramolecular hydrogen bonding in medicinal chemistry," Journal of medicinal chemistry 53, 2601-2611 (2010).
20. J. C. Wright, "Multiresonant Coherent Multidimensional Spectroscopy," Annual Review of Physical Chemistry 62, 209-230 (2011).
21. P. B. Petersen, S. T. Roberts, K. Ramasesha, D. G. Nocera, and A. Tokmakoff, "Ultrafast N−H Vibrational Dynamics of Cyclic Doubly Hydrogen-Bonded Homo- and Heterodimers," The Journal of Physical Chemistry B 112, 13167-13171 (2008).

22. M. Rini, A. Kummrow, J. Dreyer, E. T. J. Nibbering, and T. Elsaesser, "Femtosecond mid-infrared spectroscopy of condensed phase hydrogen-bonded systems as a probe of structural dynamics," Faraday Discuss. 122, 27-40 (2002).
23. G. M. Sando, Q. Zhong, and J. C. Owrutsky, "Vibrational and rotational dynamics of cyanoferrates in solution," The Journal of Chemical Physics 121, 2158-2168 (2004).
24. M. Asselin and C. Sandorfy, "A low temperature infrared study of the band-width and frequency in self-associated alcohols," Chem. Phys. Lett. 8, 601 (1971).
25. M. Asselin and C. Sandorfy, "Double Excitation in the Infrared Spectra of Self-Associated Alcohols," The Journal of Chemical Physics 52, 6130-6134 (1970).
26. J. Joseph and E. D. Jemmis, "Red-, blue-, or no-shift in hydrogen bonds: a unified explanation," J Am Chem Soc 129, 4620-4632 (2007).
27. R. Costard, C. Greve, H. Fidder, and E. T. Nibbering, "Hydrogen bonding induced enhancement of Fermi resonances: ultrafast vibrational energy flow dynamics in aniline-d(5)," The journal of physical chemistry. B 119, 2711-2725 (2015).
28. N. Sheppard, "Infrared Spectroscopy and Hydrogen Bonding — Band-Widths and Frequency Shifts," 85-105 (1959).
29. H. L. Clever, "Hydrogen bond: Recent developments in theory and experimental. volume I: theory, volume II: structure and spectroscopy, volume III: dynamics, thermodynamics and special systems (Schuster P.)," Journal of Chemical Education 55, A244 (1978).
30. A. Tokmakoff and M. D. Fayer, "Infrared Photon Echo Experiments: Exploring Vibrational Dynamics in Liquids and Glasses," Acc Chem Res 28, 437-445 (2002).
31. N. Huse, K. Heyne, J. Dreyer, E. T. J. Nibbering, and T. Elsaesser, "Vibrational Multilevel Quantum Coherence due to Anharmonic Couplings in Intermolecular Hydrogen Bonds," Physical Review Letters 91, 197401 (2003).
32. T. Elsaesser, N. Huse, J. Dreyer, J. R. Dwyer, K. Heyne, and E. T. J. Nibbering, "Ultrafast vibrational dynamics and anharmonic couplings of hydrogen-bonded dimers in solution," Chemical Physics 341, 175-188 (2007).
33. K. Heyne, N. Huse, J. Dreyer, E. T. J. Nibbering, T. Elsaesser, and S. Mukamel, "Coherent low-frequency motions of hydrogen bonded acetic acid dimers in the liquid phase," The Journal of Chemical Physics 121, 902-913 (2004).
34. S. Yamaguchi, M. Banno, K. Ohta, K. Tominaga, and T. Hayashi, "Vibrational dynamics of benzoic acid in nonpolar solvents studied by subpicosecond infrared pump–probe spectroscopy," Chemical Physics Letters 462, 238-242 (2008).
35. D. Fayer, *Ultrafast Infrared And Raman Spectroscopy* (Taylor & Francis, 2001).
36. A. Tokmakoff and M. D. Fayer, "Infrared Photon Echo Experiments: Exploring Vibrational Dynamics in Liquids and Glasses," Accounts of Chemical Research 28, 437-445 (1995).
37. R. A. Kaindl, M. Wurm, K. Reimann, P. Hamm, A. M. Weiner, and M. Woerner, "Generation, shaping, and characterization of intense femtosecond pulses tunable from 3 to 20 mm," J. Opt. Soc. Am. B 17, 2086-2094 (2000).
38. C. J. Fecko, J. J. Loparo, and A. Tokmakoff, "Generation of 45 femtosecond pulses at 3 mm with a $KNbO_3$ optical parametric amplifier," Opt. Commun. 241, 521-528 (2004).
39. J. Biegert, P. K. Bates, and O. Chalus, "New Mid-Infrared Light Sources," IEEE Journal of Selected Topics in Quantum Electronics 18, 531-540 (2012).
40. M. Baudisch, H. Pires, H. Ishizuki, T. Taira, M. Hemmer, and J. Biegert, "Sub-4-optical-cycle, 340 MW peak power, high stability mid-IR source at 160 kHz," Journal of Optics 17, 094002 (2015).
41. A. M. Stingel, H. Vanselous, and P. B. Petersen, "Covering the vibrational spectrum with microjoule mid-infrared supercontinuum pulses in nonlinear optical applications," Journal of the Optical Society of America B 34, 1163 (2017).

42. T. Fuji and T. Suzuki, "Generation of sub-two-cycle mid-infrared pulses by four-wave mixing through filamentation in air," Opt. Lett. 32, 3330-3332 (2007).
43. P. B. Petersen and A. Tokmakoff, "Source for ultrafast continuum infrared and terahertz radiation," Opt. Lett. 35, 1962-1964 (2010).
44. C. R. Baiz and K. J. Kubarych, "Ultrabroadband detection of a mid-IR continuum by chirped-pulse upconversion," Opt. Lett. 36, 187-189 (2011).
45. M. Cheng, A. Reynolds, H. Widgren, and M. Khalil, "Generation of tunable octave-spanning mid-infrared pulses by filamentation in gas media," Opt. Lett. 37, 1787-1789 (2012).
46. Y. Nomura, H. Shirai, K. Ishii, N. Tsurumachi, A. A. Voronin, A. M. Zheltikov, and T. Fuji, "Phase-stable sub-cycle mid-infrared conical emission from filamentation in gases," Opt. Express 20, 24741-24747 (2012).
47. Y. Nomura, Y. T. Wang, T. Kozai, H. Shirai, A. Yabushita, C. W. Luo, S. Nakanishi, and T. Fuji, "Single-shot detection of mid-infrared spectra by chirped-pulse upconversion with four-wave difference frequency generation in gases," Opt. Express 21, 18249-18254 (2013).
48. D. J. Cook and R. M. Hochstrasser, "Intense terahertz pulses by four-wave rectification in air," Opt. Lett. 25, 1210-1212 (2000).
49. X. Xie, J. M. Dai, and X. C. Zhang, "Coherent control of THz wave generation in ambient air," Phys. Rev. Lett. 96, 075005 (2006).
50. M. D. Thomson, M. Kress, T. Loffler, and H. G. Roskos, "Broadband THz emission from gas plasmas induced by femtosecond optical pulses: From fundamentals to applications," Laser Photonics Rev. 1, 349-368 (2007).
51. K. Y. Kim, A. J. Taylor, J. H. Glownia, and G. Rodriguez, "Coherent control of terahertz supercontinuum generation in ultrafast laser-gas interactions," Nat. Photon. 2, 605-609 (2008).
52. F. Theberge, M. Chateauneuf, G. Roy, P. Mathieu, and J. Dubois, "Generation of tunable and broadband far-infrared laser pulses during two-color filamentation," Phys. Rev. A 81(2010).
53. P. Whalen, J. V. Moloney, and M. Kolesik, "Self-focusing collapse distance in ultrashort pulses and measurement of nonlinear index," Opt Lett 36, 2542-2544 (2011).
54. D. E. Laban, W. C. Wallace, R. D. Glover, R. T. Sang, and D. Kielpinski, "Self-focusing in air with phase-stabilized few-cycle light pulses," Opt Lett 35, 1653-1655 (2010).
55. S. L. Chin, T. J. Wang, C. Marceau, J. Wu, J. S. Liu, O. Kosareva, N. Panov, Y. P. Chen, J. F. Daigle, S. Yuan, A. Azarm, W. W. Liu, T. Seideman, H. P. Zeng, M. Richardson, R. Li, and Z. Z. Xu, "Advances in intense femtosecond laser filamentation in air," Laser Physics 22, 1-53 (2011).
56. M. R. Rashidian Vaziri, "Describing the propagation of intense laser pulses in nonlinear Kerr media using the ducting model," Laser Physics 23, 105401 (2013).
57. I. B. Burgess, W. E. Shimmell, and K. Saravanamuttu, "Spontaneous pattern formation due to modulation instability of incoherent white light in a photopolymerizable medium," J Am Chem Soc 129, 4738-4746 (2007).
58. T. Schneider, "Self- and Cross-Phase Modulation," 143-165 (2004).
59. K. Dolgaleva, W. C. Ng, L. Qian, J. S. Aitchison, M. C. Camasta, and M. Sorel, "Broadband self-phase modulation, cross-phase modulation, and four-wave mixing in 9-mm-long AlGaAs waveguides," Opt Lett 35, 4093-4095 (2010).
60. A. Galvanauskas, M.-Y. Cheng, K.-C. Hou, and K.-H. Liao, "High Peak Power Pulse Amplification in Large-Core Yb-Doped Fiber Amplifiers," IEEE Journal of Selected Topics in Quantum Electronics 13, 559-566 (2007).
61. N. Demirdoven, M. Khalil, O. Golonzka, and A. Tokmakoff, "Dispersion compensation with optical materials for compression of intense sub-100-fs mid-infrared pulses," Opt. Lett. 27, 433-435 (2002).
62. C. Calabrese, A. M. Stingel, L. Shen, and P. B. Petersen, "Ultrafast continuum mid-infrared spectroscopy: probing the entire vibrational spectrum in a single laser shot with femtosecond time resolution," Opt. Lett. 37, 2265-2267 (2012).

63. L. De Marco, K. Ramasesha, and A. Tokmakoff, "Experimental Evidence of Fermi Resonances in Isotopically Dilute Water from Ultrafast Broadband IR Spectroscopy," J. Phys. Chem. B 117, 15319-15327 (2013).
64. A. M. Stingel, C. Calabrese, and P. B. Petersen, "Strong Intermolecular Vibrational Coupling through Cyclic Hydrogen-Bonded Structures Revealed by Ultrafast Continuum Mid-IR Spectroscopy," J. Phys. Chem. B 117, 15714-15719 (2013).
65. C. R. Baiz and K. J. Kubarych, "Ultrabroadband detection of a mid-IR continuum by chirped-pulse upconversion," Opt Lett 36, 187-189 (2011).
66. N. Demirdöven, M. Khalil, O. Golonzka, and A. Tokmakoff, "Dispersion compensation with optical materials for compression of intense sub-100-fs mid-infrared pulses," Opt. Lett. 27, 433 (2002).
67. N. Belabas, J. P. Likforman, L. Canioni, B. Bousquet, and M. Joffre, "Coherent broadband pulse shaping in the mid infrared," Opt. Lett. 26, 743-745 (2001).
68. H. S. Tan and W. S. Warren, "Mid infrared pulse shaping by optical parametric amplification and its application to optical free induction decay measurement," Opt. Express 11, 1021-1028 (2003).
69. S. H. Shim, D. B. Strasfeld, E. C. Fulmer, and M. T. Zanni, "Femtosecond pulse shaping directly in the mid-IR using acousto-optic modulation," Opt. Lett. 31, 838-840 (2006).
70. R. Maksimenka, P. Nuernberger, K. F. Lee, A. Bonvalet, J. Milkiewicz, C. Barta, M. Klima, T. Oksenhendler, P. Tournois, D. Kaplan, and M. Joffre, "Direct mid-infrared femtosecond pulse shaping with a calomel acousto-optic programmable dispersive filter," Opt. Lett. 35, 3565-3567 (2010).
71. J. M. Nite, J. D. Cyran, and A. T. Krummel, "Active Bragg angle compensation for shaping ultrafast mid-infrared pulses," Opt. Express 20, 23912-23920 (2012).
72. A. Cartella, S. Bonora, M. Forst, G. Cerullo, A. Cavalleri, and C. Manzoni, "Pulse shaping in the mid-infrared by a deformable mirror," Opt. Lett. 39, 1485-1488 (2014).
73. A. M. Weiner, "Ultrafast optical pulse shaping: A tutorial review," Opt. Commun. 284, 3669-3692 (2011).
74. A. Ghosh, A. L. Serrano, T. A. Oudenhoven, J. S. Ostrander, E. C. Eklund, A. F. Blair, and M. T. Zanni, "Experimental implementations of 2D IR spectroscopy through a horizontal pulse shaper design and a focal plane array detector," Optics Letters 41, 524-527 (2016).
75. V. Cardin, N. Thiré, S. Beaulieu, V. Wanie, F. Légaré, and B. E. Schmidt, "0.42 TW 2-cycle pulses at 1.8 μm via hollow-core fiber compression," Applied Physics Letters 107, 181101 (2015).
76. H. Liang, P. Krogen, R. Grynko, O. Novak, C.-L. Chang, G. J. Stein, D. Weerawarne, B. Shim, F. X. Kärtner, and K.-H. Hong, "Three-octave-spanning supercontinuum generation and sub-two-cycle self-compression of mid-infrared filaments in dielectrics," Opt. Lett. 40, 1069-1072 (2015).
77. E. Zeek, K. Maginnis, S. Backus, U. Russek, M. Murnane, G. Mourou, H. Kapteyn, and G. Vdovin, "Pulse compression by use of deformable mirrors," Opt. Lett. 24, 493-495 (1999).
78. A. Baltuska and T. Kobayashi, "Adaptive shaping of two-cycle visible pulses using a flexible mirror," Appl. Phys. B 75, 427-443 (2002).
79. P.-T. Chou, Y.-C. Chen, W.-S. Yu, Y.-H. Chou, C.-Y. Wei, and Y.-M. Cheng, "Excited-State Intramolecular Proton Transfer in 10-Hydroxybenzo[h]quinoline," The Journal of Physical Chemistry A 105, 1731-1740 (2001).
80. S. Takeuchi and T. Tahara, "Coherent Nuclear Wavepacket Motions in Ultrafast Excited-State Intramolecular Proton Transfer: Sub-30-fs Resolved Pump-Probe Absorption Spectroscopy of 10-Hydroxybenzo[h]quinoline in Solution," J. Phys. Chem. A 109, 10199-10207 (2005).
81. C. H. Kim and T. Joo, "Coherent excited state intramolecular proton transfer probed by time-resolved fluorescence," Phys. Chem. Chem. Phys. 11, 10266-10269 (2009).
82. J. Lee and T. Joo, "Photophysical model of 10-hydroxybenzo[h]quinoline: internal conversion and excited state intramolecular proton transfer," Bull. Korean Chem. Soc. 35, 881-885 (2014).

83. M. Higashi and S. Saito, "Direct Simulation of Excited-State Intramolecular Proton Transfer and Vibrational Coherence of 10-Hydroxybenzo[h]quinoline in Solution," J. Phys. Chem. Lett. 2, 2366-2371 (2011).
84. S. Luber, K. Adamczyk, E. T. J. Nibbering, and V. S. Batista, "Photoinduced Proton Coupled Electron Transfer in 2-(2′-Hydroxyphenyl)-Benzothiazole," The Journal of Physical Chemistry A 117, 5269-5279 (2013).
85. O. F. Mohammed, S. Luber, V. S. Batista, and E. T. J. Nibbering, "Ultrafast Branching of Reaction Pathways in 2-(2′-Hydroxyphenyl)benzothiazole in Polar Acetonitrile Solution," The Journal of Physical Chemistry A 115, 7550-7558 (2011).
86. S. Pijeau, D. Foster, and E. G. Hohenstein, "Excited-State Dynamics of 2-(2'-Hydroxyphenyl)benzothiazole: Ultrafast Proton Transfer and Internal Conversion," J. Phys. Chem. A 121, 4595-4605 (2017).
87. S. M. Aly, A. Usman, M. AlZayer, G. A. Hamdi, E. Alarousu, and O. F. Mohammed, "Solvent-Dependent Excited-State Hydrogen Transfer and Intersystem Crossing in 2-(2'-Hydroxyphenyl)-Benzothiazole," J. Phys. Chem. B 119, 2596-2603 (2015).
88. P.-T. Chou, G.-R. Wu, Y.-I. Liu, W.-S. Yu, and C.-S. Chiou, "Proton-Transfer Tautomerism in 10-Hydroxybenzo[h]quinolines: Heavy Atom Effects and Non-Hydrogen-Bonded Photorotamer Formation in 77 K Glassy Matrixes," J. Phys. Chem. A 106, 5967-5973 (2002).
89. R. De Vivie-Riedle, V. De Waele, L. Kurtz, and E. Riedle, "Ultrafast Excited-State Proton Transfer of 2-(2'-Hydroxyphenyl)benzothiazole: Theoretical Analysis of the Skeletal Deformations and the Active Vibrational Modes," J. Phys. Chem. A 107, 10591-10599 (2003).
90. C. Schriever, K. Stock, A. J. A. Aquino, D. Tunega, S. Lochbrunner, E. Riedle, R. de Vivie-Riedle, and H. Lischka, "The interplay of skeletal deformations and ultrafast excited-state intramolecular proton transfer: Experimental and theoretical investigation of 10-hydroxybenzo[h]quinoline," Chem. Phys. 347, 446-461 (2008).
91. M. Pfeiffer, K. Lenz, A. Lau, and T. Elsaesser, "Resonance Raman studies of heterocyclic aromatic compounds showing ultrafast intramolecular proton transfer," J. Raman Spectrosc. 26, 607-615 (1995).
92. J. Zhao, S. Ji, Y. Chen, H. Guo, and P. Yang, "Excited state intramolecular proton transfer (ESIPT): from principal photophysics to the development of new chromophores and applications in fluorescent molecular probes and luminescent materials," Physical chemistry chemical physics : PCCP 14, 8803-8817 (2012).
93. D. Madsen, J. Stenger, J. Dreyer, E. T. J. Nibbering, P. Hamm, and T. Elsaesser, "Coherent vibrational ground-state dynamics of an intramolecular hydrogen bond," Chemical Physics Letters 341, 56-62 (2001).

Chapter 2: Development and compression of Tunable Broadband Mid-IR Pulses: Using a Deformable Mirror Pulse Shaper

2.1 Summary:

To improve the utility of ultrafast infrared spectroscopy experiments, we have developed and actively compressed a tunable broadband mid-infrared (BBIR) source. The octave-spanning BBIR source is generated by a filamentation process of 800 nm and 400 nm pulses in a pressurized gas cell. To correct the higher-order dispersion effects in BBIR pulses, we have introduced a deformable mirror grating compressor, which uses an iterative genetic algorithm with optical feedback. Compression yields nearly transform limited BBIR pulses of 21 fs, or ~1.4 optical cycles at the center frequency, as measured by cross-correlation frequency resolved optical gating. Detailed experimental details are outlined in the Appendix for chapter 2.

2.2 Experiment:

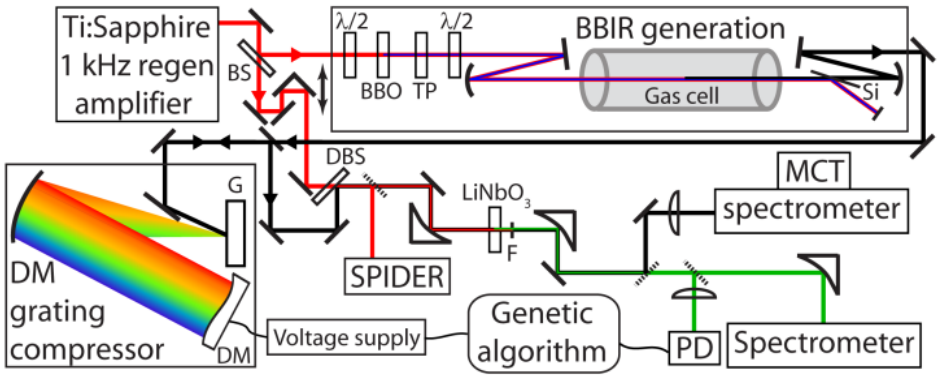

Figure 2.**1**: Experimental layout. BBIR is generated in a pressurized gas cell and enters a deformable mirror (DM) compressor. BBIR is upconverted with a SPIDER-characterized 800 nm reference pulse for detection in either a photodiode (PD) for genetic algorithm compression feedback or a spectrometer for XFROG characterization. BS: dielectric beam splitter; λ/2: half-wave plate at 800 nm; TP: calcite timing plate; Si: 250 μm silicon; DBS: gold dichroic beam splitter; G: grating; F: 750 nm short-pass filter.

The experimental layout of the generation, compression, and characterization of the BBIR pulses is

shown in Figure 2.. The pulses in this experiment originate from the output of a Spectra Physics XP Pro Ti:Sapphire regenerative amplifier (1 kHz, 800 nm, 35 fs, 3.6 W). We have previously detailed the BBIR generation process [1] . Briefly, a 2.5 mJ portion of the amplifier output is frequency doubled in a 100-μm thick Type I BBO crystal. The collinear fundamental and frequency-doubled pulses are matched in time delay and polarization using a birefringent calcite crystal and a dual waveplate, respectively, and are focused with a concave mirror (f = 1 m) into a pressurized gas cell. In this experiment, the 1.2 m stainless steel gas cell is sealed with a 1-mm thick antireflection (AR) coated fused silica window at the entrance and a 1-mm thick BaF_2 window at the exit. The BBIR beam is isolated by transmission through a 250-μm thick silicon (Si) wafer at Brewster's angle before being collimated. Not shown in the BBIR path in Fig. 2.1 are a second 250-μm Brewster's angle Si wafer to join a HeNe tracer beam and a reflective telescope to resize the BBIR beam to 15 mm diameter ($1/e^2$). We have reported the spectral tunability of BBIR with selection of gas and pressure in the cell [45]. In this work, the cell contains air at pressures of 650, 760, and 900 Torr. With increasing pressure, the spectrum of the BBIR is blue-shifted and the pulse energy increases. The resulting BBIR pulse spectra shown in Figure 2.2(a) are dispersed with a 0.19 m spectrometer (Triax 190, Horiba Jobin Yvon, 75 grooves/mm grating blazed at 4.65 μm) following a band pass filter (either 2.5–5.1 μm or 4.5–8.5 μm) to eliminate the higher diffraction orders from the grating. A mercury cadmium telluride (MCT) array detector (IR0144, Infrared Systems Development) is used to collect several spectral segments (spectrometer grating positions). The BBIR spectral center (ω_0), full width at 10% maximum spectral bandwidth ($\Delta\omega$) , and pulse energy at each pressure are as follows: ω_0 = 2000 cm^{-1}, $\Delta\omega$ = 1208 cm^{-1}, and 120 nJ at 650 Torr; ω_0 = 2300 cm^{-1}, $\Delta\omega$ = 1121 cm^{-1}, and 180 nJ at 760 Torr; and ω_0 =2600 cm^{-1}, $\Delta\omega$ = 1444 cm^{-1}, and 240 nJ at 900 Torr. The corresponding temporal intensity for the BBIR pulses, given in Fig. 2.2(b), is calculated by squaring the Fourier transform (FT) of the BBIR spectral field, $\sqrt{I(\omega)}$. The log plot of the normalized temporal intensity profile highlights the

broadened profile of the field as well as oscillations in the wings (~3% of the primary pulse) that can e expected from the structured BBIR spectrum with a dip from atmospheric CO_2 absorption at ~2350 cm^{-1}.

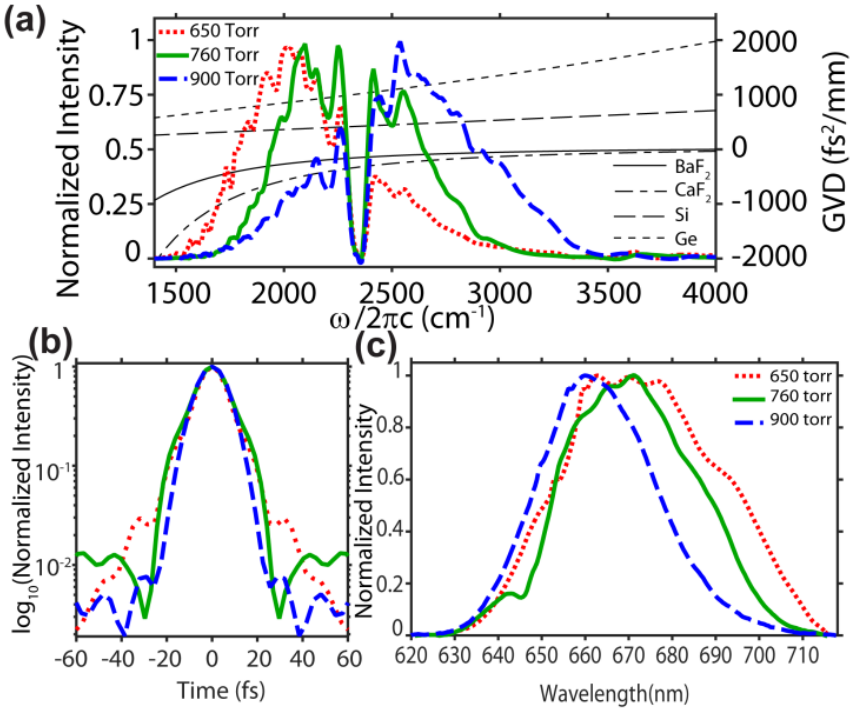

Figure **2**.2: (a) BBIR spectra collected for three pressures of air (thick traces, left axis). The dip at ~2350 cm-1 is due to atmospheric CO2 absorption. The black traces (right axis) are the GVD curves of various materials used over the BBIR spectral range. (b) FT of the spectra generated at the three pressures of air in (a) to give the corresponding transform-limited temporal intensity profiles with durations of 15 fs (650 Torr), 16 fs (760 Torr), and 16.5 fs (900 Torr). The normalized temporal intensity of the electric field is plotted on a log scale. (c) The integrations over τ of XFROG traces show a frequency shift with pressure in upconverted spectra similar to that in BBIR pulse spectra (a).

XFROG is a technique for the complete characterization of pulses, i.e. for measuring time dependent electric field and the spectral phase and was used to analyses the electric field. The compression and characterization of the BBIR pulses rely on the sum frequency generation (SFG) of BBIR pulses with reference pulses, which originate from a 2 μJ portion of the 800 nm amplifier output (Fig. 2.1). The time delay, τ, between the BBIR and reference pulses is adjusted with a computer controlled translation stage (Newport, XMS100). A gold dichroic beam splitter (ISP optics, BSP-DI-50-2) joins the beams in a collinear fashion, after which the reference beam can be routed to a SPIDER characterization setup for full electric field reconstruction [2][94].

An off-axis parabolic mirror (f=101.5 mm) focuses the BBIR and reference beams to a 100-μm thick Type I lithium niobate crystal to generate the $\omega_{BBIR} + \omega_{800}$ nm SFG signal. SFG spectra from integrated XFROG projections (Fig 2.2(c)) demonstrate the phase-matching bandwidth of the crystal as well as the blue-shift of the BBIR spectra (Fig. 2.2(a)) with increasing pressure. An interative phase retrievel algorithm, implemented as a computer program, was then used for reconstructing the pulse shape from XFROG trace [3].

Figure **2.3**: Experimental setup for XFROG charachterization.

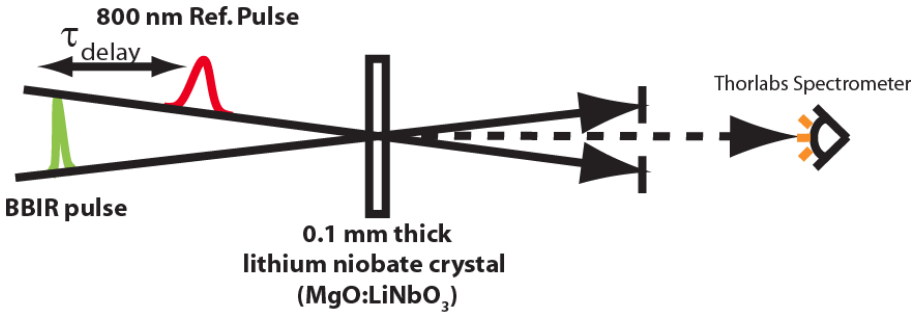

The retrieval algorithm requires the independent input of the electric field of the reference pulse (800nm). Another characterization technique using spectral interferometry, SPIDER was performed on the 800nm reference pulse to extract the electric field information. In this technique the test pulse is split into two identical copies with a significant temporal distance, so that there is no temporal overlap. Another pulse, derived from the same input pulse, is strongly temporally stretched. The long chirped pulse and the two copies of the signal pulse are then combined in a nonlinear crystal (BBO, Type I, 100um) where SFG occurs. The two signal pulses overlap with different temporal portions of the chirped pulse. The spectrum of the SFG signal reveals the temporally resolved group delay and the spectral phase.

To adaptively compress the BBIR pulses, we have constructed a grating compressor with a DM (Fig. 2.4). The 4-f geometry compressor consists of a reflective grating (40 grooves/mm), a gold-coated spherical mirror (f = 20.3 cm), and a DM spanning an octave of BBIR spectrum in the focal plane of the compressor. The DM (OKO Technologies) has 19 actuators under a gold-coated silicon nitride membrane that are computer controlled with an external voltage supply (0 to 280 V; maximum deflection of mirror center = 10 μm).

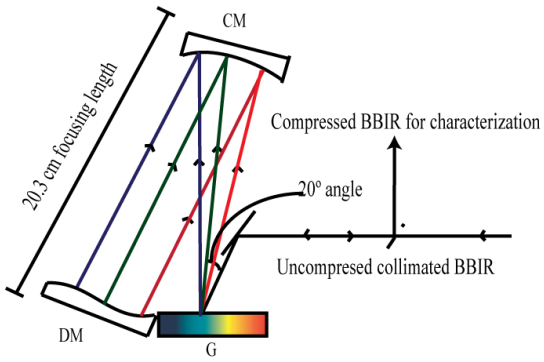

Figure **2**.4: 4f adaptive optic compressor design. G: 40 grooves/mm aluminum-coated grating, 2"x 2", blazed at 4.8 μm; CM: 3" diameter gold-coated curved (spherical) mirror, 8" f. l.; DM: linear 19 channel micro machined membrane deformable mirror, 11 x 39 cm, spanning 3-7 μm of spectral bandwidth with given G and CM f. l.

A genetic algorithm is used to optimize the surface of the DM for pulse compression through a feedback loop that maximizes the detected SFG intensity at τ=0. An initially random population of mirror conformations evolves to a fairly uniform population of optimized conformations for pulse compression in fewer than 10 minutes. The quantitative temporal characterization of the BBIR pulses uses the cross-correlation frequency resolved optical gating (XFROG) technique [3], which requires collection of the spectrally dispersed SFG signal with a spectrometer (ThorLabs CCS200) at a series of τ delays.

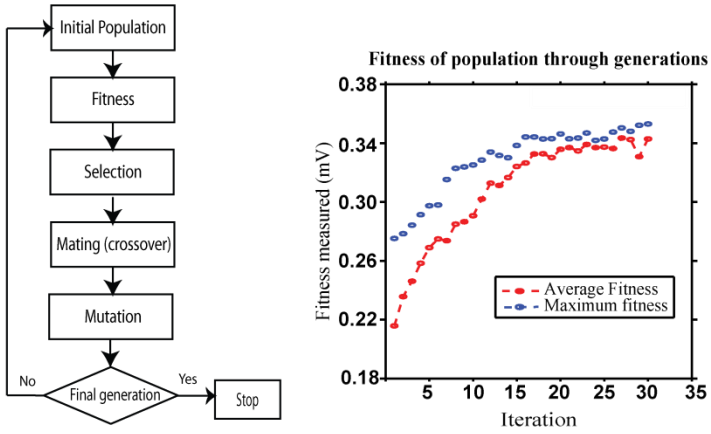

Figure 2.5: Diagram showing the genetic algorithm process for the mirror optimization and the fitness progression through the generation indicating the efficiency of genetic algorithm.

2.3 Results and Discussion:

The compression of the BBIR pulses involves a careful balance between material compensation and adaptive DM compression. BBIR pulses generated at each pressure of air are sent through materials with positive and negative GVD in the mid-IR (Fig. 2.2a) to provide an ideal rough dispersion correction for the DM compressor to refine. Coloumn IV corresponds to BBIR generated in 760 Torr air but with 1 mm Ge removed compared to column II. For each BBIR condition, XFROG traces are presented without compression (0 V applied applied to all DM actuators, Figs. 3(a-d)) and with optimized compression (Figs. 2.3(e-h)). Figures 2.3(i-l) are the reconstructed XFROG traces with the lowest XFROG error (<0.009 as computed with a 256x256 grid) generated from the XFROG algorithm for each BBIR generation condition. Figures 2.6(m-p) display the temporal electric fields recovered with the XFROG algorithm (Femtosecond Technologies, FROG 3.2.2) using the 800 nm reference electric field, which is characterized by SPIDER to have ~45 fs duration and 957 fs^2 group delay dispersion (GDD).

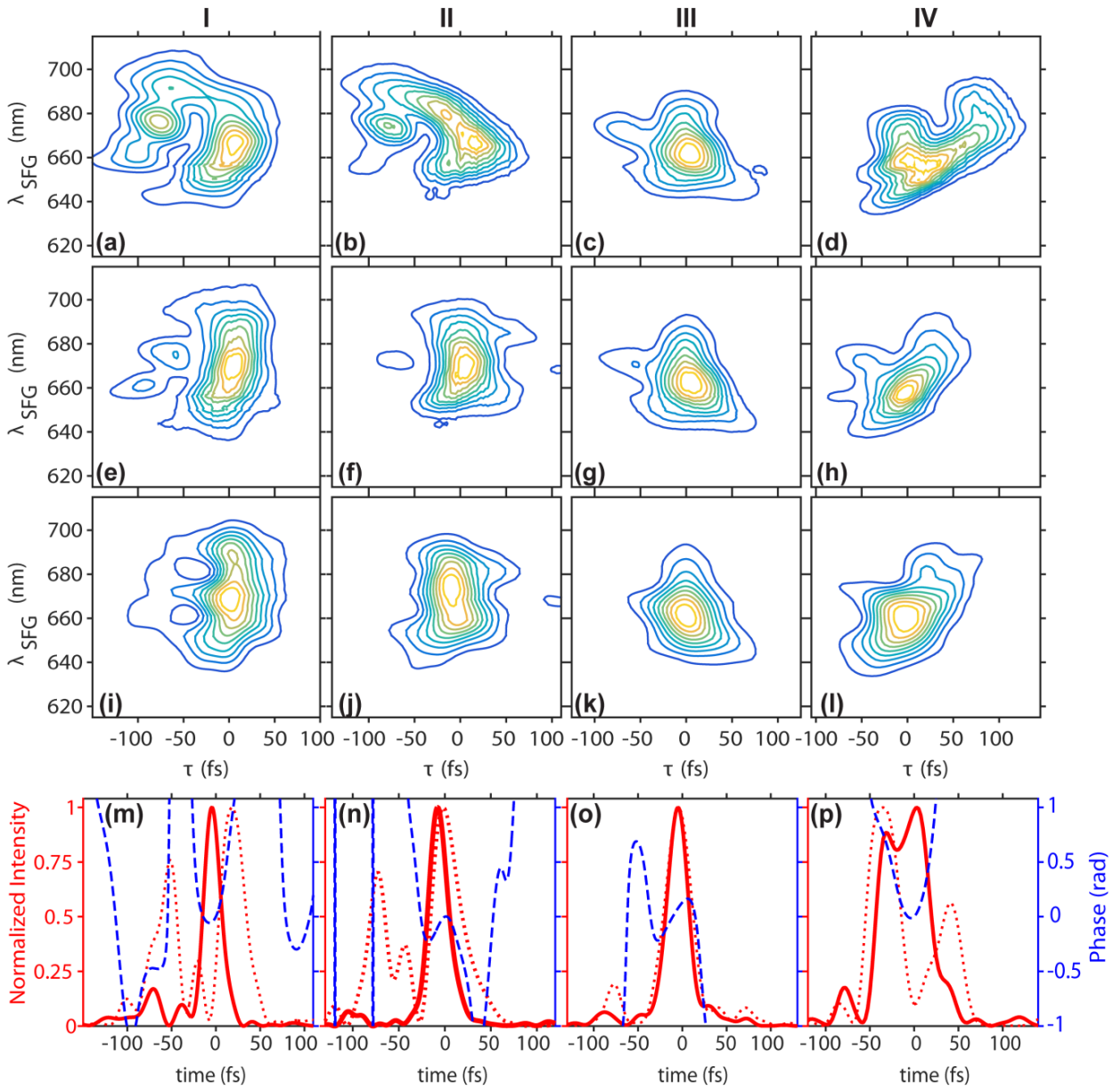

Figure 2.6: Summary of BBIR compression and characterization. Each column corresponds to a unique set of BBIR gas cell and material conditions: (I) 650 Torr air, (II) 760 Torr air, (III) 900 Torr air, and (IV) 760 torr air with 1 mm Ge removed from BBIR path. (a-d) XFROG ($\omega_{BBIR} + \omega_{800\ nm}$) traces at respective initial conditions with 0 V applied to all deformable mirror actuators, i.e., no adaptive-optic compression. (e-h) XFROG traces at respective initial conditions with DM compression optimized. (i-l) Reconstructed traces of the XFROG traces with DM compression (e-h) recovered from the algorithm. Contour lines indicate steps of 10%. (m-p) XFROG algorithm results: Reconstructed temporal electric field intensities for the unoptimized pulses (red dotted traces, left axes) and optimized pulses (red solid traces, left axes) are plotted with reconstructed temporal phases (blue dashed traces, right axes) for the optimized pulses.

The importance of specific BBIR path materials and the effectiveness of the DM pulse compression beyond material compensation differ for each BBIR spectrum. The materials in the BBIR path corresponding to columns I-III of Fig. 2.6 are identical and result in the shortest pulses after DM compression. In the most red-shifted spectrum (650 Torr air, column I), the diagonal tilt (Fig. 2.6(a)) and complicated XFROG shape indicate negative chirp and higher-order dispersion; algorithmic compression reduces these phase terms to result in a more vertical and singular peak (Fig. 2.6(e)). The initial BBIR pulse duration recovered by XFROG is 96 fs (Fig. 2.6(m), red dotted trace), and the compressed pulse duration is 22 fs (Fig. 2.6(m), red solid trace). The manipulation of the higher order dispersion terms by the DM can be seen in the reduction of the satellite pulses in the recovered electric field intensity by 77%. A similar improvement by the DM compressor is seen for the BBIR spectrum generated in 760 Torr air (column II), in which the strong linear tilt (positive chirp) and satellite pulses (Fig. 2.6(b)) are reduced by 93% (Fig. 2.6(f)) and the initial pulse duration of 100 fs is compressed to 21 fs (Fig. 2.6(n), red traces). For these two pressures, material compensation dictates the efficiency of the DM compression. This is demonstrated in column IV of Fig. 2.6 for the 760 Torr case with the removal of positively dispersive material to create a negative chirp (Fig. 2.6(d)). The starting pulse duration remains ~100 fs but is only compressed to 62 fs (Fig. 2.6(p), red traces), as the DM compressor leaves residual dispersion (Fig. 2.6(h)). The decrease in the satellite pulse intensity of the electric field is less significant (40%) than its comparative counterpart in column II. Finally, in the blue-shifted BBIR spectrum (900 Torr, column III), we are able to use material compensation more effectively for compression, as seen in the minimal tilt in Fig. 2.6(c). The recovered pulse duration is initially 34 fs and is optimized to 27 fs (Fig. 2.6(o), red traces) upon reducing some of satellite pulses by 66% (Fig. 2.6(g)) following DM compression. Here, the

uncompressed BBIR pulse upconversion and the efficiency of the DM compression are insensitive to small changes in material compensation. Removing 1 mm of Ge results in nearly identical XFROG traces to Figs. 2.6 (c, g) with BBIR pulse durations reduced from ~33 to 31 fs.

To assess the quality of the retrieved electric field information, the simulated XFROG traces for the compressed pulses are plotted alongside the experimental XFROG traces (Figs. 2.6(i-l)). A comparison of Figs. 2.6(e-h) and Figs. 2.6(i-l) reveals that most features of the experimental XFROG trace are quantitatively captured by the algorithm. For example, the satellite pulses in Fig. 2.6(e) are recovered in the simulated XFROG trace in Fig. 2.6(i). The positive chirp demonstrated by the pulses in Figs. 2.6(e,h) is also reproduced in the simulated XFROG traces in Figs. 2.6(i,l). The similarities in the experimental XFROG traces and the simulated XFROG traces point to the reliability of the retrieved electric field information from the XFROG algorithm.

The post-compression temporal profiles in Figs. 2.6(m–o) (red solid traces) contain minimal secondary pulses, and the pulse durations of 22 fs, 21 fs and 27 fs approach the FT limits of 15 fs, 16 fs, and 16.5 fs, derived from the Fig. 2.2(b) temporal profiles. Residual dispersion is evident in the retrieved temporal phases (blue dashed traces) in Figs. 2.6(m–o). In columns I-III, the temporal phases within the BBIR pulse envelopes exhibit mild quadratic (650 Torr, Fig. 2.6(m)) and cubic (760 and 900 Torr, Figs. 2.6(n, o)) phases. The recovered spectral phase, $\phi(\omega)$ for each case is fit to a Taylor expansion through the cubic phase term, centered at ω_0 and over a range $\Delta\omega$. From the quadratic and cubic terms, $\phi'' \cdot (\omega - \omega_0)^2 / 2$ and $\phi''' \cdot (\omega - \omega_0)^3 / 6$, we report the GDD ($\phi''$) and third-order dispersion (TOD, ϕ''') of the pulse. At 650 Torr, the DM compression results in half of ϕ''' compared to the uncompressed pulse and a reduction of ϕ'' to one quarter (1025 to 224 fs^2). At 760 Torr (column

II), ϕ''' is corrected by an order of magnitude while ϕ'' decreases from 768 to 28 fs^2. However, with only 1 mm Ge (column IV), DM compression decreases the magnitude of ϕ'' only slightly (-917 to -531 fs^2) and ϕ''' increases. Finally in the BBIR produced at 900 Torr (column III), ϕ''' mproves slightly and ϕ'' is corrected from 401 to 130 fs^2.

Column	I	II	III	IV
Pressure of Air in Gas cell	650 Torr	760 Torr	900 Torr	760 Torr
Material	2 mm Ge	2 mm Ge	2 mm Ge	1 mm Ge
Pulse Length before DM correction	96 fs	100 fs	34 fs	100 fs
Pulse Length after DM correction	22 fs	21 fs	27 fs	62 fs
GDD (φ") before DM correction	1025 fs^2	768 fs^2	401 fs^2	-917 fs^2
GDD (φ") after DM correction	224 fs^2	28 fs^2	130 fs^2	-531 fs^2

Table 2.1: Summary of results analyzing the efficiency of deformable mirror compressor

The reductions in GDD and TOD correspond to improvements in pulse durations and account for the changes of XFROG traces before and after DM compression (Fig. 2.6). The DM compressor performs best for red-shifted spectra with weakly negative GDD (columns I-II). More efficient compression at redder wavelengths is attributed to a greater density of DM actuators in the BBIR frequency space and greater sensitivity of SFG optimization due to crystal phase matching. The BBIR generation and BaF_2 exit window transmission yield pulses with negative dispersion, but GVD curvatures in materials (Fig. 2.2(a)) result in fairly crude corrections of GDD while imparting TOD. While DM compression favors initially positive GDD (column II versus IV), limited material control may restrict the GDD sign when balancing all initial phase terms for optimized mirror deformation. Negatively dispersive materials influence the bluer spectrum least in GVD magnitude and curvature (Fig. 2(a)), resulting in initially short pulses at 900 Torr. However, the DM compressor is unable to correct for the

significant TOD at high (low) BBIR frequencies (actuator density).

Our results demonstrate that the DM compressor is an effective tool for a smooth correction of a pulse with a moderately varying spectral phase. We are able to compress the octave-spanning BBIR pulses to durations of ~4/3 of their transform limits with a compressor throughput, which is dictated by grating efficiency, of over 50%. The efficiency of our compressor could be improved by using a DM with more flexible actuators or a greater density of them to enable the correction of greater magnitude and higher-order dispersion in the BBIR pulses.

2.4 Conclusion

In summary, we have demonstrated the generation and compression of BBIR under different pressure conditions. The results reveal that adaptive compression with a deformable mirror is successful for pulses with varying spectral centers resulting in differing efficiencies and material compensation requirements. We are currently using compressed BBIR probe pulses in transient-IR and other novel ultrafast spectroscopies [4]. Approaching the transform limit afforded by the spectral bandwidth of the BBIR source opens up numerous possibilities for the use of these pulses as pumps and probes in experiments aimed at understanding the electronic and vibrational degrees of freedom in complex systems.

Appendix for Chapter 2

Optical Alignment of BBIR:

BBIR can be aligned from the amplifier by using the fundamental 800nm throughout the whole setup with a much later pick off time from the laser. The later pick off time allows one to use the 800nm path but with much lower intensity hence protecting optics before ramping back the pick off time to give the full intensity. The mode will differ with a different pick off time slightly but the difference is minimal for long distance alignment. The first step would be to remove all the transmission optics (λ/2 half wave plate, β-BBO, calcite timing plate, λ/2 wave plate) needed for the second harmonics and BBIR generation. Placing a beam block before the gas cell, first perform the alignment into the gas cell. The iris needed for this alignment is BB-IR Iris . Using the iris, align the lower intensity 800nm pulse through the iris just before the gas cell (Iris positions in Figure A2.1: IP 1, 2, 3). The telescope should be avoided until there is no other way to correct the alignment. The iris can be used to before and after the telescope but because the telescope is at an angle, float the iris between the curved mirrors to correct the height using the first telescope mirror. Center the beam as well as possible using just the first telescope mirror. The second telescope mirror can be used with the next flat mirror to align the beam as a straight line through the path into the gas cell. Remember not to alter the distance between the telescope mirrors since it affects the collimation. To check the collimation/mode of the beam, inset a flat mirror in the transmission optics line and send the beam through the hole in the box to the adjacent wall. Check the mode of the beam by bringing the timing back to the original intensity. There should be no hot spots or inhomogeneity with the beam profile.

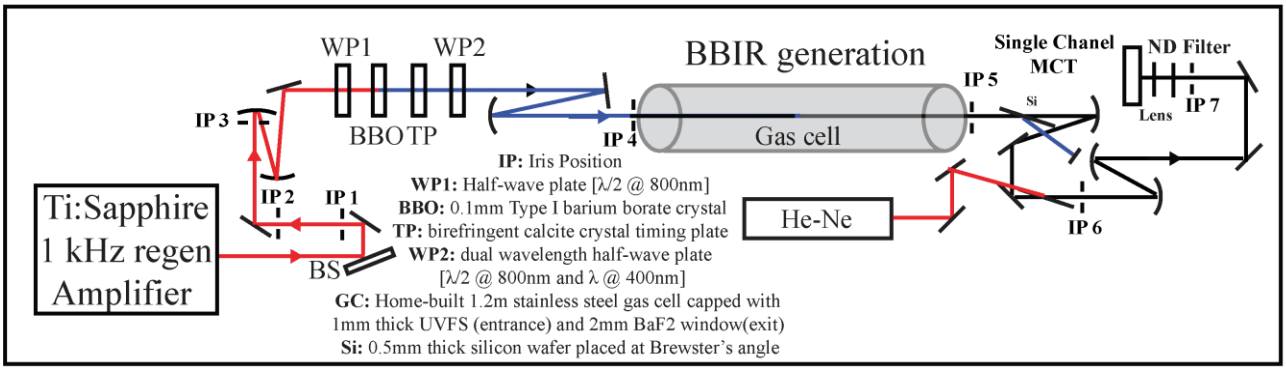

Figure A2.1: BBIR generation by filamentation of 800 nm/400 nm light fields in a pressure-controlled gas cell. WP1: Half-wave plate [λ/2 @ 800nm]; b-BBO: 0.1mm Type I barium borate crystal; TP: birefringent calcite crystal timing plate; WP2: dual waveleng

For the next alignment bring the intensity lower again and using the fundamental 800 nm align it through the gas cell and into the collimating mirror after the gas cell (IR 5: Iris label: Iris Exiting Gas Cell Visible). Remember to remove the silicon so that you can see the path of the 800nm. Follow the 800nm though the next few mirrors at reduced intensity. Stop the 800nm before it hits the single channel detector. Do not let the 800nm go through the pulse shaper since it will damage the deformable mirror. Once you are happy with the propagation of the 800nm pulse, continue on to generate the second harmonic generation by inserting the transmission optics with the back reflection on top of the original beam. It is possible to use a power meter to maximize the 400nm pulse by flipping the dichroic mirror already in the path before the gas cell. There might be need to adjust the post collars for these transmission optics since the height of the beam might have moved with the alignment of the 800nm outlined previously. Adjust the pick off time to optimal and ensure that all the light is being used to generate the BBIR pulse. Ensure that the Si Wafer is placed at a very steep Brewster's angle to allow maximum transmission of the IR pulse but absorption of IR pulse. Make sure all the IR coming out of gas cell is blocked but not blocking the outgoing IR after the collimating mirror onto the gold mirror. Hitting gold coated mirror with the fundamental 800nm and second harmonic 400nm will burn the mirror so

take care to not let the visible beams hit the gold mirror. The next mirror pair allows for the IR to turn around the corner. The second silicon wafer not only allows removal of any residual visible light but also allows for the He-Ne IR overlap. The angle for this wafer is very steep to allow for maximum transmission of IR light as well as the reflection of the He-Ne beam. Avoid adjustment of this wafer because it very hard to align this for maximum transmission and the overlap with He-Ne. Use the mirrors before the silicon wafer to align the He-Ne IR overlap to achieve independent control of the IR without He-Ne beam.

There is no Iris specifically to set the height between the collimation mirror after gas cell and the last gold mirror before the BBIR merges with He-Ne. The He-Ne beam is then used as a guide to align the BBIR through the rest of the laser table. The curved mirror telescope was build to collimate the BBIR beam to 1mm diameter before the pulse shaper. The difference between the mirror are set to (XXX). The distance is determined by using the joule meter (Coherent) to measure the rate of divergence/convergence for the BBIR assuming a Gaussian pulse profile. The BBIR has pulse energy of 100-200 nJ near the telescope. Remember to use a lens to fit the beam in the instrument area for the joule meter. Once the distance is set by adjusting the mechanical stage of the second curved mirror of the telescope set the mirrors so that the He-Ne beam is centered on the curved mirrors. The He-Ne beam and BBIR beam have different collimation rates hence the He-Ne might actually converge compared to the optimal spacing for the curved mirror telescope distance for the BBIR.

To align for the He-Ne and BBIR overlap use the single channel MCT (Mercury Cadmium Telluride) detector for the integrated signal of the BBIR beam. The detector is set before the beam enters the deformable mirror pulse compressor for compression and lens allows

for the beam to be focused on the pixel for detector. The detector needs to be cooled before being used so remember to fill the Dewar of the detector with liquid N_2. For the alignment two irises are used: the iris after the Silicon wafer set in a post permanently (Figure A2.1;IP: 6, Iris Label: Iris BBIR/HeNe after Si approx. 6.5") and the iris after set before the single channel detector (Figure A2.1;IP 7, Entering Pulse shaper Iris grating height). The best alignment is achieved when using both Irises, the near field mirror is used to maximize the detector signal and using combination of the far-field mirrors to achieve maximum IR signal in the detector. Alternate between the near field and the far field so you get independent control of the two different dimensions to get the ideal alignment and overlap between the He-Ne and BBIR. Make sure the alignment of the He-Ne beam is not changed once the He-Ne and IR overlap is optimized.

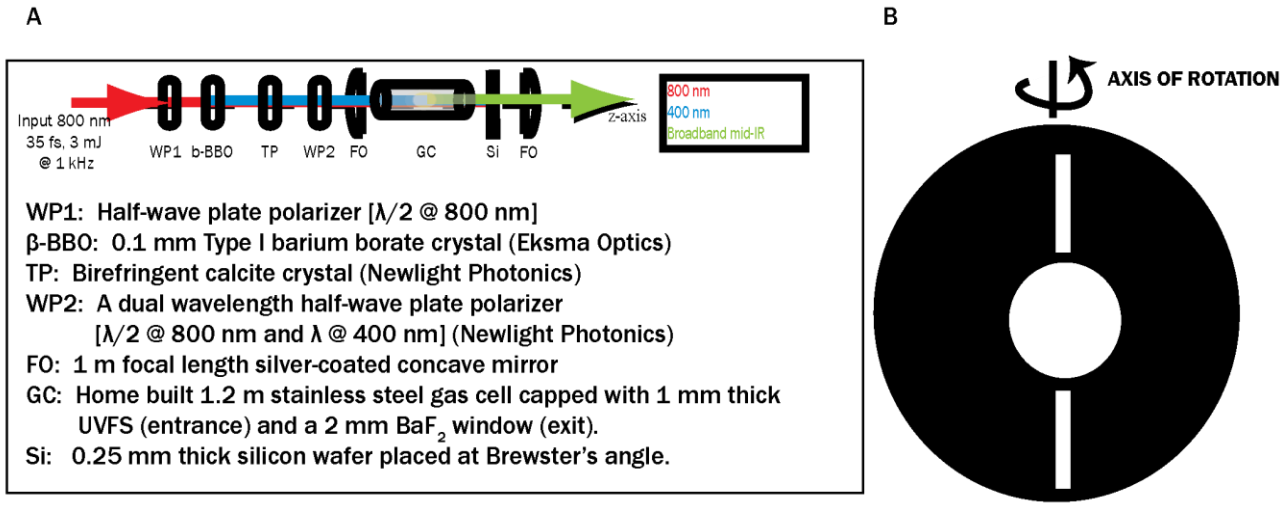

Figure A2.2: (A) BBIR generation by filamentation of 800 nm/400 nm light field. (B) Orientation of mounted BBO crystal for Type I second harmonic generation. The axis of rotation represents the phase matching angle to maximize the second harmonic generation.

To optimize the output of the BBIR a combination of different optics can be changed : the BBO crystal , the Calcite timing plate, Gas cell, Grating compressor in the Regenerative amplifier of the Laser. The BBO crystal has two different angles that can be optimized: one for

the polarization dependency of the mixing of two photons of 800nm and phase matching angle set in the rotation stage. For the type I crystal, crystal must be orientated (the angle of the phase of the crystal) with the incident beam properly aligned and at normal incidence. The crystal should also be tuned with respect to the axis of rotation (in this case the phase matching angle) to optimize the power of the second harmonic generation. Look at the Figure A2.2B for visual details about the angle. The calcite timing plate should be set to optimize the BBIR generated by using the detection from the single channel detector. A combination of the BBO phase matching angle and timing plate assures that the optics is set for the maximum BBIR generation. The grating compressor in the Amplifier can be controlled by the software provided by Newport. You can control the chirp of the 800nm pulse by clicking the right or left clicks of the mouse in the tab (XXX). The combination of chirp settings and BBO crystal angle and timing plate angle allows for the control of the output BBIR generation. Beware that there are local minima in the Grating compressor chirp control that allows for different local maxima for output of the BBIR generation. Don't forget to take large sweeps in the chirp settings and BBO angles to check the maximum output of the BBIR.

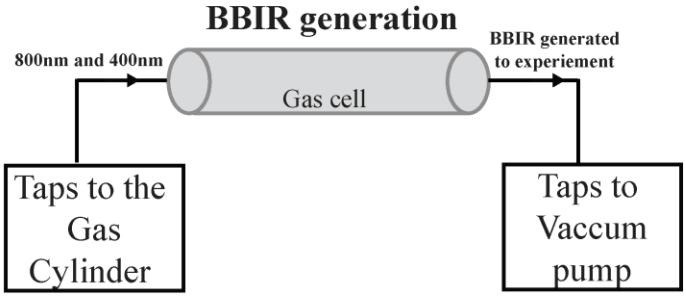

Figure A2.3: The schematic for BBIR generation includint the taps for the vaccum and gas cylinder for filling and vaccuming.

To control the output and the area of focus of the 800nm and 400nm pulses the gas cell can be moved vertically and horizontally to get the all of the BBIR output since the collinear geometry doesn't guarantee that the IR follows the visible outputs. To control where the filamentation process happens, translate the gas cell across the direction of the focusing vector. This is especially useful when there is white light generated because of the high power density of the 800nm and 400nm pulses when they transmit through the BaF_2 window at the end of the gas cell. While translating the gas cell towards the direction of the transmission optics for the generation of the BBIR, the focusing of the beams happens near the front of the gas cell and hence the BaF_2 window doesn't generate the white light. A combination of all these factor lets you achieve good efficiency of the BBIR generation.

Changing the pressure of the Gas cell by using the compressed air cylinder and the vacuum motor allows for spectral tuning. To flush the gas cell start the vacuum motor and open the taps and switches on the side of the vacuum meter. Watch the pressure gauge and make sure the pressure is dropping so that the gas cell is completely empty. This might take a while for the pressure to drop below 5 Torr. Close the taps before turning off the vacuum pump so that you can keep the pressure at 5 Torr or less. To fill the gas cell, turn the regulators on the gas cylinder for positive pressure and open the taps and switches on the other side of the gas cell. This allows for the gas cell to fill with the compressed air or any gas of choice. Adjust the taps so that there is a consistent positive flow of gas by monitoring the pressure gauge. Be careful with the taps because it the gas can fill up very quickly and the pressure may quickly rise. Adjust the taps till you reach desired pressure and close the taps to contain the gas in the cell. Turn off the regulator in the gas cylinder to keep the pressure constant in the gas cell. Flush and fill the gas cell three times before setting up the required gas in the required pressure. The spectral tuning and

different pulse energies are possible for a combination of different pressure and gasses as well as crystal angles and chirp conditions. For reference, look at the table below for various conditions in compressed air. Use the spectral filters with the integrated measurements to tune the spectrum without looking at the spectrum in the array detector. The grating was selected using the grating equation given below:

Pressure of air in gas cell	650 Torr	760 Torr	900 Torr
Spectral Center (ω_0)	2000 cm^{-1}	2300 cm^{-1}	2600 cm^{-1}
Full width at 10% maximum spectral bandwidth ($\Delta\omega$)	1208 cm^{-1}	1121 cm^{-1}	1444 cm^{-1}
Pulse Energy	120 nJ	180 nJ	240 nJ
Transform Limit of BBIR pulse	15 fs	16 fs	16.5 fs

Table A2.1: Conditions of the BBIR output under various pressure of compressed air

Alignment of the pulse shaper:

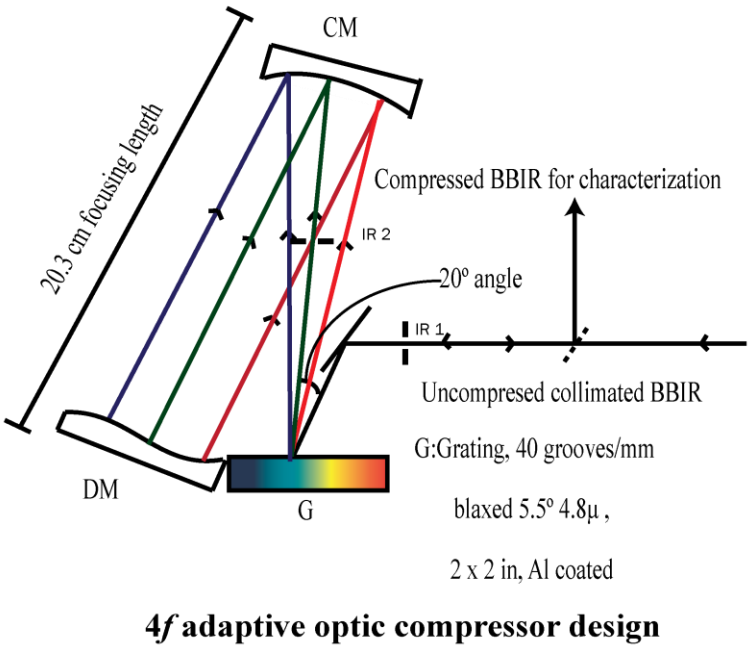

Figure A2.4: Experimental setup for the pulse shaper. IP labels are Iris positions used for the respective iris.

The pulse shaper is built with the 4*f* geometry with *f* being 20.3 cm. The grating was selected using the grating equation given below:

$$\sin\alpha + sin\beta = N \times m \times \lambda$$

Where N is the number of slits per mm; m is the order of diffraction; λ is wavelength; α is the angle between the incident light and normal to grating; β is the angle between the diffracted light and normal to grating. The curved mirror allows the different orders to be focused into the deformable mirror and the refocused on the grating on the second round trip. To set the first mirror at the 20° angle to the grating, set the height of the incoming pulse using the Iris (Iris entering pulse shaper Iris grating height 6.5in) by looking at some far field place. To set the angle for the mirror, draw on the breadboard the 20° going into the grating. The aluminum block is machined so that the height of the grating on top of the grating mount is 6.5". Set the

aluminum block and the grating such that the angle is set correct and the aluminum block is in the far end of the breadboard. The square mirror was chosen such that the outgoing beam from the pulse shaper misses this mirror and hits the other mirror these set at lower height.

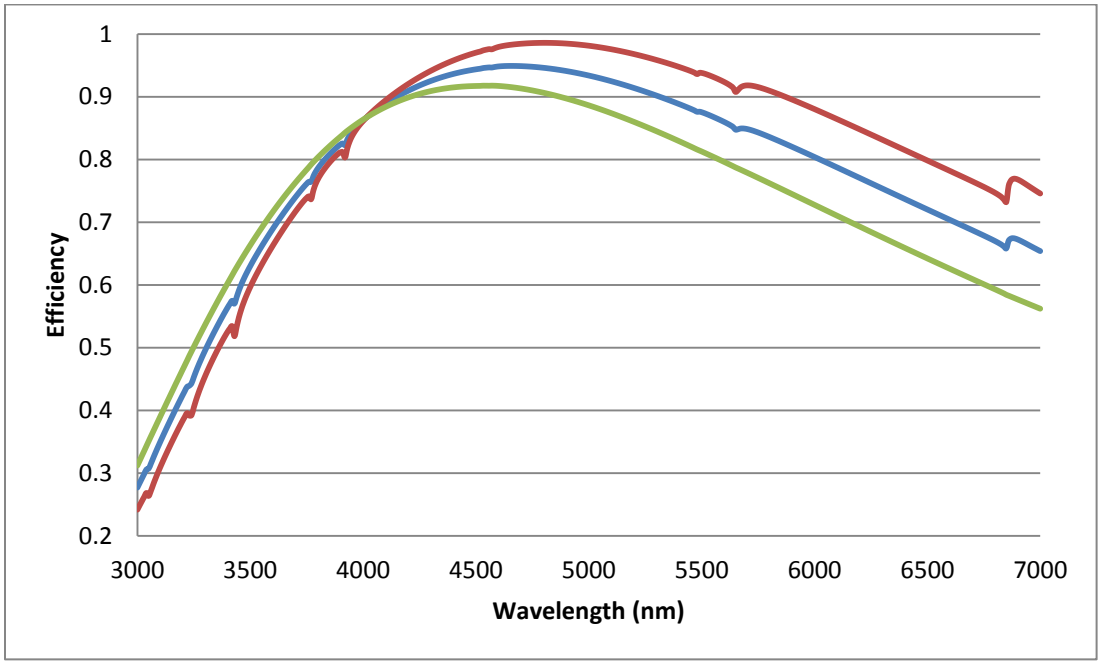

Figure A2.5: Theoretical Efficiency 40gr/mm, 1st order, 5.5° blaze, λ=4.8um, Al. The Blue trace is the average efficiency of the two polarization possibility. The Red trace is the response to S polarized light whereas the Green trace is response to the P polarization light.

Once the block is set, for the first time alignment you can use a use a small portion of the 800 nm fundamental pulse so that the order are seen more visible. The 6th order of the 800 nm pulse should be close to the 4.8μ that is the blazed wavelength of the grating. This should be the brightest order seen as well. The IP position shown in Figure A 2.4 as IR 1 is set to be the centered at the blazed wavelength and the Iris used is Iris entering pulse shaper Iris grating height 6.5in. To center the grating use a far field position beyond the curved mirror to act as a near field. To set the tilt of the grating, use the tilting knob on the grating mount and set the height. To align vertically use the angle in the grating position to make sure the 6th order of the

800nm pulse is center on the correct bolt row. The 800nm beam is only to make sure that the grating the is set well to be centered around 4.8μ but do not let the 800nm pulse go to the deformable mirror. The mirror is gold coated and hence 800nm pulse should not hit the silicon nitride mirror. Set the curved mirror on the translational stages 20.3 cm away from the grating. The translational stage gives you fine alignment ability in both the horizontal and Z axis.

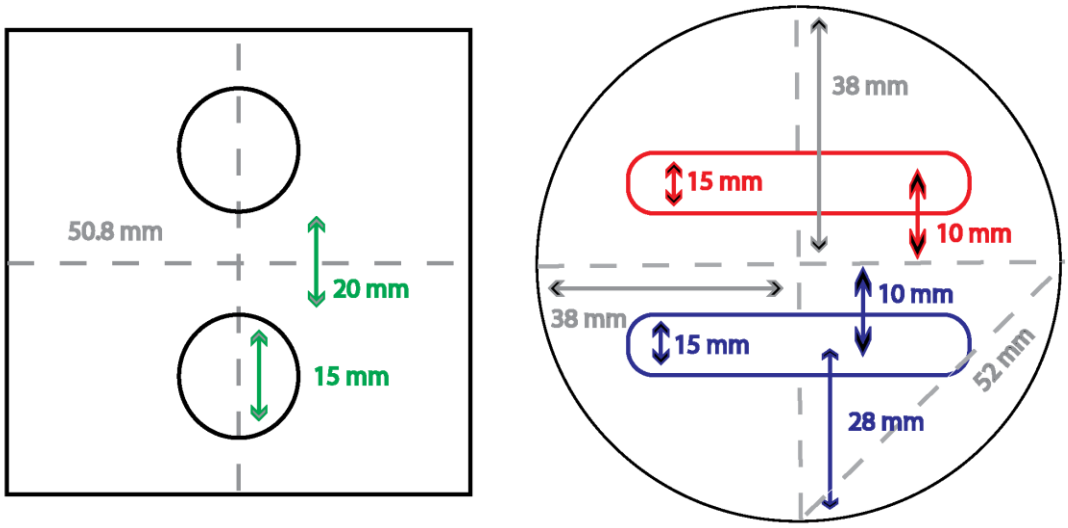

Figure A2.6: Profile of the grating (left) and Curved mirror (right). The top beam profile is the incoming beam profile and bottom beam is the outgoing beam profile. The beam profiles are for the IR but He-Ne beam can also be thought of similarly for visual interpretation.

Now is the time to start using the He-Ne to align the rest of the pulse shaper. Use the Iris at Iris Position 6 (Figure A2.1; Iris label Iris BBIR/He-Ne after Si approx. 6.5") to separate the diffraction gratings of He-Ne. Count the grating orders to give you the 7th He-Ne order and center it on IR position 2 (Figure A2.4; Iris entering pulse shaper Iris grating height 6.5in). The 7th order should be the brightest order since the He-Ne is blazed at 4.8μ. Remember because the He-Ne is a CW laser, there will be negative orders as well. So remember to count the orders well and learn the brightness gradient for the -2 to 2 orders. This will help to align the pulse shaper on

a day to day basis as well as centering the pulse shaper on different orders when you move the BBIR to more red /blue wavelengths. For minor alignments on the curved mirror do not use the tilt knob on gratings, rather use the first gold mirror before the grating. Not tilt the curved mirror so that the focused He-Ne orders falls close the grating on the deformable mirror. The deformable mirror does not have mirror knobs to align the outgoing beam. Set the deformable mirror 20.3 cm away from the curved mirror adjacent to the grating. Align the curved mirror so that the outgoing beams are seen in the profile in Figure A2.6. Remember that the outgoing beam is set at 5.8 in at IR position 2 (IR Label: Leaving pulse shaper 5.85in). On a day to day basis, use only the He-Ne and the Iris for the incoming and outgoing beams. Use the curved mirror and initial mirror to do major alignment. The grating can be rotated so that the center of the pulse shaper is on the different orders. This is also useful to do when you are taking a look at the spectrum at the array detector. Check to see if all the frequency components are placed within the mirror length. For lower pressure of the gas cell with red frequencies, you can rotate the grating to fit all the red components within the deformable mirror. To set the height of the outgoing beam the Iris (IR Label: Leaving pulse shaper 5.85in) at Ir position 2 and IR position 1. The height is bought back to 6.5” using two mirrors before the compressed beam enters the interferometer.

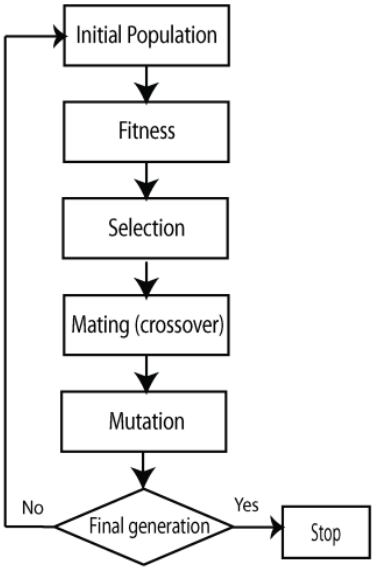

Figure A2.7: Diagram showing the genetic algorithm process for the mirror optimization

The genetic algorithm is written using LabView and the optimization is done using the same software. The Screen shot below tells the common factor entered to get a good optimization from the pulse shaper. Ideal optimization is performed by using the integrated XFROG signal from the photodiode. The GPIB and the base address is from the Locking amplifier. The population size is usually 20 to get a good optimization within 10-15 minutes. To get ideal results, run the genetic algorithm for 50-75 generations. Most of these factors can be kept constant for similar results.

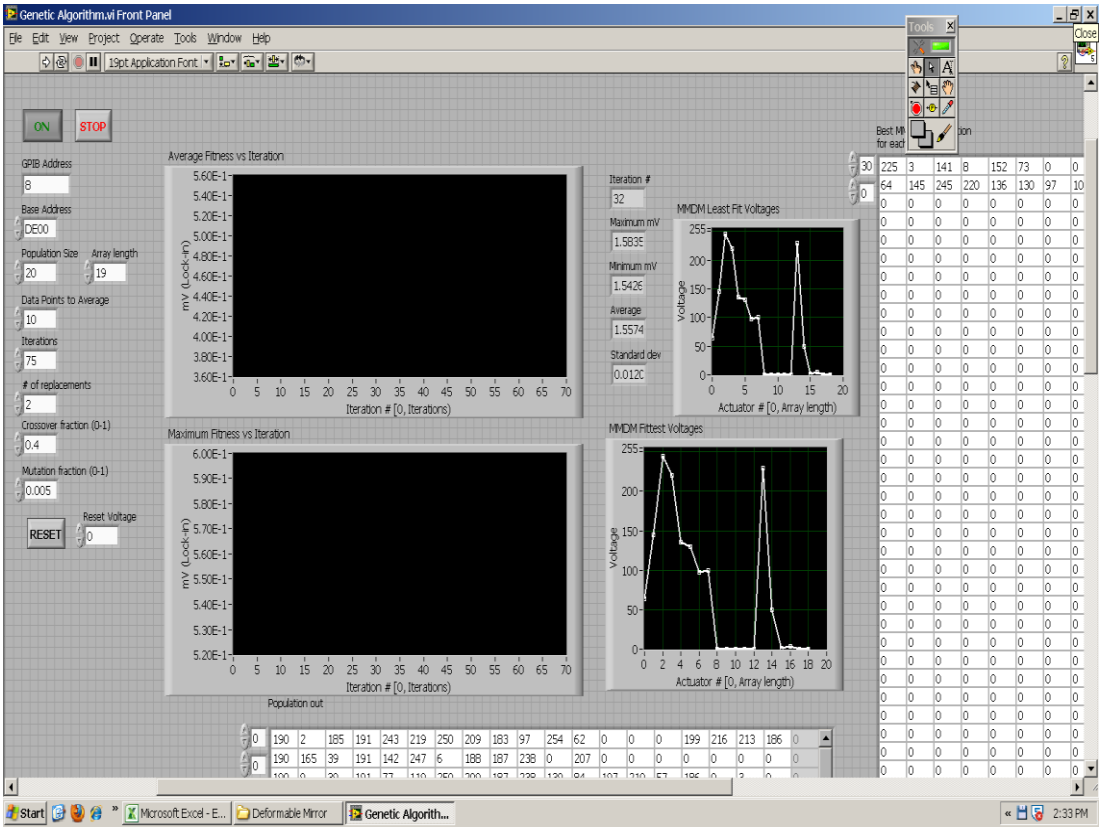

Figure A2.8: Screen shots of the main genetic algorithm window. Press start after the reading is set to start the algorithm.

The following screen shots are some of the other VI‘s to help reset all the actuator voltages to zero or manually enter the voltages to see the effect of the voltages on the mirror shape.

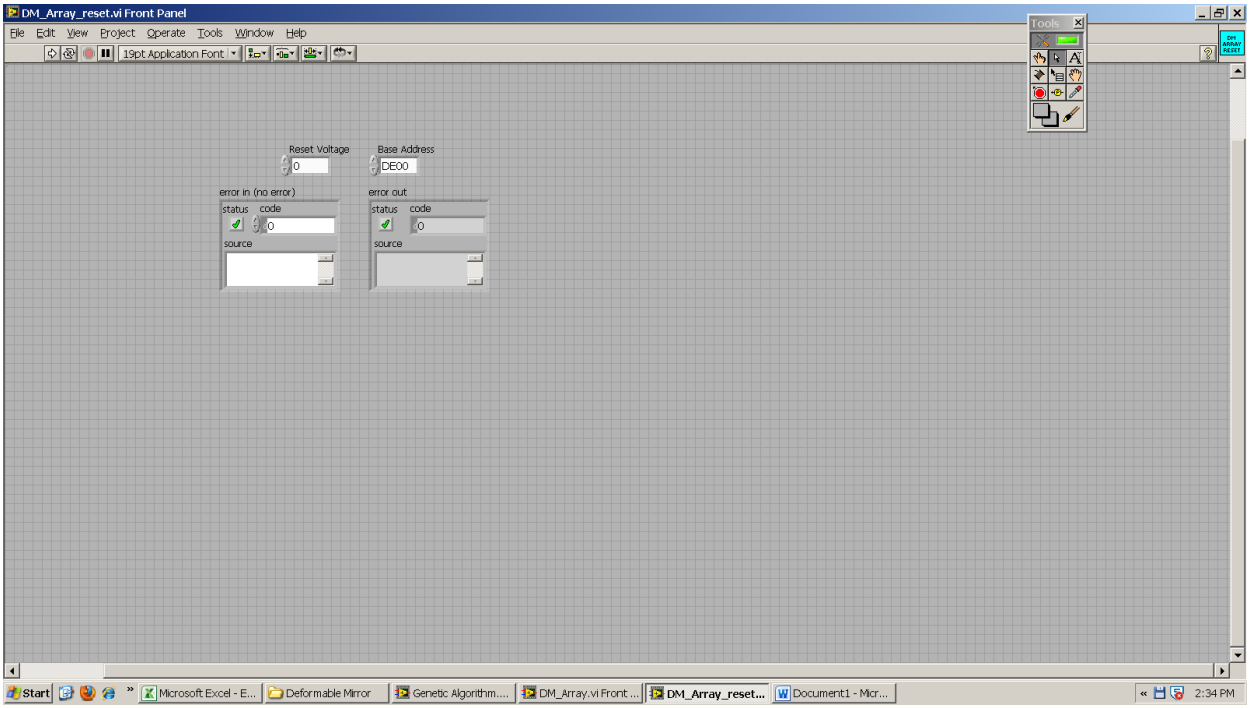

Figure A2.9: Screen shots to reset the voltages to zero.

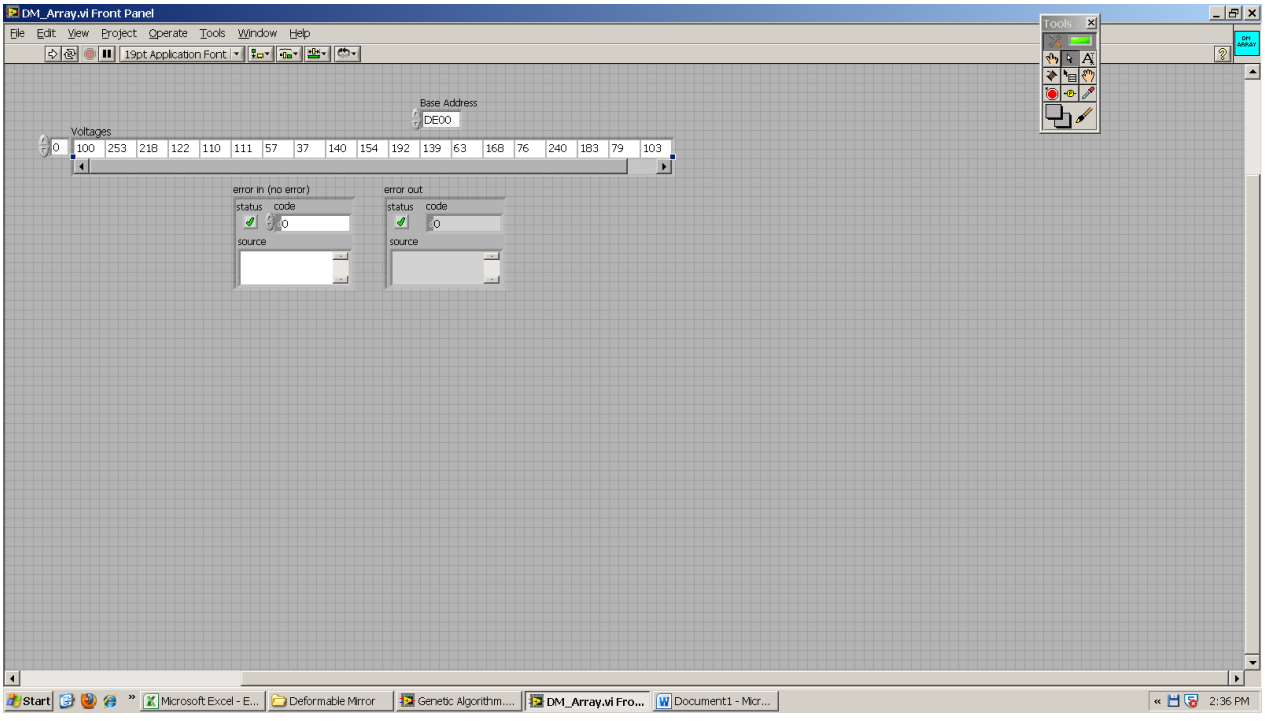

Figure 2.10: Screen shots of the VI to set the voltages manually.

References:

1. M. Cheng, A. Reynolds, H. Widgren, and M. Khalil, "Generation of tunable octave-spanning mid-infrared pulses by filamentation in gas media," Opt Lett **37**, 1787-1789 (2012).
2. C. Iaconis and I. A. Walmsley, "Spectral phase interferometry for direct electric-field reconstruction of ultrashort optical pulses," Opt. Lett. **23**, 792-794 (1998).
3. S. Linden, H. Giessen, and J. Kuhl, "XFROG - A new method for amplitude and phase characterization of weak ultrashort pulses," Phys. Status Solidi B **206**, 119-124 (1998).
4. J. D. Gaynor, T. L. Courtney, M. Balasubramanium, and M. Khalil, "Fourier Transform Two-Dimensional Electronic-Vibrational Spectroscopy using an Octave-Spanning Mid-IR Probe," (in preparation).

Chapter 3: Probing ultrafast vibrational dynamics of intramolecular hydrogen bonds with broadband Infrared pump-probe spectroscopy.

3.1 Summary

Understanding the microscopic interactions governing the vibrational dynamics of inter and intramolecular hydrogen bonds is important for elucidating the structure-function relationships of molecular complexes in biology, chemistry and material science. Of particular interest is learning how the transfer of the proton from a donor to an acceptor is modulated by the motions of the molecule and the surrounding solvent. Intramolecular proton transfer in the excited state has practical applications for developing dye molecules and molecular switches. Our ability to make better dye molecules hinges on understanding the role of vibrational dynamics in intramolecular hydrogen-bonded complexes in the ground and electronic excited states. These include luminescence sensors which allow the excited state proton transfer with the addition of analytes. They can be used as molecular fluorescent probes as a way to label and study DNA-protein interaction [9, 10],. The dynamics of hydrogen bonds in solution is associated with crucial processes that dictate many different chemical and biological reactions. Intramolecular hydrogen bonding plays a special role in important intramolecular interactions and a critical element in selected molecular arrangements. The formation of intramolecular hydrogen bonds has a very pronounced effect on molecular structure and properties.

With the compressed BBIR, we have the advantage of the large bandwidth that can be used to probe the hydrogen bonding dynamics. Utilizing this, we present the results from the study which focus on the vibrational dynamics on the electronic ground state of the two intramolecular H-bonded complexes 10-Hydroxybenzo[h]quinolone (HBQ) and 2-(2′-Hydroxyphenyl)benzothiazole (HBT) which have been used as dye molecules since excited state

proton transfer results in a large Stokes shift [95]. In these molecules, the proton is bonded to the hydroxyl group and is engaged in H-bonding interactions with the N atom as seen from the structure in Figure 3.1. These molecules exhibit broad OH stretches which are structured and reminiscent of the vibrational spectra of the OH stretch of strongly H-bonded systems. The potential of the OH stretch is modulated by low frequency modes which gate the ON distance. This study revealed the high anharmonicity of the model systems as well as time scales that matches with other hydrogen bonding systems. The pump-probe results elucidate the low frequency motions coupled to the fundamental ν_{OH} and the results complement well with the anharmonic theory calculations performed for the systems. The results follow closely with previous studies on these chromophores. The low frequency structural motions represented a 'cogwheel' type motion that allowed the donor and acceptor groups to come closer.

3.2 Experimental Methods:

HBQ and HBT were obtained commercially from TCI and Sigma Aldrich, respectively and used without further purification. Both molecules were dissolved in anhydrous carbon tetrachloride (CCl_4), purchased from Sigma Aldrich, at a concentration of ~300 mM. This concentration results in an optical density of the solution at the OH stretching frequency (ν) of 0.3. The vibrational spectra of the ν_{OH} in the HBQ and HBT samples were obtained using a JASCO FT/IR-4100 spectrometer with 2 cm^{-1} resolution. The solution samples were placed in a commercial sample cell which utilizes CaF_2 windows separated by a 250 μm thick Teflon spacer. The use of CCl_4 as the solvent minimizes spectral interference from the solvent across the vibrational spectrum of the ν_{OH}.

The pump-probe experiments utilized femtosecond mid-infrared (IR) laser pulses produced using a commercial Ti-Sapphire oscillator and regenerative amplifier, which generated 40 fs

pulses centered at 800 nm at a repetition rate of 1 KHz with pulse energies of 4 mJ/pulse. The fundamental 800 nm pulses were split and used as pump, probe or gating pulses (for pulse characterization). The IR pump pulses were generated in a home-built, β-BBO based, double-pass optical parametric amplifier (OPA) followed by difference frequency generation (DFG) in a 500 μm thick $AgGaS_2$ crystal. For HBQ, the IR pump pulse was centered at 2611 cm^{-1} with a bandwidth of 530 cm^{-1} (full width at 10%) as shown by the blue spectrum in Fig 3.1(a). For the HBT sample, the pump pulse was centered at 2888 cm^{-1} to with a bandwidth of 550 cm^{-1} (full width at 10%). The pump pulses were temporally characterized using the cross-correlation frequency resolved optical gating (XFROG) technique [96]. Briefly, the IR pump pulse was mixed with a 800 nm pulse in a 100 μm thick Type I Lithium Niobate (LiNbO3) crystal and the resultant sum frequency generated (SFG) signal was spectrally dispersed with a spectrometer (Thorlabs CCS200) as a function of the time delay between the input pulses. The X-FROG measurement revealed that the IR pump-pulses were ~60 fs in duration. The 800 nm reference field used in the X-FROG measurement was separately characterized by spectral phase interferometry for direct-electric field reconstruction (SPIDER) and used as an input in the X-FROG pulse retrieval algorithm.

The BBIR probe pulse was generated by using the previously described [45] process of filamentation of the fundamental (800nm, 3.5 mJ) and the second harmonic (400 nm) pulses in a pressure controlled gas cell. The BBIR beam is isolated from the 800nm and 400 nm pulses by transmission through a 250-μm thick silicon (Si) wafer at Brewster's angle before being collimated. The BBIR probe pulse was temporally compressed using the *4f* deformable mirror (DM) pulse shaper that has been outlined previously [97]. To help with the temporal compression 2 mm anti-reflection (AR) coated Germanium was added in the BBIR path along

with 1 mm CaF_2 to compensate for the sample cell and other transmissive optical elements in the probe beam path. A Genetic algorithm was used to optimize the pulse compression through a feedback loop that maximizes the detected SFG intensity generated from mixing the 800 nm gating pulse and BBIR pulse in a LiNbO3 crystal. For the HBQ and HBT pump-probe experiments, the pressure in the gas cell was set at 1000 Torr which tuned the probe spectrum to center at 2600 cm^{-1} and spectral width of greater than 1500 cm^{-1} (full width at 10% max) as seen in Figure 3.1 (black traces, right axis). The electric field reconstruction of the BBIR was performed by using the same method (XFROG) as the pump field and resulted in pulse width of ~30fs. Any residual chirp after the experimental correction is handled by using the pump-probe data for the solvent, CCl_4 as the instrumental response. The instrument response over the various gratings was accommodated by fitting with a quadratic function and the experimental data was corrected accordingly. The figures for the correction are shown in the Appendix for chapter 3.

The pump and probe beams with the same polarization were focused non-collinearly into the sample using an off-axis parabolic mirror (f=101.5 mm). The focused pump beam had a spot size of ~150 μm and pulse energy of 400 nJ. The probe pulse was focused to a spot size of <100 um and pulse energy of ~50nJ/pulse. The time delay,τ, between the pump and probe pulses is adjusted with a computer controlled translation stage (Newport, XMS100). The pump pulse is blocked after the sample and the pump-probe signal is dispersed at the focal plane of a 0.19 m spectrometer (Triax 190, Horiba Jobin Yvon, 75 grooves/mm grating) using a 2 × 64 pixel mercury cadmium telluride (MCT) array detector (IR0144, Infrared Systems Development). The signal was collected using band pass filters (either 2.5–5.1 μm or 4.5–8.5 μm) to eliminate the higher diffraction orders from the grating in the spectrometer as a result of the broad bandwidth of the BBIR. A total of 8 grating positions (centered at 2700 nm, 3350 nm, 4000 nm, 4650 nm,

5300 nm and 5950 nm) were used to collect the averaged (~80000 shots) pump-probe signal for both HBQ and HBT. A chopper is placed in the pump arm allowing the collection of the weak pump-probe signal at 500 Hz and discriminating it from the much stronger probe pulse.

Density functional theory (DFT) calculations of HBQ and HBT were conducted in the Gaussian 16 software package[98] using the unrestricted Becke, 3-parameter, Lee-Yang-Parr (uB3LYP) functional and 6-311++G (d,p) basis set. A polarizable continuum model (PCM) was used to account for the solvation of these compounds in CCl_4. Following geometry optimization vibrational frequencies were calculated using Gaussian's default anharmonic frequency calculation settings. An integration grid of 150 radial points and 770 angular points was utilized to ensure accuracy of the optimized equilibrium structures and subsequent anharmonic calculations [99].

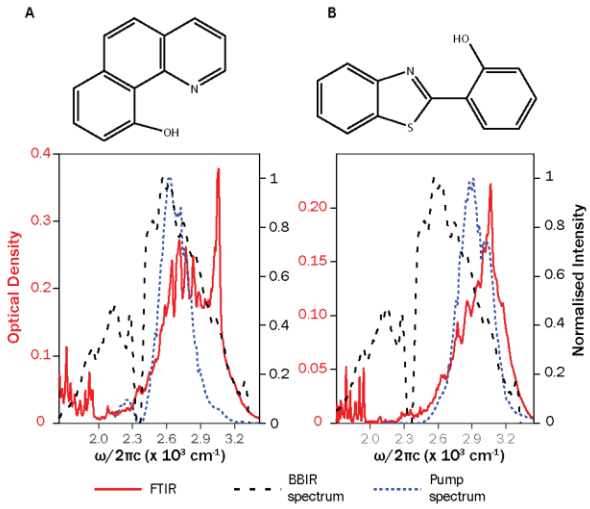

Figure 3.1: Solvent (CCl4) subtracted FTIR of the HBQ (left) and HBT (right) compound showing the area of interest (-OH stretch) is seen in red (left axis, red). The molecular structures of the compounds (HBQ and HBT) are shown above the respective FTIR spectra. The normalized pump and probe spectrum is shown in blue-dotted and black-dashed respectively (right axis, black). The dashed black line is a trace of the broadband mid-IR spectral content of the probe used during the pump-probe experiment. The dotted blue line is a trace of the DFG mid-IR spectral content of the pump used during the pump-probe experiment.

3.3 Results and Discussion:

The FTIR spectra of ~300mM sample of HBQ and HBT (Figure 3.1) indicate the broad line shape of the ν_{OH} spanning 2300 cm^{-1} to 3260 cm^{-1} corresponding to a bandwidth of 960 cm^{-1} (full width at 10% of the max).The ν_{OH} vibration overlaps with the aromatic ν_{CH} that can be observed as the sharp feature at 3061 cm^{-1} for HBQ and 3069 cm^{-1} for HBT respectively. The broad features and multiple peaks seen in the high frequency ν_{OH} stretch can be attributed to complicated underlying dynamics. For HBQ the oscillatory features seen atop the -OH frequency are spaced out at 60 cm^{-1} (between 2600 cm^{-1} and 2900 cm^{-1}) while the HBT has spacing of between 80-100 cm^{-1} (between 2770 cm^{-1} and 2990 cm^{-1}). Hydrogen bonding systems are characterized by the ν_{OH} having large bandwidth as well as structure as seen in HBQ and HBT that is attributed commonly to Frank-Condon like progressions due to anharmonic coupling to low frequency structural modes[100]. The broad nature of the ν_{OH} stretch can pose issues as the fields necessary to probe this mode need to cover the fundamental as well as the overtone for the ν_{OH} stretch. This might encompass over hundreds of wavenumbers and currently the conventional mid IR sources are unable to achieve this. As indicated in the Figure 3.1, the pump mid-IR generated by the DFG does not contain enough spectral content for the entire region of the fundamental ν_{OH} stretch and the overtone as needed to determine the dynamics. However, the BBIR probe used in this study allows us probe the entire fundamental and overtone of the OH region in addition to adjacent spectral information.

The OH peak of the FTIR is centered at 2771 cm^{-1} for the HBQ system and 2930 cm^{-1} for the HBT model system. The blue shift of the OH stretch for the HBT compared to HBQ is representative of the strength of the intramolecular hydrogen bonding. The crystal structure of HBQ found that bond length of the OH is between 1.34-1.36 Å while the structural optimization

in our computational study gave us bond length for the OH stretch as 0.99 Å [101]. While the crystal structure of the HBT has not been published, the structural optimization in our theory calculation gave us OH bond length of 0.989 Å. The red shift in the HBQ compared to HBT is due to the stronger hydrogen bonding OH---N that can be seen by the bond lengths of OH bond.

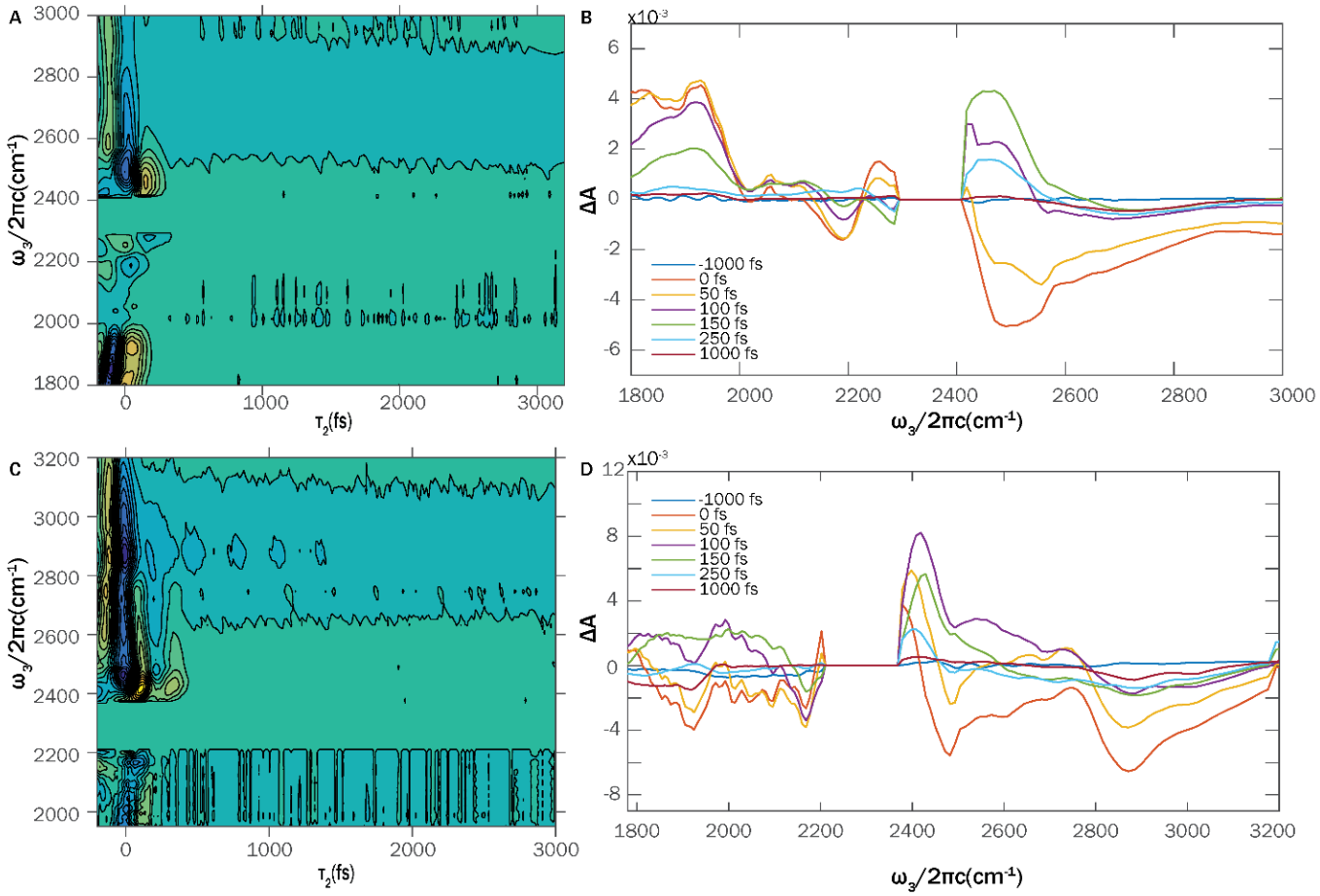

Figure 3.2: Pump-probe spectra of HBQ (top A and B) and HBT (bottom, C and D) in CCl4. A) The pump-probe spectra of HBQ at selected τ points of 0,50, 100,150, 250 and 1000 fs as well as a background pump-probe spectrum at -1000fs. B) The ZZZZ pump-probe spectra of HBT at selected τ points of 50, 100, 200, 500, and 1000 fs as well as a background pump-probe spectrum at -1000fs.

The parallel (ZZZZ) pump-probe spectra of HBQ and HBT in CCl4 solvent as a function of the detection frequency at various time delays are shown in Figure 3.2. The bleach (negative peak)

is centered at the peak of the FTIR transition and represents the ν_0 to ν_1 and the excited state absorption (positive peak) is centered at the transition from the ν_1 to the ν_2 state. To calculate the anharmonicity, the pump probe trace at ~200 fs was fit for a bleach and overtone separately and the difference between the center frequencies is reported. HBQ complex exhibits an anharmonicity of 600 cm^{-1} and anharmonicity of HBT is calculated to be 815 cm^{-1}. FTIR studies on similar phenol–OH(OD)-pyridine systems found that the anharmonicities of the ν(OH—N) vibration is between 180-250cm^{-1} [102]. Another similar study involving dialcohol systems in an apolar solvent showed anharmonicities of hydrogen bonded OH stretch between 160-180 cm^{-1}. Compared to these experiments, HBQ and HBT have large anharmonicity that have been attributed to mixed character of the structural motions rather than pure OH anharmonicities. This kind of mixed character could be a combination of various bend-stretch-shearing motions coupled very strong. This again proves that normal mode representation is a very poor model to understand these systems[103].

Fitting the pump-probe time traces at bleach and excited state absorption frequencies is indicative of the lifetimes of the vibrational dynamics in these model systems. Both HBQ and HBT exhibit an initial very fast time component across all frequencies less than 100 fs. These initial fast dynamics is under the instrument response limit of the experiment and can be attributed to spectral shifts due kerr nonlinearities as well as the non-resonant pure solvent response. The second time component is much longer and can be attributed to the ν_{OH} vibrational relaxation. The bleach frequencies for HBQ systems, between 2700 cm^{-1} to 2900 cm^{-1}, yielded lifetimes between 2.3±0.5 ps to 1.0±0.3 ps. The overtone frequencies, between 2000 cm^{-1} to 2200 cm^{-1}, has a lifetime of between 0.7±0.1 ps to 0.9±0.1 ps. The absorption dynamics has shown slightly faster dynamics to the bleach lifetimes. The fundamental frequencies also show a

decrease in lifetimes across the 200 cm^{-1} range that was measured. This change in timescale across the ν_{OH} could be due to structural heterogeneity[104] . Similarly, HBT exhibits slightly different timescales for the bleach frequencies and absorption frequencies. The timescales for absorption frequencies between 1800 cm^{-1} to 2000 cm^{-1} can be averaged to 1.4 ps due to low signal to noise in this region. The bleach frequencies, between 2950 cm-1 to 3100 cm-1, have time scales in the range from 1.5±0.4 ps to 1.1±0.1 ps. Previous vibrational study for the DBT in toluene has shown longer time scales corresponding to ~3-6 fs timescale [93]. The dampening of the ν_{OH} compared to the ν_{OD} could be due to isotope effects. The longer time scales seen in these systems, are characteristic of hydrogen bonded –OH systems like the di-alcohol systems studied by Lock et al [105] and such as those by the $\nu_{OH/OD}$ mode in D_2O/HOD vibrational relaxation experiments [106, 107]. In addition to the decay rates, the fundamental transition for both model systems has an offset to account for the decay to a non-zero value. Tokmakoff and co-workers have reported this in HOD/D_2O experiments indicating arises from an altered hydrogen bonding network where the ν_{OD} mode relaxes into a "hot" ground state [22, 105, 107, 108].

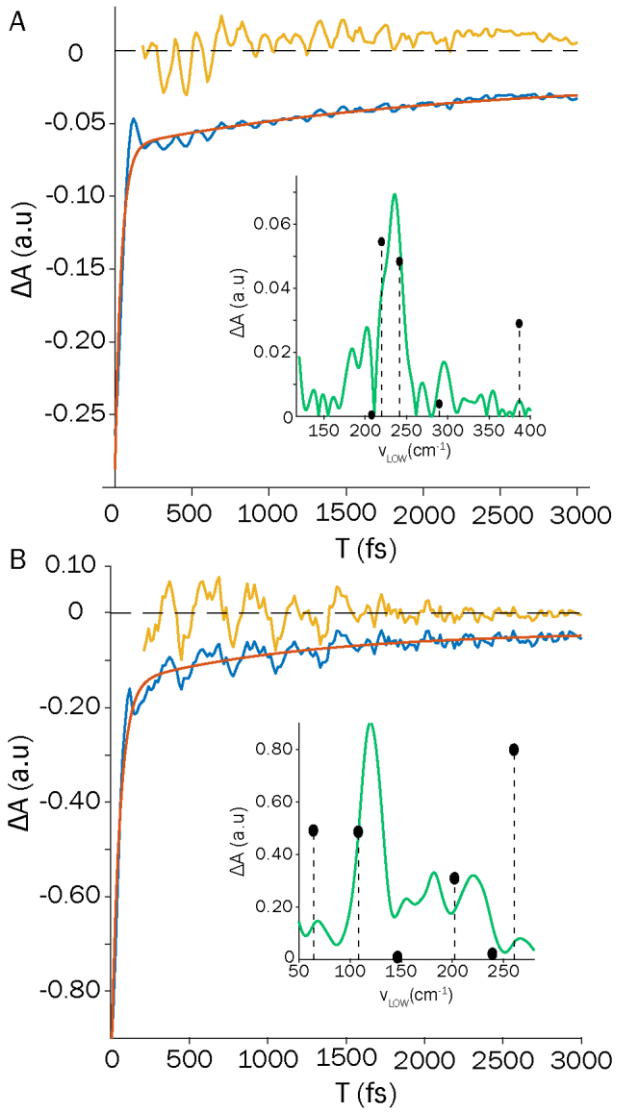

Figure 3.3: Pump-probe time traces and coupled low frequency modes of HBQ (**A**) and HBT (**B**). **A)** The pump-probe time traces at 2771 cm^{-1} as indicated by the blue trace in Figure **3.A.** This trace was chosen as it represents the fundamental region of the pump-probe spectrum. The blue-solid line and red-solid line for the 2771 cm^{-1} frequency trace are the original data and bi-exponential fit, respectively. The residual trace from 180 fs for the bleach is shown as the yellow trace to **3.A**. The inset contains the intensity spectra of the trace along 2771 cm^{-1} calculated from the Fourier transform of the residual shown in yellow. The black-dashed sticks indicate harmonic frequency calculation modes (See Table 1). **B)** The pump-probe time traces at 2900 cm^{-1} as indicated by the blue trace in Figure **3.B.** These trace were chosen as it represents the fundamental region of the pump-probe spectrum for HBT. The blue-solid line and red-solid line for the 2900 cm^{-1} frequency trace are the original data and bi-exponential fit, respectively. The residual trace from 180 fs for the bleach is shown as the yellow trace to **3.B**. The inset contains the intensity spectra of the trace along 2900 cm^{-1} calculated from the Fourier transform of the residual shown in yellow. The black-dashed sticks indicate the modes obtained from the anharmonic frequency calculation (See Table 1).

The time traces fit to a biexponential functions of a characteristic frequency of fundamental mode are shown in Figure 3.3A and 3.3B (blue and red traces). The residuals of the fits, calculated by subtracting the time trace with biexponential decay, in the fundamental region demonstrate a strong coherent oscillatory component for both the model systems (Figure 3.3A and 3.3B, yellow trace). In order to reveal the underlying structural modulations that give rise to the beats, the Fourier transform of the residual was performed as shown in insets for Figures 3.3A and 3.3B. The HBQ residual spectrum shows a strong anharmonically coupled low frequency mode at 248 cm^{-1} as well as at 220 cm^{-1}. The DFT calculations (insets 3.3A stick Figures) agree well with the experimental results especially for the 240 cm^{-1} mode. To eliminate the possibility of the effect of instrument response from the solvent, CCl_4, the Raman modes of the solvent need to be compared with the results. Previous studies have measured the low frequency solvent modes of CCl_4 at 218 cm^{-1}, 315 cm^{-1} (anisotropic), and 464 cm^{-1} (isotropic) [109, 110]. These solvent modes correspond closely to the shoulder at 220 cm^{-1} for the structural modes in HBQ. However the strongest peaks around 242 cm^{-1} are not the results of solvent response and is directly related the structure of the solute HBQ. This mode has been observed in the ESIPT study where the proton transfer was strongly coupled to this structural mode [79].This is in agreement with the displacement vectors calculated by DFT for these vibrational modes (Figure 3.4) as seen with the stick Figures in Figure 3.3.

Similarly time traces for HBT and the biexponential fit for the fundamental frequency at 2900 cm^{-1} (Figure 3.3B, blue and red trace respectively) reveal very strong oscillatory component as seen in the residual trace (Figure 3.3, yellow trace) . The Fourier transform of the residuals (black trace, 3.3B inset) demonstrate a strong coupling with the low frequency vibration at 118 cm^{-1}. Apart from this strong influence, there are low intensity broad features from 150 cm^{-1} to

250 cm^{-1} that are not resolved well enough to pick up particular features. These features could correspond to solute modes or could be from the solvent Raman modes. The strong mode at 118 cm^{-1} matches well to the low frequency motion at 102 cm^{-1} determined by the DFT calculations as seen in the stick Figures. The results deviate significantly from the theory calculations in the absence of the peak at 250 cm^{-1} in the experiment.

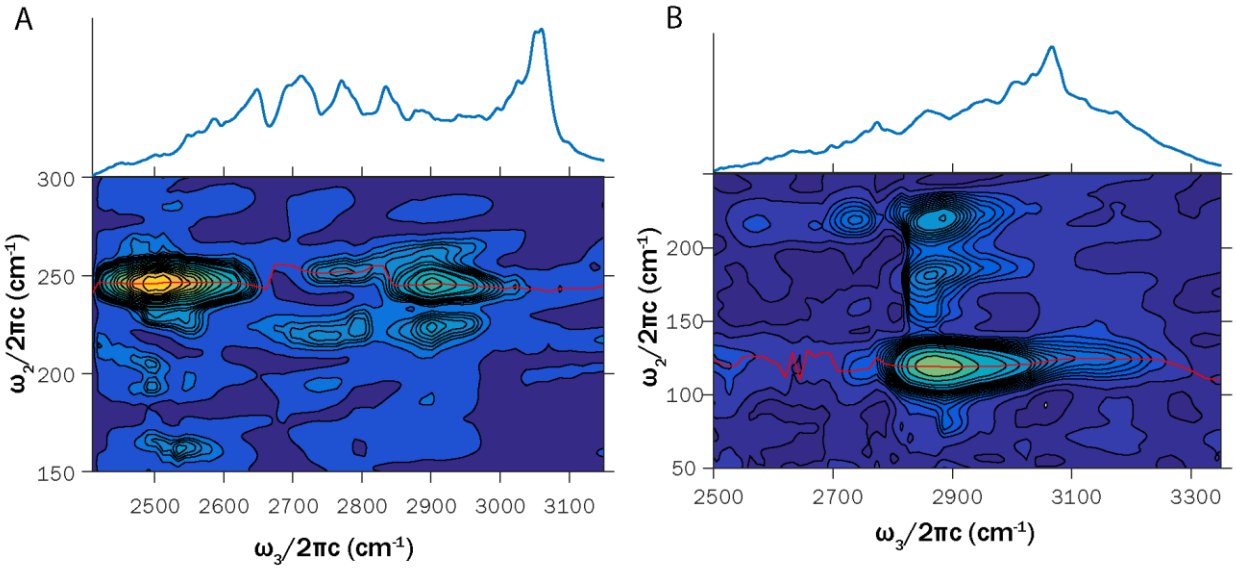

Figure 3.4: **A**) Correlation spectrum of HBQ indicating correlation of many high frequency modes with the low frequency modulation. The top panel indicates the linear spectrum of HBQ over the bleach frequencies. The red linear line indicates the maxima intensity along the ω_3 over distinct characters in the correlation spectrum. **B)** Correlation spectrum of HBT indicating correlation of many high frequency modes with the low frequency modulation. The top panel indicates the linear spectrum of HBT over the bleach frequencies. The red linear line indicates the maxima intensity along the ω_3 over distinct characters in the correlation spectrum

The correlation spectra as a function of the low frequency modulations is shown in Figure 3.4 is the result taking the FT of all residuals for the fundamental and overtone transitions for both HBQ and HBT. The correlation spectrum for HBQ (Figure 3.4A) shows the presence of 245 cm^{-1} over various high frequency modes in the fundamental bleach region and this kind of strong coupling to the fundamental transition suggests anharmonic coupling to the hydrogen bonding

vibrations [23-35]. Transient absorption frequencies are unable to be resolved to get the low frequency modes. The most prominent feature in the correlation is seen as 245cm^{-1} structural mode. For this mode the strongest coupling for the HBQ, is seen the wings fundamental stretch shown in the FTIR, and there is a clear shift in the low frequency mode correlated in the bulk of the fundamental mode. The wings of the FTIR are strongly correlated to the motion at 245 cm^{-1} while the bulk of the fundamental frequency is more weakly correlated with 250 cm^{-1}. The next prominent feature is the mode at 223 cm^{-1} and this could be attributed to two different modes: the molecular mode contributed from the solute or the anistropic Raman mode from the solvent. The rigid geometry of HBQ complex plays a major role in how the structural dynamics affects the ν_{OH} vibrational dynamics.

Mode description	HBQ			HBT		
	ω_j (cm^{-1})	Intensity	Cubic constants	ω_j (cm^{-1})	Intensity	Cubic constants
'Butterfly', Symmetric oop bend	86.89	1.5881	-18.94	64.58	0.9795	102.17
Symmetric oop bend	208.06	0.025	5.12	202.59	0.6151	-17.80
β(-Py) or β(-C3H3NS) Symmetric oop bend	220.02	3.8106	21.68	239.62	0.039	-45.48
'Cogwheel', Symmetric ip bend	241.81	3.3802	59.46	108.47	0.9685	-67.95

Table 3.1: Description of the low frequency modes calculated for HBQ and HBT with the anharmonic correction (ω). (ip= in-plane, oop=out of plane)

For HBT, the correlation spectrum shown in Figure 3.4B show that strongly coupled mode in the bleach with 118 cm^{-1} as well as lesser strongly coupled modes around 180cm^{-1} and 220cm^{-1}. Similar to HBQ correlation map, the transient absorption frequencies do not show contribution from the structural modes. Contrary to the results from HBQ, the mode at 118 cm^{-1} is correlated over the majority of the linear spectrum. There is no shift in the correlation map over the fundamental frequency and this could be because this mode is the main contributor to the ν_{OH} anharmonicity. The modes around 180 cm^{-1} and 220 cm^{-1} modes also show correlation over the

bulk of the fundamental frequency region. Similar to HBQ, the 220 cm^{-1} mode could be representative of the anisotropic Raman mode from the solvent, CCl4 or it could also molecular motion of HBT. Theoretical calculations show a closely associated mode at 240 cm-1 that could be the molecular motion seen. HBT, in contrast to HBQ, has more flexibility in the structure that allows for more out of plane structural motions that affects the vibrational dynamics of HBT compared to that of the HBQ.

The anharmonic frequency calculations for both the systems are able to provide visualization of the different molecular motions that could be strongly associated with ν_{OH}. Tables 1 and 2 highlights the low frequency modes as well as the cubic coupling constants calculated that could be coupled to the ν_{OH} mode and contribute to the correlation spectrum shown (Figure 4.4A and 4.4B). For HBQ, the calculations that show a possible corresponding modulation at 241 cm^{-1} that matched very closely to the experimental results seen in Figure 4.4A. The calculations indicate a 'cogwheel' like symmetric in-plane bend providing the bond between the phenol and amine as the backbone for a breathing motion. This motion deliberately brings the nitrogen and proton from the OH bond closer and indicates that this motion might facilitate to the proton transfer in the excited state. The 241 cm^{-1} mode correlates to a very high cubic coupling of 59.3 cm^{-1} and the 220 cm^{-1} mode which correlates to the strongest intensity has a coupling constant of 21.6 cm^{-1}. These numbers match the intensity of the oscillations seen in the experiment and hence the strength of the correlation of the mode. The calculations also yield a ν_{OH} fundamental frequency of 2716 cm^{-1} which closely matches the fundamental frequency of the FTIR at 2771 cm^{-1}.

Theory calculations for HBT seen in Table 1B and shows the mode at 102 cm^{-1} replicates the cogwheel motion that reduces the O-H distance. Similarly, this motion has a high cubic coupling constant that results in strong correlation as seen in correlation map in Figure 4.4B. This mode

has been observed in many theory calculations as well as the vibrational study on DBT [14, 19-26]. This low frequency mode can also be seen in the peak spacing of 80-100 cm^{-1} as seen in the linear spectrum (Figure 4.1). Other vibrational motions that are notable due to their high intensities and correlations are the modes at 64 cm^{-1} and 260 cm^{-1} but both these modes are absent from the experimental correlation spectrum. Theory might be unable to completely replicate the anharmonicity picture for HBT well.

The line shapes of the OH mode as seen in the FTIR pose a unique problem in understanding the vibrational landscape. In other similar systems exhibiting strong hydrogen bonding, this phenomenon is attributed mainly to anharmonic coupling through low frequency structural modes giving rise to broad lineshapes with complex structure. Following this theory, correlation of the ν_{OH} with the low frequency mode in the HBQ and HBT complex strongly suggests anharmonic coupling through low frequency structural modes gives rise to these broad lineshapes as seen in Figure 3.1. For HBQ system the above observations coincide with the vibrational analysis of the data collected by Chou and co-workers where the vibrational mode between 230 and 250 cm^{-1} has been observed as having a significant impact on the ESIPT. For HBT, the results have shown the presence of strong coupling to a motion that is very similar to the mode in HBQ but red shifted by about 120 cm^{-1}. The reason for this shift could be due to a different structure moiety between the two model systems as well as the presence of a heavier Sulphur atom that is not present in HBQ.

The clear difference in the strength of the oscillation between HBT and HBQ in the fundamental region may be attributed due the difference in the skeletal moiety of the two molecules. HBQ has a fairly planar structure due to the three rings that force the molecule to the plane while HBT has a single bond connecting the rings (between the donor and acceptor) that

allow for more flexibility for the structural modes. The ability to have more flexibility to bring the donor and acceptor molecule in HBT can be the reason behind the increased intensity of the oscillations of the 118 cm^{-1} that is observed. Theoretical studies show that the ESIPT mechanism in HBT is passive due to this flexibility in the skeletal structure while in HBQ, the mechanism takes a semi passive role due to the rigidity [112].

The study shown has a few significant faults that might impact the conclusions drawn. The main issue is that the carbon dioxide absorption which occupies a significant region within the overtone and fundamental region of HBQ/HBT that we are unable to access. This lack of information does limit the conclusions we can make about possible coupling. However, the information we do have does clearly indicate very strong anharmonic coupling to low frequency structural modulations that likely play a major role in the proton transfer mechanism. To help with this, isotope studies using DBQ and DBT where the OD stretch can avoid the carbon dioxide stretch. In addition ultrafast visible-pump IR-probe experiments, similar to the one done on HBT by Nibbering et al. may yield information about the proton transfer and electron transfer [85] .

3.4 Conclusion

Both the systems, HBQ and HBT, have complex structural dynamics that greatly affect the proton transfer in the excited state. The vibrational dynamics of the ν_{OH} revealed that low frequency structural modulations at 245 cm^{-1} for HBQ and 112 cm^{-1} for HBT were anharmonically coupled to the ν_{OH}. These values correspond well with the motions seen from the theoretical calculations. The results clearly indicate very strong anharmonic coupling to low frequency structural modulations that likely play a major role in the proton transfer mechanism of ESIPT reactions.

Appendix for Chapter 3

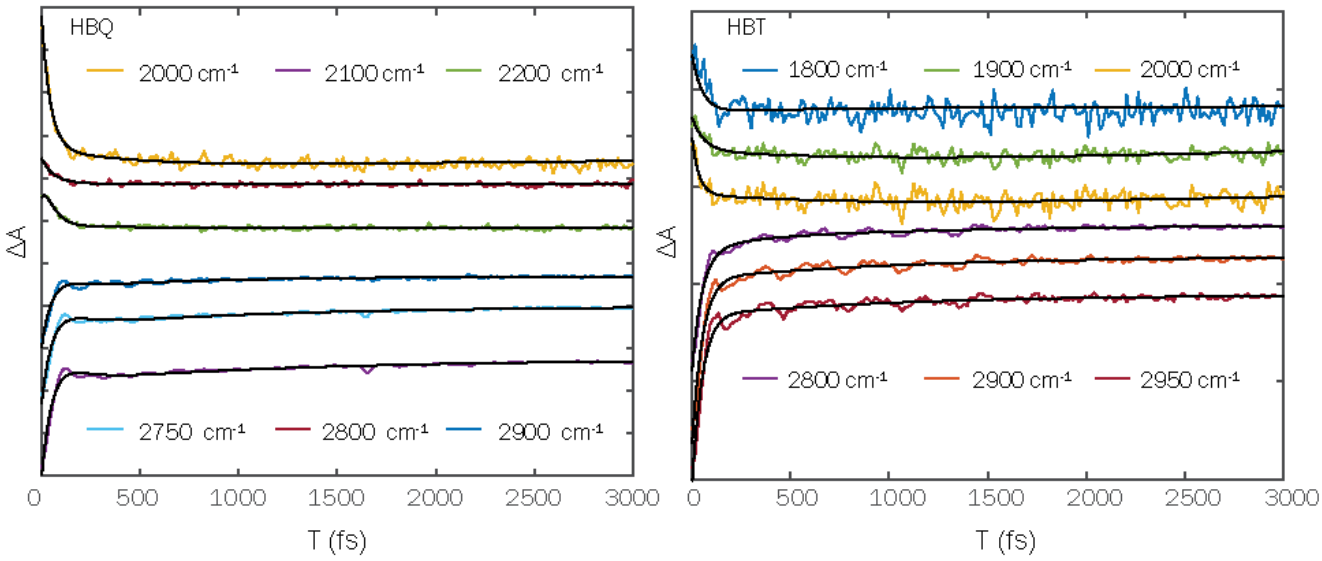

Figure A3.1: Biexponential fits (black) and time traces (colors, legend) for both HBQ and HBT across select frequencies highlighting the fast and slow time component in the bleach and overtone frequencies. The traces are adjusted in intensity so that they stack up in the y-axis.

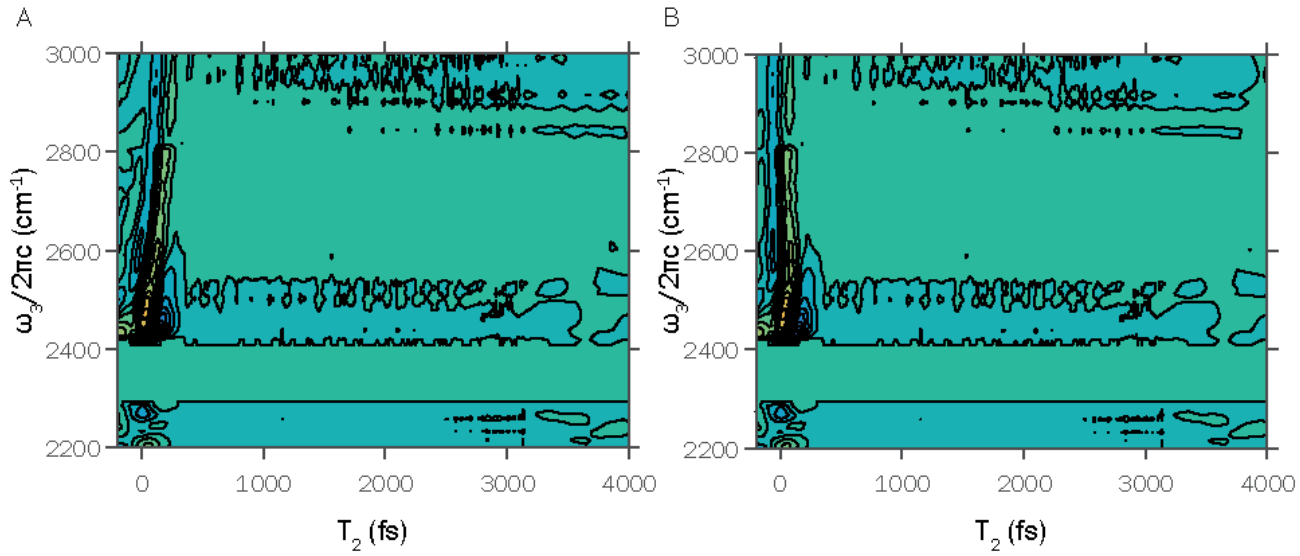

Figure A3.2: Chirp correction for the pump probe data performed with the correction factor from the solvent response across the frequencies for HBQ model systems. (A) Corresponds to the uncorrected HBQ spectrum that clearly shows the tilt across the 2400 cm-1 to 3000 cm-1 frequency range. (B) Corrected pump-probe spectrum for HBQ after the gradient of the tilt from the solvent response is used to correct the HBQ pump probe spectrum.

Mode description	ω_j (cm^{-1})	Intensity	Cubic constants (cm^{-1})
'Butterfly', Symmetric oop bend	86.89	1.5881	-18.94
τ(PhOH)/t(-Py) Structural torsion	116.7	0.2042	-13.46
β(PhOH)/β(-Ph) Symmetric oop bend	208.06	0.025	5.12
β(-Py) Symmetric oop bend	220.02	3.8106	21.68
'Cogwheel', Symmetric ip bend	241.81	3.3802	59.46
β(PhOH)/b(-Py) Asymmetric oop bend	290.07	0.2653	-15.56
H-bond shearing, Asymmetric ip bend	386.9	2.0223	14.29

Mode Description	wavenumber	Intensity	Cubic constants (cm^{-1})
Twist', Symmetric oop bend	18.62	0.0625	-83.67
'Butterfly', Symmetric oop bend	64.58	0.9795	102.17
'Cogwheel', Symmetric ip bend	108.47	0.9685	-67.95
b(PhOH)/b(-C3H3NS) Symmetric oop bend	146.85	0.0144	-
b(Ph)/b(-C3H3NS) Symmetric oop bend	202.59	0.6151	-17.80
b(-C3H3NS) Symmetric oop bend	239.62	0.039	-45.48
H-bond shearing, symmetric ip bend	260.64	1.5951	-73.26
H-bond shearing, Asymmetric ip bend	290.97	5.651	17.99
b(PhOH)/b(-C8H7NS) Asymmetric oop bend	319.73	0.111	-25.34

Table A3.3: Description of the low frequency modes calculated for HBQ and HBT with the anharmonic correction . (ip = in-plane, oop = out-of-plane)

References:

1. J.-J. Zheng, Y.-Q. Lu, P.-L. Li, and C. Tao, "All-optical switching effect of the excited state proton transfer molecule 2-(2'-hydroxyphenyl) benzothiazole in different polar solvents," Wuli Xuebao **59**, 6626-6631 (2010).
2. J. Ma, J. Zhao, P. Yang, D. Huang, C. Zhang, and Q. Li, "New excited state intramolecular proton transfer (ESIPT) dyes based on naphthalimide and observation of long-lived triplet excited states," Chem Commun (Camb) **48**, 9720-9722 (2012).
3. N. Kungwan, F. Plasser, A. J. Aquino, M. Barbatti, P. Wolschann, and H. Lischka, "The effect of hydrogen bonding on the excited-state proton transfer in 2-(2'-hydroxyphenyl)benzothiazole: a TDDFT molecular dynamics study," Physical chemistry chemical physics : PCCP **14**, 9016-9025 (2012).
4. S. Linden, H. Giessen, and J. Kuhl, "XFROG - A new method for amplitude and phase characterization of weak ultrashort pulses," Phys. Status Solidi B **206**, 119-124 (1998).
5. M. Cheng, A. Reynolds, H. Widgren, and M. Khalil, "Generation of tunable octave-spanning mid-infrared pulses by filamentation in gas media," Opt. Lett. **37**, 1787-1789 (2012).
6. M. Balasubramanian, T. L. Courtney, J. D. Gaynor, and M. Khalil, "Compression of tunable broadband mid-IR pulses with a deformable mirror pulse shaper," J. Opt. Soc. Am. B **33**, 2033-2037 (2016).
7. M. J. Frisch, G. W. Trucks, H. B. Schlegel, G. E. Scuseria, M. A. Robb, J. R. Cheeseman, G. Scalmani, V. Barone, G. A. Petersson, H. Nakatsuji, X. Li, M. Caricato, A. V. Marenich, J. Bloino, B. G. Janesko, R. Gomperts, B. Mennucci, H. P. Hratchian, J. V. Ortiz, A. F. Izmaylov, J. L. Sonnenberg, Williams, F. Ding, F. Lipparini, F. Egidi, J. Goings, B. Peng, A. Petrone, T. Henderson, D. Ranasinghe, V. G. Zakrzewski, J. Gao, N. Rega, G. Zheng, W. Liang, M. Hada, M. Ehara, K. Toyota, R. Fukuda, J. Hasegawa, M. Ishida, T. Nakajima, Y. Honda, O. Kitao, H. Nakai, T. Vreven, K. Throssell, J. A. Montgomery Jr., J. E. Peralta, F. Ogliaro, M. J. Bearpark, J. J. Heyd, E. N. Brothers, K. N. Kudin, V. N. Staroverov, T. A. Keith, R. Kobayashi, J. Normand, K. Raghavachari, A. P. Rendell, J. C. Burant, S. S. Iyengar, J. Tomasi, M. Cossi, J. M. Millam, M. Klene, C. Adamo, R. Cammi, J. W. Ochterski, R. L. Martin, K. Morokuma, O. Farkas, J. B. Foresman, and D. J. Fox, Gaussian 16, Wallingford, CT, 2016.
8. V. Barone, "Vibrational zero-point energies and thermodynamic functions beyond the harmonic approximation," J Chem Phys **120**, 3059-3065 (2004).
9. Y. Marechal and A. Witkowski, "Infrared Spectra of H-Bonded Systems," The Journal of Chemical Physics **48**, 3697-3705 (1968).
10. M. Kubicki, T. Borowiak, and W. Z. Antkowiak, "10-Hydroxybenzo[h]quinoline," Acta Crystallographica Section C **51**, 1173-1175 (1995).
11. M. Rospenk and T. Zeegers-Huyskens, "FT-IR (7500−1800 cm-1) Study of Hydrogen-Bond Complexes between Phenols−OH(OD) and Pyridine. Evidence of Proton Transfer in the Second Vibrational Excited State," The Journal of Physical Chemistry A **101**, 8428-8434 (1997).
12. K. Ramasesha, L. De Marco, A. Mandal, and A. Tokmakoff, "Water vibrations have strongly mixed intra- and intermolecular character," Nature chemistry **5**, 935-940 (2013).
13. S. T. van der Post, C. S. Hsieh, M. Okuno, Y. Nagata, H. J. Bakker, M. Bonn, and J. Hunger, "Strong frequency dependence of vibrational relaxation in bulk and surface water reveals sub-picosecond structural heterogeneity," Nature communications **6**, 8384 (2015).
14. D. Madsen, J. Stenger, J. Dreyer, E. T. J. Nibbering, P. Hamm, and T. Elsaesser, "Coherent vibrational ground-state dynamics of an intramolecular hydrogen bond," Chemical Physics Letters **341**, 56-62 (2001).
15. A. J. Lock and H. J. Bakker, "Temperature dependence of vibrational relaxation in liquid H2O," The Journal of Chemical Physics **117**, 1708-1713 (2002).

16. H.-K. Nienhuys, S. Woutersen, R. A. van Santen, and H. J. Bakker, "Mechanism for vibrational relaxation in water investigated by femtosecond infrared spectroscopy," The Journal of Chemical Physics **111**, 1494-1500 (1999).
17. R. A. Nicodemus, S. A. Corcelli, J. L. Skinner, and A. Tokmakoff, "Collective Hydrogen Bond Reorganization in Water Studied with Temperature-Dependent Ultrafast Infrared Spectroscopy," The Journal of Physical Chemistry B **115**, 5604-5616 (2011).
18. M. Rini, A. Kummrow, J. Dreyer, E. T. J. Nibbering, and T. Elsaesser, "Femtosecond mid-infrared spectroscopy of condensed phase hydrogen-bonded systems as a probe of structural dynamics," Faraday Discuss. **122**, 27-40 (2002).
19. C. J. Fecko, J. D. Eaves, J. J. Loparo, A. Tokmakoff, and P. L. Geissler, "Ultrafast hydrogen-bond dynamics in the infrared spectroscopy of water," Science **301**, 1698-1702 (2003).
20. P. B. Petersen, S. T. Roberts, K. Ramasesha, D. G. Nocera, and A. Tokmakoff, "Ultrafast N-H vibrational dynamics of cyclic doubly hydrogen-bonded homo- and heterodimers," The journal of physical chemistry. B **112**, 13167-13171 (2008).
21. M. Khalil, O. Golonzka, N. Demirdöven, C. J. Fecko, and A. Tokmakoff, "Polarization-selective femtosecond Raman spectroscopy of isotropic and anisotropic vibrational dynamics in liquids," Chemical Physics Letters **321**, 231-237 (2000).
22. P.-T. Chou, Y.-C. Chen, W.-S. Yu, Y.-H. Chou, C.-Y. Wei, and Y.-M. Cheng, "Excited-State Intramolecular Proton Transfer in 10-Hydroxybenzo[h]quinoline," The Journal of Physical Chemistry A **105**, 1731-1740 (2001).
23. S. T. Roberts, K. Ramasesha, P. B. Petersen, A. Mandal, and A. Tokmakoff, "Proton transfer in concentrated aqueous hydroxide visualized using ultrafast infrared spectroscopy," The journal of physical chemistry. A **115**, 3957-3972 (2011).
24. C. Schriever, K. Stock, A. J. A. Aquino, D. Tunega, S. Lochbrunner, E. Riedle, R. de Vivie-Riedle, and H. Lischka, "The interplay of skeletal deformations and ultrafast excited-state intramolecular proton transfer: Experimental and theoretical investigation of 10-hydroxybenzo[h]quinoline," Chem. Phys. **347**, 446-461 (2008).
25. A. J. A. Aquino, F. Plasser, M. Barbatti, and H. Lischka, "Ultrafast excited-state proton transfer processes: energy surfaces and on-the-fly dynamics simulations," Croat. Chem. Acta **82**, 105-114 (2009).
26. O. F. Mohammed, S. Luber, V. S. Batista, and E. T. J. Nibbering, "Ultrafast Branching of Reaction Pathways in 2-(2′-Hydroxyphenyl)benzothiazole in Polar Acetonitrile Solution," The Journal of Physical Chemistry A **115**, 7550-7558 (2011).

Chapter 4: Femtosecond Infrared Pump-probe studies on DBQ

4.1 Summary

Direct geometric information can be obtained from mid-IR pump–mid-IR probe experiments on vibrational bands that exhibit features of anharmonic coupling between vibrational modes [1, 2]. Following our detailed experiments with HBQ and HBT, we were interested in studying the effect of isotopes on the oscillatory change of OD stretching mode. Similar studies have been performed on phthalic acid monomethylester (PMME) and modulation on the IR pump probe signal with a period of 330 fs has been observed, indicating a coherent motion of the hydrogen bond. The coherent motions have been ascribed to anharmonic coupling between the O–D stretching mode ν_{OD} and a low-frequency out-of-plane motion of the two sub-groups that are connected to each other through the hydrogen bond [3-5]. In addition, mid IR pump-probe studies on the deuterated version of HBT, hydroxy-deuterated 2-(2′-hydroxyphenyl)benzothiazole in toluene has shown the presence of a wave packet with a frequency of 118 cm^{-1} mode modulating the length of the hydrogen bond [1, 6]. In this chapter we present preliminary evidence for coherent vibrational motions of low frequency in the of the high-frequency O–D stretching mode of an intramolecular hydrogen bond. The vibrational dynamics of the OD stretching vibration (ν_{OD}) of this system was studied using dispersed infrared pump-probe spectroscopy. This study revealed that low frequency structural 230 cm^{-1} for DBQ was anharmonically coupled to the ν_{OD} mode.

4.2 Experimental Method:

HBQ is commercially available from TCI. DBQ was obtained by repeated deuteron/hydron exchange to >90% enrichment in $CDCl_3$ solvent. The isotope substitution was done under nitrogen in a plastic glove bag (Atmos glove bag, Signa Aldrich) to get isolated and controlled environment. DBQ were prepared in CCl_4 at a concentration of ~0.3 M to give FTIR Optical

density of 0.38. The use of CCl_4 is to halt the intermolecular hydrogen bonding between the solute and isolate the intramolecular hydrogen bond. The vibrational spectra of the υ_{OH} in the HBQ and HBT samples were obtained using a JASCO FT/IR-4100 spectrometer with 2 cm^{-1} resolution. The solution samples were placed in a commercial sample cell which utilizes CaF_2 windows separated by a 250 μm thick Teflon spacer. The use of CCl_4 as the solvent minimizes spectral interference from the solvent across the vibrational spectrum of the ν_{OH}.

The optical details of this experiment are very similar to the experimental details outlined in chapter 3 for the pump-probe experiments on HBQ/HBT. The infrared pump-field was generated by difference frequency generation by an in-house built optical parametric amplifier. The mid IR pump pulses were centered at 2050 cm^{-1} for DBQ as shown by the blue spectrum in Figure 4.1. The pump-field was temporally characterized as discussed in Chapter 2 Section 2 resulting pulse widths at half max of ~60 fs.

The mid-IR probe-field was generated by using the broadband IR (BBIR) technique described in chapter 2 and chapter 3 [7, 8]. For the DBQ pump-probe experiments, the pressure in the gas cell was set at 600 Torr which achieved a spectral width greater than 900 cm^{-1} centered at 2100 cm^{-1} as shown by the black spectrum in Figure 4.2. The BBIR was temporally characterized by the XFROG method detailed in chapter 2 [9]. The pump pulse was sent through a variable delay stage, focused into the sample cell in pump probe geometry (spot size 100 μm) and spatially overlapped with the probe pulses. After interacting with the sample the probe pulses were spectrally dispersed and broad-band detected using a 32-channel HgCdTe detector to collect pump robe spectra. This cross-correlation yielded a pulse width of 40 fs for the BBIR. A total of 5 grating positions (centered at 3350 nm, 4000 nm, 4650 nm, 5300 nm and 5950 nm) were used to collect the averaged (~80000 shots) pump-probe signal for DBQ dissolved in CCl_4. A chopper

is placed in the pump arm allowing the collection of the weak pump-probe signal at 500 Hz and discriminating it from the much stronger probe pulse.

Density functional theory (DFT) calculations of DBQ and HBT were conducted in the Gaussian 16 software package [10] using the unrestricted Becke , 3-parameter, Lee-Yang-Parr (uB3LYP) functional and 6-311++G (d,p) basis set. A polarizable continuum model (PCM) was used to account for the solvation of these compounds in CCl_4. Following geometry optimization vibrational frequencies were calculated using Gaussian's default anharmonic frequency calculation settings. An integration grid of 150 radial points and 770 angular points was utilized to ensure accuracy of the optimized equilibrium structures and subsequent anharmonic calculations [11].

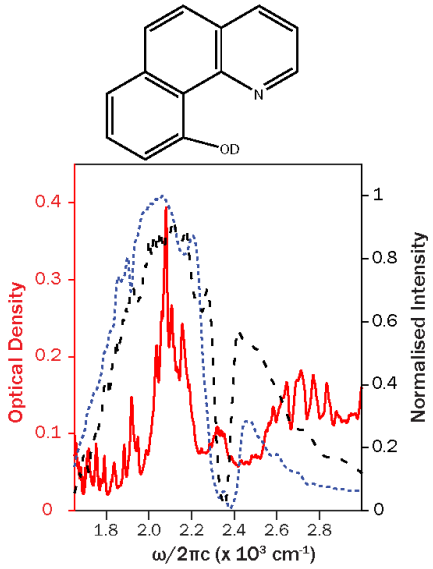

Figure 4.1: Solvent (CCl_4) subtracted FTIR of the DBQ (left) compound showing the area of interest (-OH stretch) is seen in red (left axis, red). The molecular structures of DBQ are shown above the FTIR spectra. The normalized pump and probe spectrum is shown in blue-dotted and black-dashed respectively (right axis, black). The dashed black line is a trace of the broadband mid-IR spectral content of the probe used during the pump-probe experiment. The dotted blue line is a trace of the DFG output mid-IR spectral content of the pump used during the pump-probe experiment.

4.3 Results and Discussion:

Figure 4.1 shows the strongly broadened O–D stretching band of DBQ (solid line) which gives direct indication of an intramolecular hydrogen bond of medium strength. The red shift in the OD stretch compared to the OH stretch seen in HBQ is consistent with decrease in oscillator strength due to the substitution to the heavier isotope. The advantage of using the deuterated version is that the OD stretch is shifted to the red of the very strong asymmetric stretching mode of atmospheric CO_2. Hence pump probe signal will not overlap with the CO_2 absorption and we can access portions of bleach and overtones region that was not possible using HBQ. The line-shape in this region has significant structure which makes it difficult to decipher the underlying dynamics which give rise to broad features and multiple peaks. The pump-probe measurements provide a window to view the dynamics in more detail.

The parallel (ZZZZ) pump-probe spectra as a function of the detection frequency at various time delays are shown in Figure 4.2. In the figure, the absorbance change $\Delta A = -\log(T/T_0)$ is plotted as a function of the spectral position within the probe spectrum for delay times of 0 ,50 ,100, 150, 250 and 1000 fs (T_0, T: sample transmission before and after excitation).The bleach (negative peak) is centered at the peak of the FTIR transition and the excited state absorption (positive peak) is centered at the transition from the $\nu_{OD}=1$ to the $\nu_{OD}=2$ state. To calculate the anharmonicity, the pump probe trace at ~200 fs was fit for a bleach and overtone separately and the difference between the center frequencies is reported. The DBQ complex exhibits a single broad OD mode which gives rise to an anharmonicity of 250 cm^{-1}. FTIR studies on similar phenol–OH (OD)-pyridine systems found that the anharmonicities of the ν(OH—N) vibration is

between 180-250cm^{-1} [12]. Another similar study involving dialcohol systems in an apolar solvent showed anharmonicities of hydrogen bonded OH stretch between 160-180 cm^{-1}[13, 14].

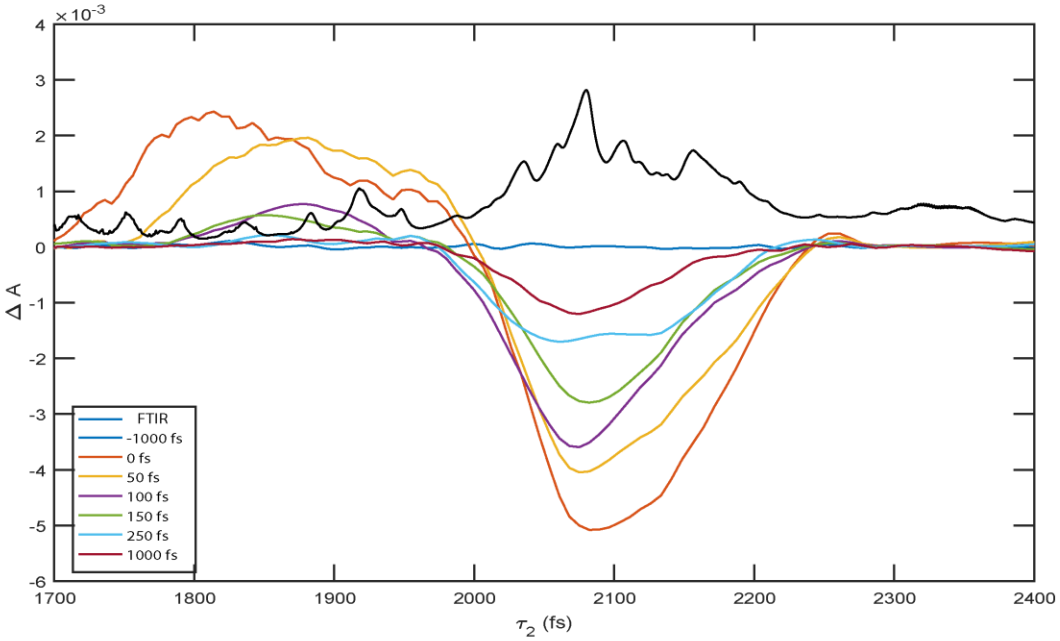

Figure 4.2: Isotropic pump-probe spectra of DBQ. **A)** The ZZZZ pump-probe spectra of DBQ at selected τ_2 points of -1000, 0, 50, 100, 150, 250, and 1000 fs along with the overlapped OD stretch of the stationary spectrum. The plot represents absorbance change $\Delta A = -\log(T/T_0)$ as a function of probe frequency for respective delay times (T_0,T: sample transmission before and after excitation).

The isotropic pump-probe trace for DBQ at the fundamental, 2070 cm^{-1}, was fit with a two exponentials. The fast time scale under 100 fs is attributed to pure solvent response and is unable to be resolved due to it being under the instrument response. The overtone at 1753 cm^{-1} exhibited somewhat faster dynamics with an initial decay of 98 fs and longer decay of 1.1 ps. These fits were typical results for their respective spectral region. These two component decay rates are typical of strong hydrogen bonding systems such as those by the $\nu_{OH/OD}$ mode in D_2O/HOD vibrational relaxation experiments as previously described above in Section 3 [15-20].

The residuals of the fits which were calculated by subtracting the time trace with biexponential decay is able to indicate the presence of anharmonic coupling. Additionally the residuals of the fits in the fundamental region demonstrate a strong oscillatory component (Figure 4.3). These oscillations are superimposed on the signal and these oscillations persist for several picoseconds. Inset in the Figure 4.3 show the spectrum from the Fourier transform of this residual. The Fourier transform residual spectrum indicated the oscillations were centered on 230 cm^{-1} with a spectral bandwidth of 30 cm^{-1}. The Fourier transform spectrum also indicate coupling to additional low frequency mode at 212 cm^{-1}. However we were unable to resolve this peak from the 230cm^{-1} peak. While theory calculations does suggests strong coupling to a mode at 222 cm^{-1}, it is difficult to discern this from the 218 cm^{-1} mode of CCl_4. Previous studies have measured the low frequency solvent modes of CCl_4 at 218, 315, and 464 cm^{-1} indicating the low frequency mode at 230 cm^{-1} is not a result of the solvent[21, 22]. The oscillation frequencies are essentially identical in the protonated compound, from chapter 3. This mode is in agreement with the structural modes calculated by DFT as seen in the stick figures in the Inset in Figure 4.3.

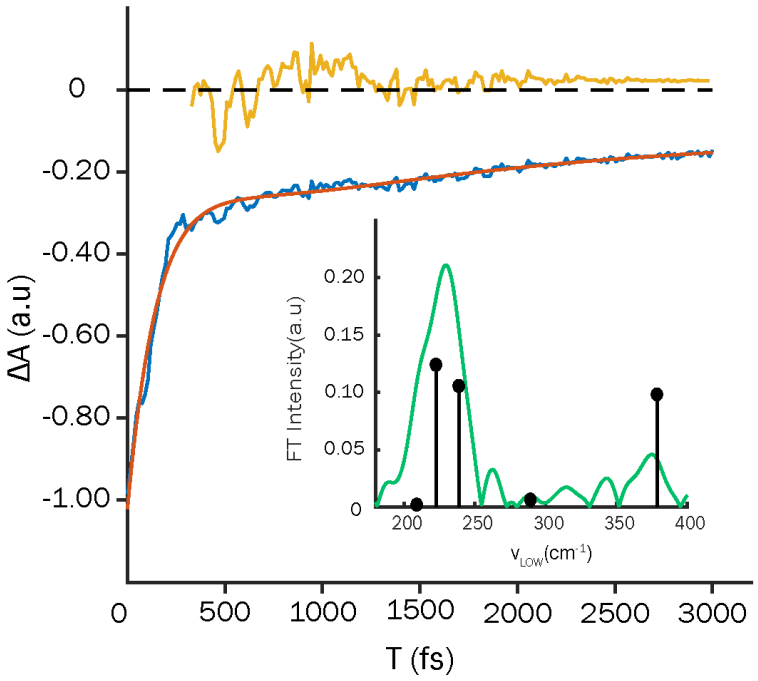

Figure 4.3: Pump-probe time traces and coupled low frequency modes of DBQ. The pump-probe time traces at 2075 cm^{-1} as indicated by the blue trace**.** This trace was chosen as it represents the fundamental region of the stationary spectrum of DBQ. The blue-solid line and red-solid line for the 2075 cm^{-1} frequency trace are the original data and bi-exponential fit, respectively. The residual trace from 220 fs for the bleach is shown as the yellow trace. The inset contains the intensity spectra of the trace along 2771 cm^{-1} calculated from the Fourier transform of the residual shown in yellow. The solid black sticks indicate harmonic frequency calculation modes (See Table 1).

The DFT calculations show a possible corresponding modulation at 239 cm^{-1} for DBQ. The calculations indicate a 'cogwheel' like symmetric in-plane bend providing the bond between the phenol and amine as the backbone for a breathing motion. This motion is an in-plane bending motion of the two ring systems towards each other i.e., it moves the deuterium atom closer to the accepting nitrogen atom thereby strongly modulating the hydrogen bond length O–D···N. The anharmonic calculations also provided cubic off-diagonal coupling terms of low frequency structural modes to the high frequency ν_{OD} mode. Table 4.1 highlights the low frequency modes that are coupled to the ν_{OD} mode and contribute to the Fourier transform spectrum. The anharmonic frequency calculation for the structure yielded a ν_{OD} fundamental frequency of 2097 cm^{-1}. Additionally, using the appropriate scaling factor of 0.968 further

reduces the calculated fundamental frequency to 2030 cm^{-1} which very matches the fundamental frequency of the IR at 2072 cm^{-1} [23].

Table 4.1: Description of the frequency calculation of DBQ with the anharmonic correction with the Intensity and Cubic coupling constants. (oop = out of plane ; ip= in plane)

Mode Type	ω_j (cm^{-1})	Intensity	Cubic Coupling Constants
Butterfly', Symmetric oop bend	91.17	1.6505	-18.1802
β(PhOH)/t(-Py) Structural torsion	117.92	0.1316	-13.4075
β(PhOH)/β(-Ph) Symmetric oop bend	209.3	0.0425	5.06494
β(-Py) Symmetric oop bend	222.9	3.7072	21.21912
Cogwheel', Symmetric ip bend	239.03	3.1417	63.24617
β(PhOH)/b(-Py) Asymmetric oop bend	289.62	0.175	-7.38333
H-bond shearing, Asymmetric ip bend	378.99	2.9292	19.68173
OD Stretch	2097.47	17.3285	--

The most intense coupled low frequency mode is at 239 cm^{-1} and this matches with the experimental results as seem in Figure 4.3 inset. The mode at 222 cm^{-1} matches closely with the shoulder seen in the Fourier transform spectrum however the resolution is not enough to identify the separate peaks. While there is some overlap between the non-resonant solvent response and the resonant low frequency modes of DBQ, the main peak at 230 cm^{-1} can be attributed to the in plane bending that modulates the donor and acceptor distance. Hence the correlation of the ν_{OD} stretch with the low frequency mode in the DBQ complex strongly suggests anharmonic coupling through low frequency structural modes gives rise to these broad lineshapes. Our observations coincide with the vibrational analysis of the data collected by Chou and co-workers where they point to a vibrational mode between 230 and 250 cm^{-1} as having a significant impact on the ESIPT for HBQ [24-31]. These results also match with previous ground state results seen in chapter 3 for HBQ.

However there are some experimental limitations to this experiment. The deuteron/hydrogen transfer process was not 100% successful as seen in the absorption spectrum in Figure 3.1. The ν_{OH} stretch centered at 2771 cm^{-1} with the characteristic substructure seen in HBQ absorption spectrum in chapter 3 (Figure 3.1) is still present in the DBQ absorption spectrum (Figure 4.1). While the NMR of the DBQ (Appendix) is seen to not have the OH proton peak, the FTIR still indicates that the dueteration was not successful. This is attributed to not using completely anaerobic conditions for the process of deuteron transfer in the glove bag rather than the traditional glovebox. The preliminary results show promise and future actions should be taken to ensure that the exchange is done under a complete sealed glove box.

Conclusion:

In conclusion, we observed coherent low-frequency motions of a hydrogen bond in the v=0 state of the O–D stretching mode in real-time. Wave packets consisting of quanta of an 230 cm^{-1} mode which strongly modulates the length of the hydrogen bond, were generated within the bandwidth of the femtosecond infrared pump pulses. Our results clearly demonstrate the anharmonic coupling of the low-frequency mode and the high-frequency O–D stretching vibration. These results coincide with previous excited state studies done on HBQ as well as ground state vibrational studies on HBQ as detailed in chapter 3 [23-30].

References:

1. J. Stenger, D. Madsen, J. Dreyer, E. T. J. Nibbering, P. Hamm, and T. Elsaesser, "Coherent Response of Hydrogen Bonds in Liquids Probed by Ultrafast Vibrational Spectroscopy," The Journal of Physical Chemistry A **105**, 2929-2932 (2001).
2. S. Yamaguchi, M. Banno, K. Ohta, K. Tominaga, and T. Hayashi, "Vibrational dynamics of benzoic acid in nonpolar solvents studied by subpicosecond infrared pump–probe spectroscopy," Chemical Physics Letters **462**, 238-242 (2008).
3. T. Elsaesser, N. Huse, J. Dreyer, J. R. Dwyer, K. Heyne, and E. T. J. Nibbering, "Ultrafast vibrational dynamics and anharmonic couplings of hydrogen-bonded dimers in solution," Chemical Physics **341**, 175-188 (2007).
4. K. Heyne, N. Huse, J. Dreyer, E. T. Nibbering, T. Elsaesser, and S. Mukamel, "Coherent low-frequency motions of hydrogen bonded acetic acid dimers in the liquid phase," J Chem Phys **121**, 902-913 (2004).
5. K. Heyne, M. Petković, E. T. J. Nibbering, O. Kühn, and T. Elsaesser, "Cascaded energy redistribution upon O-H stretching excitation in an intramolecular hydrogen bond," **79**, 389-391 (2005).
6. D. Madsen, J. Stenger, J. Dreyer, E. T. J. Nibbering, P. Hamm, and T. Elsaesser, "Coherent vibrational ground-state dynamics of an intramolecular hydrogen bond," Chemical Physics Letters **341**, 56-62 (2001).
7. M. Cheng, A. Reynolds, H. Widgren, and M. Khalil, "Generation of tunable octave-spanning mid-infrared pulses by filamentation in gas media," Opt. Lett. **37**, 1787-1789 (2012).
8. M. Balasubramanian, T. L. Courtney, J. D. Gaynor, and M. Khalil, "Compression of tunable broadband mid-IR pulses with a deformable mirror pulse shaper," Journal of the Optical Society of America B **33**, 2033-2037 (2016).
9. S. Linden, H. Giessen, and J. Kuhl, "XFROG - A new method for amplitude and phase characterization of weak ultrashort pulses," Phys. Status Solidi B **206**, 119-124 (1998).
10. M. J. Frisch, G. W. Trucks, H. B. Schlegel, G. E. Scuseria, M. A. Robb, J. R. Cheeseman, G. Scalmani, V. Barone, G. A. Petersson, H. Nakatsuji, X. Li, M. Caricato, A. V. Marenich, J. Bloino, B. G. Janesko, R. Gomperts, B. Mennucci, H. P. Hratchian, J. V. Ortiz, A. F. Izmaylov, J. L. Sonnenberg, Williams, F. Ding, F. Lipparini, F. Egidi, J. Goings, B. Peng, A. Petrone, T. Henderson, D. Ranasinghe, V. G. Zakrzewski, J. Gao, N. Rega, G. Zheng, W. Liang, M. Hada, M. Ehara, K. Toyota, R. Fukuda, J. Hasegawa, M. Ishida, T. Nakajima, Y. Honda, O. Kitao, H. Nakai, T. Vreven, K. Throssell, J. A. Montgomery Jr., J. E. Peralta, F. Ogliaro, M. J. Bearpark, J. J. Heyd, E. N. Brothers, K. N. Kudin, V. N. Staroverov, T. A. Keith, R. Kobayashi, J. Normand, K. Raghavachari, A. P. Rendell, J. C. Burant, S. S. Iyengar, J. Tomasi, M. Cossi, J. M. Millam, M. Klene, C. Adamo, R. Cammi, J. W. Ochterski, R. L. Martin, K. Morokuma, O. Farkas, J. B. Foresman, and D. J. Fox, Gaussian 16, Wallingford, CT, 2016.
11. V. Barone, "Vibrational zero-point energies and thermodynamic functions beyond the harmonic approximation," J Chem Phys **120**, 3059-3065 (2004).
12. M. Rospenk and T. Zeegers-Huyskens, "FT-IR (7500−1800 cm-1) Study of Hydrogen-Bond Complexes between Phenols−OH(OD) and Pyridine. Evidence of Proton Transfer in the Second Vibrational Excited State," The Journal of Physical Chemistry A **101**, 8428-8434 (1997).
13. M. Asselin and C. Sandorfy, "A low temperature infrared study of the band-width and frequency in self-associated alcohols," Chem. Phys. Lett. **8**, 601 (1971).
14. M. Asselin and C. Sandorfy, "Double Excitation in the Infrared Spectra of Self-Associated Alcohols," The Journal of Chemical Physics **52**, 6130-6134 (1970).
15. M. Rini, A. Kummrow, J. Dreyer, E. T. J. Nibbering, and T. Elsaesser, "Femtosecond mid-infrared spectroscopy of condensed phase hydrogen-bonded systems as a probe of structural dynamics," Faraday Discuss. **122**, 27-40 (2002).

16. R. A. Nicodemus, S. A. Corcelli, J. L. Skinner, and A. Tokmakoff, "Collective Hydrogen Bond Reorganization in Water Studied with Temperature-Dependent Ultrafast Infrared Spectroscopy," The Journal of Physical Chemistry B **115**, 5604-5616 (2011).
17. A. J. Lock, J. J. Gilijamse, S. Woutersen, and H. J. Bakker, "Vibrational relaxation and coupling of two OH-stretch oscillators with an intramolecular hydrogen bond," J Chem Phys **120**, 2351-2358 (2004).
18. C. J. Fecko, J. D. Eaves, J. J. Loparo, A. Tokmakoff, and P. L. Geissler, "Ultrafast hydrogen-bond dynamics in the infrared spectroscopy of water," Science **301**, 1698-1702 (2003).
19. J. J. Loparo, C. J. Fecko, J. D. Eaves, S. T. Roberts, and A. Tokmakoff, "Reorientational and configurational fluctuations in water observed on molecular length scales," Physical Review B **70**, 180201 (2004).
20. C. J. Fecko, J. J. Loparo, S. T. Roberts, and A. Tokmakoff, "Local hydrogen bonding dynamics and collective reorganization in water: ultrafast infrared spectroscopy of HOD/D(2)O," J Chem Phys **122**, 54506 (2005).
21. P. B. Petersen, S. T. Roberts, K. Ramasesha, D. G. Nocera, and A. Tokmakoff, "Ultrafast N−H Vibrational Dynamics of Cyclic Doubly Hydrogen-Bonded Homo- and Heterodimers," The Journal of Physical Chemistry B **112**, 13167-13171 (2008).
22. P. Moore, A. Tokmakoff, T. Keyes, and M. D. Fayer, "The low frequency density of states and vibrational population dynamics of polyatomic molecules in liquids," The Journal of Chemical Physics **103**, 3325-3334 (1995).
23. I. M. Alecu, J. Zheng, Y. Zhao, and D. G. Truhlar, "Computational Thermochemistry: Scale Factor Databases and Scale Factors for Vibrational Frequencies Obtained from Electronic Model Chemistries," Journal of Chemical Theory and Computation **6**, 2872-2887 (2010).
24. P.-T. Chou, G.-R. Wu, Y.-I. Liu, W.-S. Yu, and C.-S. Chiou, "Proton-Transfer Tautomerism in 10-Hydroxybenzo[h]quinolines: Heavy Atom Effects and Non-Hydrogen-Bonded Photorotamer Formation in 77 K Glassy Matrixes," J. Phys. Chem. A **106**, 5967-5973 (2002).
25. J. Lee and T. Joo, "Photophysical model of 10-hydroxybenzo[h]quinoline: internal conversion and excited state intramolecular proton transfer," Bull. Korean Chem. Soc. **35**, 881-885 (2014).
26. C. Schriever, K. Stock, A. J. A. Aquino, D. Tunega, S. Lochbrunner, E. Riedle, R. de Vivie-Riedle, and H. Lischka, "The interplay of skeletal deformations and ultrafast excited-state intramolecular proton transfer: Experimental and theoretical investigation of 10-hydroxybenzo[h]quinoline," Chem. Phys. **347**, 446-461 (2008).
27. P.-T. Chou, Y.-C. Chen, W.-S. Yu, Y.-H. Chou, C.-Y. Wei, and Y.-M. Cheng, "Excited-State Intramolecular Proton Transfer in 10-Hydroxybenzo[h]quinoline," J. Phys. Chem. A **105**, 1731-1740 (2001).
28. D. LeGourrierec, V. Kharlanov, R. G. Brown, and W. Rettig, "Excited-state intramolecular proton transfer (ESIPT) in 2-(2'-hydroxyphenyl)pyridine and some carbon-bridged derivatives," J. Photochem. Photobiol., A **117**, 209-216 (1998).
29. S. Takeuchi and T. Tahara, "Coherent Nuclear Wavepacket Motions in Ultrafast Excited-State Intramolecular Proton Transfer: Sub-30-fs Resolved Pump-Probe Absorption Spectroscopy of 10-Hydroxybenzo[h]quinoline in Solution," J. Phys. Chem. A **109**, 10199-10207 (2005).
30. C. H. Kim and T. Joo, "Coherent excited state intramolecular proton transfer probed by time-resolved fluorescence," Phys. Chem. Chem. Phys. **11**, 10266-10269 (2009).
31. S. Hristova, G. Dobrikov, F. S. Kamounah, S. Kawauchi, P. E. Hansen, V. Deneva, D. Nedeltcheva, and L. Antonov, "10-Hydroxybenzo[h]quinoline: switching between single- and double-well proton transfer through structural modifications," RSC Advances **5**, 102495-102507 (2015).

BIBLIOGRAPHY

1. J. M. Berg, J. L. Tymoczko, and L. Stryer, *Biochemistry* (W. H. Freeman, 2010).
2. C. Tommos and G. T. Babcock, "Proton and hydrogen currents in photosynthetic water oxidation," Biochimica et Biophysica Acta (BBA) - Bioenergetics 1458, 199-219 (2000).
3. D. Voet and J. G. Voet, *Biochemistry, 4th Edition* (John Wiley & Sons, 2010).
4. G. A. Jeffrey and W. Saenger, "The Importance of Hydrogen Bonds," in *Hydrogen Bonding in Biological Structures*, G. A. Jeffrey and W. Saenger, eds. (Springer Berlin Heidelberg, Berlin, Heidelberg, 1991), pp. 3-14.
5. N. Rawat and P. Biswas, "Hydrogen bond dynamics in intrinsically disordered proteins," The journal of physical chemistry. B 118, 3018-3025 (2014).
6. J. Fossey, D. Lefort, and J. Sorba, Free Radicals in Organic Chemistry (1993).
7. J. R. Cheeseman, M. T. Carroll, and R. F. W. Bader, "The mechanics of hydrogen bond formation in conjugated systems," Chemical Physics Letters 143, 450-458 (1988).
8. S. Wang, Z. Wang, and C. Hao, "Role of intramolecular hydrogen bonding in the excited-state intramolecular double proton transfer (ESIDPT) of calix[4]arene: A TDDFT study," Open Physics 14(2016).
9. J.-J. Zheng, Y.-Q. Lu, P.-L. Li, and C. Tao, "All-optical switching effect of the excited state proton transfer molecule 2-(2'-hydroxyphenyl) benzothiazole in different polar solvents," Wuli Xuebao 59, 6626-6631 (2010).
10. J. Ma, J. Zhao, P. Yang, D. Huang, C. Zhang, and Q. Li, "New excited state intramolecular proton transfer (ESIPT) dyes based on naphthalimide and observation of long-lived triplet excited states," Chem Commun (Camb) 48, 9720-9722 (2012).
11. E. T. J. Nibbering and T. Elsaesser, "Ultrafast Vibrational Dynamics of Hydrogen Bonds in the Condensed Phase," Chemical Reviews 104, 1887-1914 (2004).
12. T. F. Markle and J. M. Mayer, "Concerted Proton–Electron Transfer in Pyridylphenols: The Importance of the Hydrogen Bond," Angewandte Chemie International Edition 47, 738-740 (2008).
13. T. F. Markle, I. J. Rhile, A. G. DiPasquale, and J. M. Mayer, "Probing concerted proton–electron transfer in phenol–imidazoles," Proceedings of the National Academy of Sciences (2008).
14. J. M. Mayer, "PROTON-COUPLED ELECTRON TRANSFER: A Reaction Chemist's View," Annual Review of Physical Chemistry 55, 363-390 (2004).
15. J. M. Mayer, "Simple Marcus-Theory-Type Model for Hydrogen-Atom Transfer/Proton-Coupled Electron Transfer," The Journal of Physical Chemistry Letters 2, 1481-1489 (2011).
16. I. J. Rhile, T. F. Markle, H. Nagao, A. G. DiPasquale, O. P. Lam, M. A. Lockwood, K. Rotter, and J. M. Mayer, "Concerted Proton−Electron Transfer in the Oxidation of Hydrogen-Bonded Phenols," Journal of the American Chemical Society 128, 6075-6088 (2006).
17. M. Wikstrom, "Identification of the electron transfers in cytochrome oxidase that are coupled to proton-pumping," Nature 338, 776-778 (1989).
18. T. Kolev, "Influence of intermolecular hydrogen bonding on IR-spectroscopic properties of (R)-(−)-1-phenylglycinium hydrogen squarate monohydrate in solid-state. IR-LD, Raman spectroscopy and theoretical study," Journal of Molecular Structure 846, 139-146 (2007).
19. B. Kuhn, P. Mohr, and M. Stahl, "Intramolecular hydrogen bonding in medicinal chemistry," Journal of medicinal chemistry 53, 2601-2611 (2010).
20. J. C. Wright, "Multiresonant Coherent Multidimensional Spectroscopy," Annual Review of Physical Chemistry 62, 209-230 (2011).
21. P. B. Petersen, S. T. Roberts, K. Ramasesha, D. G. Nocera, and A. Tokmakoff, "Ultrafast N−H Vibrational Dynamics of Cyclic Doubly Hydrogen-Bonded Homo- and Heterodimers," The Journal of Physical Chemistry B 112, 13167-13171 (2008).

22. M. Rini, A. Kummrow, J. Dreyer, E. T. J. Nibbering, and T. Elsaesser, "Femtosecond mid-infrared spectroscopy of condensed phase hydrogen-bonded systems as a probe of structural dynamics," Faraday Discuss. 122, 27-40 (2002).
23. G. M. Sando, Q. Zhong, and J. C. Owrutsky, "Vibrational and rotational dynamics of cyanoferrates in solution," The Journal of Chemical Physics 121, 2158-2168 (2004).
24. M. Asselin and C. Sandorfy, "A low temperature infrared study of the band-width and frequency in self-associated alcohols," Chem. Phys. Lett. 8, 601 (1971).
25. M. Asselin and C. Sandorfy, "Double Excitation in the Infrared Spectra of Self-Associated Alcohols," The Journal of Chemical Physics 52, 6130-6134 (1970).
26. J. Joseph and E. D. Jemmis, "Red-, blue-, or no-shift in hydrogen bonds: a unified explanation," J Am Chem Soc 129, 4620-4632 (2007).
27. R. Costard, C. Greve, H. Fidder, and E. T. Nibbering, "Hydrogen bonding induced enhancement of Fermi resonances: ultrafast vibrational energy flow dynamics in aniline-d(5)," The journal of physical chemistry. B 119, 2711-2725 (2015).
28. N. Sheppard, "Infrared Spectroscopy and Hydrogen Bonding — Band-Widths and Frequency Shifts," 85-105 (1959).
29. H. L. Clever, "Hydrogen bond: Recent developments in theory and experimental. volume I: theory, volume II: structure and spectroscopy, volume III: dynamics, thermodynamics and special systems (Schuster P.)," Journal of Chemical Education 55, A244 (1978).
30. A. Tokmakoff and M. D. Fayer, "Infrared Photon Echo Experiments: Exploring Vibrational Dynamics in Liquids and Glasses," Acc Chem Res 28, 437-445 (2002).
31. N. Huse, K. Heyne, J. Dreyer, E. T. J. Nibbering, and T. Elsaesser, "Vibrational Multilevel Quantum Coherence due to Anharmonic Couplings in Intermolecular Hydrogen Bonds," Physical Review Letters 91, 197401 (2003).
32. T. Elsaesser, N. Huse, J. Dreyer, J. R. Dwyer, K. Heyne, and E. T. J. Nibbering, "Ultrafast vibrational dynamics and anharmonic couplings of hydrogen-bonded dimers in solution," Chemical Physics 341, 175-188 (2007).
33. K. Heyne, N. Huse, J. Dreyer, E. T. J. Nibbering, T. Elsaesser, and S. Mukamel, "Coherent low-frequency motions of hydrogen bonded acetic acid dimers in the liquid phase," The Journal of Chemical Physics 121, 902-913 (2004).
34. S. Yamaguchi, M. Banno, K. Ohta, K. Tominaga, and T. Hayashi, "Vibrational dynamics of benzoic acid in nonpolar solvents studied by subpicosecond infrared pump–probe spectroscopy," Chemical Physics Letters 462, 238-242 (2008).
35. D. Fayer, *Ultrafast Infrared And Raman Spectroscopy* (Taylor & Francis, 2001).
36. A. Tokmakoff and M. D. Fayer, "Infrared Photon Echo Experiments: Exploring Vibrational Dynamics in Liquids and Glasses," Accounts of Chemical Research 28, 437-445 (1995).
37. R. A. Kaindl, M. Wurm, K. Reimann, P. Hamm, A. M. Weiner, and M. Woerner, "Generation, shaping, and characterization of intense femtosecond pulses tunable from 3 to 20 mm," J. Opt. Soc. Am. B 17, 2086-2094 (2000).
38. C. J. Fecko, J. J. Loparo, and A. Tokmakoff, "Generation of 45 femtosecond pulses at 3 mm with a $KNbO_3$ optical parametric amplifier," Opt. Commun. 241, 521-528 (2004).
39. J. Biegert, P. K. Bates, and O. Chalus, "New Mid-Infrared Light Sources," IEEE Journal of Selected Topics in Quantum Electronics 18, 531-540 (2012).
40. M. Baudisch, H. Pires, H. Ishizuki, T. Taira, M. Hemmer, and J. Biegert, "Sub-4-optical-cycle, 340 MW peak power, high stability mid-IR source at 160 kHz," Journal of Optics 17, 094002 (2015).
41. A. M. Stingel, H. Vanselous, and P. B. Petersen, "Covering the vibrational spectrum with microjoule mid-infrared supercontinuum pulses in nonlinear optical applications," Journal of the Optical Society of America B 34, 1163 (2017).
42. T. Fuji and T. Suzuki, "Generation of sub-two-cycle mid-infrared pulses by four-wave mixing through filamentation in air," Opt. Lett. 32, 3330-3332 (2007).

43. P. B. Petersen and A. Tokmakoff, "Source for ultrafast continuum infrared and terahertz radiation," Opt. Lett. 35, 1962-1964 (2010).
44. C. R. Baiz and K. J. Kubarych, "Ultrabroadband detection of a mid-IR continuum by chirped-pulse upconversion," Opt. Lett. 36, 187-189 (2011).
45. M. Cheng, A. Reynolds, H. Widgren, and M. Khalil, "Generation of tunable octave-spanning mid-infrared pulses by filamentation in gas media," Opt. Lett. 37, 1787-1789 (2012).
46. Y. Nomura, H. Shirai, K. Ishii, N. Tsurumachi, A. A. Voronin, A. M. Zheltikov, and T. Fuji, "Phase-stable sub-cycle mid-infrared conical emission from filamentation in gases," Opt. Express 20, 24741-24747 (2012).
47. Y. Nomura, Y. T. Wang, T. Kozai, H. Shirai, A. Yabushita, C. W. Luo, S. Nakanishi, and T. Fuji, "Single-shot detection of mid-infrared spectra by chirped-pulse upconversion with four-wave difference frequency generation in gases," Opt. Express 21, 18249-18254 (2013).
48. D. J. Cook and R. M. Hochstrasser, "Intense terahertz pulses by four-wave rectification in air," Opt. Lett. 25, 1210-1212 (2000).
49. X. Xie, J. M. Dai, and X. C. Zhang, "Coherent control of THz wave generation in ambient air," Phys. Rev. Lett. 96, 075005 (2006).
50. M. D. Thomson, M. Kress, T. Loffler, and H. G. Roskos, "Broadband THz emission from gas plasmas induced by femtosecond optical pulses: From fundamentals to applications," Laser Photonics Rev. 1, 349-368 (2007).
51. K. Y. Kim, A. J. Taylor, J. H. Glownia, and G. Rodriguez, "Coherent control of terahertz supercontinuum generation in ultrafast laser-gas interactions," Nat. Photon. 2, 605-609 (2008).
52. F. Theberge, M. Chateauneuf, G. Roy, P. Mathieu, and J. Dubois, "Generation of tunable and broadband far-infrared laser pulses during two-color filamentation," Phys. Rev. A 81(2010).
53. P. Whalen, J. V. Moloney, and M. Kolesik, "Self-focusing collapse distance in ultrashort pulses and measurement of nonlinear index," Opt Lett 36, 2542-2544 (2011).
54. D. E. Laban, W. C. Wallace, R. D. Glover, R. T. Sang, and D. Kielpinski, "Self-focusing in air with phase-stabilized few-cycle light pulses," Opt Lett 35, 1653-1655 (2010).
55. S. L. Chin, T. J. Wang, C. Marceau, J. Wu, J. S. Liu, O. Kosareva, N. Panov, Y. P. Chen, J. F. Daigle, S. Yuan, A. Azarm, W. W. Liu, T. Seideman, H. P. Zeng, M. Richardson, R. Li, and Z. Z. Xu, "Advances in intense femtosecond laser filamentation in air," Laser Physics 22, 1-53 (2011).
56. M. R. Rashidian Vaziri, "Describing the propagation of intense laser pulses in nonlinear Kerr media using the ducting model," Laser Physics 23, 105401 (2013).
57. I. B. Burgess, W. E. Shimmell, and K. Saravanamuttu, "Spontaneous pattern formation due to modulation instability of incoherent white light in a photopolymerizable medium," J Am Chem Soc 129, 4738-4746 (2007).
58. T. Schneider, "Self- and Cross-Phase Modulation," 143-165 (2004).
59. K. Dolgaleva, W. C. Ng, L. Qian, J. S. Aitchison, M. C. Camasta, and M. Sorel, "Broadband self-phase modulation, cross-phase modulation, and four-wave mixing in 9-mm-long AlGaAs waveguides," Opt Lett 35, 4093-4095 (2010).
60. A. Galvanauskas, M.-Y. Cheng, K.-C. Hou, and K.-H. Liao, "High Peak Power Pulse Amplification in Large-Core Yb-Doped Fiber Amplifiers," IEEE Journal of Selected Topics in Quantum Electronics 13, 559-566 (2007).
61. N. Demirdoven, M. Khalil, O. Golonzka, and A. Tokmakoff, "Dispersion compensation with optical materials for compression of intense sub-100-fs mid-infrared pulses," Opt. Lett. 27, 433-435 (2002).
62. C. Calabrese, A. M. Stingel, L. Shen, and P. B. Petersen, "Ultrafast continuum mid-infrared spectroscopy: probing the entire vibrational spectrum in a single laser shot with femtosecond time resolution," Opt. Lett. 37, 2265-2267 (2012).

63. L. De Marco, K. Ramasesha, and A. Tokmakoff, "Experimental Evidence of Fermi Resonances in Isotopically Dilute Water from Ultrafast Broadband IR Spectroscopy," J. Phys. Chem. B 117, 15319-15327 (2013).
64. A. M. Stingel, C. Calabrese, and P. B. Petersen, "Strong Intermolecular Vibrational Coupling through Cyclic Hydrogen-Bonded Structures Revealed by Ultrafast Continuum Mid-IR Spectroscopy," J. Phys. Chem. B 117, 15714-15719 (2013).
65. C. R. Baiz and K. J. Kubarych, "Ultrabroadband detection of a mid-IR continuum by chirped-pulse upconversion," Opt Lett 36, 187-189 (2011).
66. N. Demirdöven, M. Khalil, O. Golonzka, and A. Tokmakoff, "Dispersion compensation with optical materials for compression of intense sub-100-fs mid-infrared pulses," Opt. Lett. 27, 433 (2002).
67. N. Belabas, J. P. Likforman, L. Canioni, B. Bousquet, and M. Joffre, "Coherent broadband pulse shaping in the mid infrared," Opt. Lett. 26, 743-745 (2001).
68. H. S. Tan and W. S. Warren, "Mid infrared pulse shaping by optical parametric amplification and its application to optical free induction decay measurement," Opt. Express 11, 1021-1028 (2003).
69. S. H. Shim, D. B. Strasfeld, E. C. Fulmer, and M. T. Zanni, "Femtosecond pulse shaping directly in the mid-IR using acousto-optic modulation," Opt. Lett. 31, 838-840 (2006).
70. R. Maksimenka, P. Nuernberger, K. F. Lee, A. Bonvalet, J. Milkiewicz, C. Barta, M. Klima, T. Oksenhendler, P. Tournois, D. Kaplan, and M. Joffre, "Direct mid-infrared femtosecond pulse shaping with a calomel acousto-optic programmable dispersive filter," Opt. Lett. 35, 3565-3567 (2010).
71. J. M. Nite, J. D. Cyran, and A. T. Krummel, "Active Bragg angle compensation for shaping ultrafast mid-infrared pulses," Opt. Express 20, 23912-23920 (2012).
72. A. Cartella, S. Bonora, M. Forst, G. Cerullo, A. Cavalleri, and C. Manzoni, "Pulse shaping in the mid-infrared by a deformable mirror," Opt. Lett. 39, 1485-1488 (2014).
73. A. M. Weiner, "Ultrafast optical pulse shaping: A tutorial review," Opt. Commun. 284, 3669-3692 (2011).
74. A. Ghosh, A. L. Serrano, T. A. Oudenhoven, J. S. Ostrander, E. C. Eklund, A. F. Blair, and M. T. Zanni, "Experimental implementations of 2D IR spectroscopy through a horizontal pulse shaper design and a focal plane array detector," Optics Letters 41, 524-527 (2016).
75. V. Cardin, N. Thiré, S. Beaulieu, V. Wanie, F. Légaré, and B. E. Schmidt, "0.42 TW 2-cycle pulses at 1.8 μm via hollow-core fiber compression," Applied Physics Letters 107, 181101 (2015).
76. H. Liang, P. Krogen, R. Grynko, O. Novak, C.-L. Chang, G. J. Stein, D. Weerawarne, B. Shim, F. X. Kärtner, and K.-H. Hong, "Three-octave-spanning supercontinuum generation and sub-two-cycle self-compression of mid-infrared filaments in dielectrics," Opt. Lett. 40, 1069-1072 (2015).
77. E. Zeek, K. Maginnis, S. Backus, U. Russek, M. Murnane, G. Mourou, H. Kapteyn, and G. Vdovin, "Pulse compression by use of deformable mirrors," Opt. Lett. 24, 493-495 (1999).
78. A. Baltuska and T. Kobayashi, "Adaptive shaping of two-cycle visible pulses using a flexible mirror," Appl. Phys. B 75, 427-443 (2002).
79. P.-T. Chou, Y.-C. Chen, W.-S. Yu, Y.-H. Chou, C.-Y. Wei, and Y.-M. Cheng, "Excited-State Intramolecular Proton Transfer in 10-Hydroxybenzo[h]quinoline," The Journal of Physical Chemistry A 105, 1731-1740 (2001).
80. S. Takeuchi and T. Tahara, "Coherent Nuclear Wavepacket Motions in Ultrafast Excited-State Intramolecular Proton Transfer: Sub-30-fs Resolved Pump-Probe Absorption Spectroscopy of 10-Hydroxybenzo[h]quinoline in Solution," J. Phys. Chem. A 109, 10199-10207 (2005).
81. C. H. Kim and T. Joo, "Coherent excited state intramolecular proton transfer probed by time-resolved fluorescence," Phys. Chem. Chem. Phys. 11, 10266-10269 (2009).
82. J. Lee and T. Joo, "Photophysical model of 10-hydroxybenzo[h]quinoline: internal conversion and excited state intramolecular proton transfer," Bull. Korean Chem. Soc. 35, 881-885 (2014).
83. M. Higashi and S. Saito, "Direct Simulation of Excited-State Intramolecular Proton Transfer and Vibrational Coherence of 10-Hydroxybenzo[h]quinoline in Solution," J. Phys. Chem. Lett. 2, 2366-2371 (2011).

84. S. Luber, K. Adamczyk, E. T. J. Nibbering, and V. S. Batista, "Photoinduced Proton Coupled Electron Transfer in 2-(2′-Hydroxyphenyl)-Benzothiazole," The Journal of Physical Chemistry A 117, 5269-5279 (2013).
85. O. F. Mohammed, S. Luber, V. S. Batista, and E. T. J. Nibbering, "Ultrafast Branching of Reaction Pathways in 2-(2′-Hydroxyphenyl)benzothiazole in Polar Acetonitrile Solution," The Journal of Physical Chemistry A 115, 7550-7558 (2011).
86. S. Pijeau, D. Foster, and E. G. Hohenstein, "Excited-State Dynamics of 2-(2'-Hydroxyphenyl)benzothiazole: Ultrafast Proton Transfer and Internal Conversion," J. Phys. Chem. A 121, 4595-4605 (2017).
87. S. M. Aly, A. Usman, M. AlZayer, G. A. Hamdi, E. Alarousu, and O. F. Mohammed, "Solvent-Dependent Excited-State Hydrogen Transfer and Intersystem Crossing in 2-(2'-Hydroxyphenyl)-Benzothiazole," J. Phys. Chem. B 119, 2596-2603 (2015).
88. P.-T. Chou, G.-R. Wu, Y.-I. Liu, W.-S. Yu, and C.-S. Chiou, "Proton-Transfer Tautomerism in 10-Hydroxybenzo[h]quinolines: Heavy Atom Effects and Non-Hydrogen-Bonded Photorotamer Formation in 77 K Glassy Matrixes," J. Phys. Chem. A 106, 5967-5973 (2002).
89. R. De Vivie-Riedle, V. De Waele, L. Kurtz, and E. Riedle, "Ultrafast Excited-State Proton Transfer of 2-(2'-Hydroxyphenyl)benzothiazole: Theoretical Analysis of the Skeletal Deformations and the Active Vibrational Modes," J. Phys. Chem. A 107, 10591-10599 (2003).
90. C. Schriever, K. Stock, A. J. A. Aquino, D. Tunega, S. Lochbrunner, E. Riedle, R. de Vivie-Riedle, and H. Lischka, "The interplay of skeletal deformations and ultrafast excited-state intramolecular proton transfer: Experimental and theoretical investigation of 10-hydroxybenzo[h]quinoline," Chem. Phys. 347, 446-461 (2008).
91. M. Pfeiffer, K. Lenz, A. Lau, and T. Elsaesser, "Resonance Raman studies of heterocyclic aromatic compounds showing ultrafast intramolecular proton transfer," J. Raman Spectrosc. 26, 607-615 (1995).
92. J. Zhao, S. Ji, Y. Chen, H. Guo, and P. Yang, "Excited state intramolecular proton transfer (ESIPT): from principal photophysics to the development of new chromophores and applications in fluorescent molecular probes and luminescent materials," Physical chemistry chemical physics : PCCP 14, 8803-8817 (2012).
93. D. Madsen, J. Stenger, J. Dreyer, E. T. J. Nibbering, P. Hamm, and T. Elsaesser, "Coherent vibrational ground-state dynamics of an intramolecular hydrogen bond," Chemical Physics Letters 341, 56-62 (2001).
94. C. Iaconis and I. A. Walmsley, "Spectral phase interferometry for direct electric-field reconstruction of ultrashort optical pulses," Opt. Lett. 23, 792-794 (1998).
95. N. Kungwan, F. Plasser, A. J. Aquino, M. Barbatti, P. Wolschann, and H. Lischka, "The effect of hydrogen bonding on the excited-state proton transfer in 2-(2'-hydroxyphenyl)benzothiazole: a TDDFT molecular dynamics study," Physical chemistry chemical physics : PCCP 14, 9016-9025 (2012).
96. S. Linden, H. Giessen, and J. Kuhl, "XFROG - A new method for amplitude and phase characterization of weak ultrashort pulses," Phys. Status Solidi B 206, 119-124 (1998).
97. M. Balasubramanian, T. L. Courtney, J. D. Gaynor, and M. Khalil, "Compression of tunable broadband mid-IR pulses with a deformable mirror pulse shaper," J. Opt. Soc. Am. B 33, 2033-2037 (2016).
98. M. J. Frisch, G. W. Trucks, H. B. Schlegel, G. E. Scuseria, M. A. Robb, J. R. Cheeseman, G. Scalmani, V. Barone, G. A. Petersson, H. Nakatsuji, X. Li, M. Caricato, A. V. Marenich, J. Bloino, B. G. Janesko, R. Gomperts, B. Mennucci, H. P. Hratchian, J. V. Ortiz, A. F. Izmaylov, J. L. Sonnenberg, Williams, F. Ding, F. Lipparini, F. Egidi, J. Goings, B. Peng, A. Petrone, T. Henderson, D. Ranasinghe, V. G. Zakrzewski, J. Gao, N. Rega, G. Zheng, W. Liang, M. Hada, M. Ehara, K. Toyota, R. Fukuda, J. Hasegawa, M. Ishida, T. Nakajima, Y. Honda, O. Kitao, H. Nakai, T. Vreven, K. Throssell, J. A. Montgomery Jr., J. E. Peralta, F. Ogliaro, M. J. Bearpark, J. J. Heyd, E. N. Brothers, K. N. Kudin, V. N. Staroverov, T. A. Keith, R. Kobayashi, J. Normand, K. Raghavachari, A. P. Rendell, J. C. Burant, S. S.

Iyengar, J. Tomasi, M. Cossi, J. M. Millam, M. Klene, C. Adamo, R. Cammi, J. W. Ochterski, R. L. Martin, K. Morokuma, O. Farkas, J. B. Foresman, and D. J. Fox, Gaussian 16, Wallingford, CT, 2016.
99. V. Barone, "Vibrational zero-point energies and thermodynamic functions beyond the harmonic approximation," J Chem Phys 120, 3059-3065 (2004).
100. Y. Marechal and A. Witkowski, "Infrared Spectra of H-Bonded Systems," The Journal of Chemical Physics 48, 3697-3705 (1968).
101. M. Kubicki, T. Borowiak, and W. Z. Antkowiak, "10-Hydroxybenzo[h]quinoline," Acta Crystallographica Section C 51, 1173-1175 (1995).
102. M. Rospenk and T. Zeegers-Huyskens, "FT-IR (7500−1800 cm-1) Study of Hydrogen-Bond Complexes between Phenols−OH(OD) and Pyridine. Evidence of Proton Transfer in the Second Vibrational Excited State," The Journal of Physical Chemistry A 101, 8428-8434 (1997).
103. K. Ramasesha, L. De Marco, A. Mandal, and A. Tokmakoff, "Water vibrations have strongly mixed intra- and intermolecular character," Nature chemistry 5, 935-940 (2013).
104. S. T. van der Post, C. S. Hsieh, M. Okuno, Y. Nagata, H. J. Bakker, M. Bonn, and J. Hunger, "Strong frequency dependence of vibrational relaxation in bulk and surface water reveals sub-picosecond structural heterogeneity," Nature communications 6, 8384 (2015).
105. A. J. Lock and H. J. Bakker, "Temperature dependence of vibrational relaxation in liquid H2O," The Journal of Chemical Physics 117, 1708-1713 (2002).
106. H.-K. Nienhuys, S. Woutersen, R. A. van Santen, and H. J. Bakker, "Mechanism for vibrational relaxation in water investigated by femtosecond infrared spectroscopy," The Journal of Chemical Physics 111, 1494-1500 (1999).
107. R. A. Nicodemus, S. A. Corcelli, J. L. Skinner, and A. Tokmakoff, "Collective Hydrogen Bond Reorganization in Water Studied with Temperature-Dependent Ultrafast Infrared Spectroscopy," The Journal of Physical Chemistry B 115, 5604-5616 (2011).
108. C. J. Fecko, J. D. Eaves, J. J. Loparo, A. Tokmakoff, and P. L. Geissler, "Ultrafast hydrogen-bond dynamics in the infrared spectroscopy of water," Science 301, 1698-1702 (2003).
109. P. B. Petersen, S. T. Roberts, K. Ramasesha, D. G. Nocera, and A. Tokmakoff, "Ultrafast N-H vibrational dynamics of cyclic doubly hydrogen-bonded homo- and heterodimers," The journal of physical chemistry. B 112, 13167-13171 (2008).
110. M. Khalil, O. Golonzka, N. Demirdöven, C. J. Fecko, and A. Tokmakoff, "Polarization-selective femtosecond Raman spectroscopy of isotropic and anisotropic vibrational dynamics in liquids," Chemical Physics Letters 321, 231-237 (2000).
111. S. T. Roberts, K. Ramasesha, P. B. Petersen, A. Mandal, and A. Tokmakoff, "Proton transfer in concentrated aqueous hydroxide visualized using ultrafast infrared spectroscopy," The journal of physical chemistry. A 115, 3957-3972 (2011).
112. A. J. A. Aquino, F. Plasser, M. Barbatti, and H. Lischka, "Ultrafast excited-state proton transfer processes: energy surfaces and on-the-fly dynamics simulations," Croat. Chem. Acta 82, 105-114 (2009).

VITA

Madhumitha (Madhu) Balasubramanian came to United States of America from Thailand, to start undergraduate studies in Hiram College, Ohio. She graduated at 2011, *magna cum Laude* with her Bachelors of Arts with a major in chemistry. She spent a year working a lab technician at Hiram College before starting graduate school. In 2012, Madhu pursued a graduate career to achieve a Ph.D of Chemistry in 2018. While at the University of Washington, she studied under the direction of Munira Khalil investigating anharmoic coupling of the low frequency structural modes to high frequency hydroxyl/deuteroxyl vibrational modes using pump probe spectroscopy.